Turbulence and Vorticity Generated by Breaking Waves

Thomas Richard Haydon

A thesis submitted in fulfilment of the requirements

for the degree of Doctor of Philosophy

to the

University of Edinburgh

1998

Abstract

Experiments have been performed on the flow generated after the breaking of laboratory-generated water waves. Digital Particle Image Velocimetry (DPIV) was employed to make flow-field measurements in the post-breaking region of both spilling and plunging breakers, for a range of times close to breaking. The development of the technique in order to study the temporal evolution of the flow with high resolution CCD cameras is outlined. The visual record generated by PIV is presented in the form of a large set of vorticity and velocity maps. This information is used to describe the flow and its evolution over time. The raw data is then further processed in order to demonstrate the effectiveness of PIV in measuring complex turbulent characteristics. Energy and velocity profiles, temporal decay of turbulent kinetic energy and power spectra are calculated and the results compared with other experimental, numerical and theoretical work. Similarities and differences are considered and explanations offered.

Acknowledgements

I would like to thank Clive Greated for his supervision during the course of my study and Frank Morris for accommodating my untidy methods of work. Also thankyou to all my friends within and outwith the department for accompanying me on numerous visits to the pub.

Finally I thank my parents for financing my studies and supporting me throughout.

Table of Contents

List of Figures

List of Tables

Symbols Used in This Thesis

a Wave amplitude

f_c Frequency of central component of breaking wave input spectrum

k_c Wave number of central component of breaking wave input spectrum

v_p Phase velocity of breaking wave

H_0 Wave height at breaking

d Water depth measured from the still water surface

$k_c d$ Non-dimensionalised water depth

$a k_c$ Non-dimensionalised wave-height

Chapter 1

Introduction

1.1 General subject background

Breaking waves have many important and diverse applications within coastal engineering. In the near-shore region they are important in coastal erosion and the transport of sediment along and up beaches. In deep water, the forces they exert on ships and off-shore structures such as oil-platforms are important and need to be estimated when the structures are designed. Furthermore the dispersion of pollutants such as effluent and oil have been shown to be heavily dependent on wave-breaking.

The mixing process, to which wave-breaking contributes, has far-reaching environmental implications. For example Gibson *et al* [27] showed that intermittent turbulence produced by the breaking process has an adverse effect on the growth rate of plankton in the upper region of the ocean.

There have been a number of recent laboratory and numerical studies on the evolution of water waves up to the point of breaking. The forces produced prior to breaking are easier to predict than the turbulent, chaotic motion that follows. It is however, this turbulent motion that causes mixing, sediment transport, dispersion and diffusion near to the water surface. The study of the post-breaking region has been limited due to the nature of the conditions once the free-surface is broken.

This results in numerical simulations being impossible due to the combination of the chaotic, almost random nature of the flow and the complexity of the boundary conditions. Experimental investigations are also difficult because of the adverse flow conditions after breaking; the motion is turbulent, three-dimensional and decays with time.

Most techniques for the study of fluid flow are point techniques, allowing one point in the flow to be studied over time. These methods are suitable for studying homogeneous turbulent flow but since instantaneous spatial information is not yielded, spatially intermittent or inhomogeneous turbulence is not characterised fully. Other methods of flow visualisation and measurement have been limited by the technology of the systems employed.

1.2 Aim of this study

In this study Particle Image Velocimetry (PIV) is used to make measurements in the post-breaking region of laboratory water waves. This technique provides full-field spatial information on the flow at a particular instant of time. There are a number of main objectives that were tackled during the course of these experiments.

- The further development of PIV in order to study the flow-field that exists after breaking. The use of digital PIV is a very recent development that is, in the main, technology limited. The image acquisition system was developed such that high-resolution PIV images could be acquired in quick succession. The flow is complicated and unsteady, decaying significantly with time and is a mixture of turbulent and non-turbulent velocity contributions. Optimisation of experimental parameters such as image-shifting velocity, exposure of CCD array, area of study, illumination period and

position of camera is required to measure the flow-field effectively.

- To make a qualitative description of the breaking process and the early stages of the post-breaking flow, with the assistance of high-speed video footage and PIV vorticity and velocity information.

- To produce a large and comprehensive dataset of velocity information that could be used to assist with the development of numerical models of this process.

- To quantitatively describe the evolution of post-breaking turbulence. This includes the spatial and temporal decay of the turbulence and the characteristic differences that exist between spilling and plunging breakers. Comparisons with similar work using different experimental techniques, and theories are made.

  The circulation produced after breaking is also measured and compared with an order of magnitude estimate of the pre-breaking circulation.

- The results were non-dimensionalised in order that future studies in the laboratory and the ocean can make direct comparisons with the results obtained here.

1.3   Literature review

This study encompasses a large amount of work in many diverse fields. A convenient starting point for the review of research is a qualitative study and description of the process by Bonmarin [10] who described the pre and post-breaking flow in great detail. This work ties in with New [48] who, from a numerical modeling point of view, fitted ellipses to the free-surface of numerically generated breaking

waves in an attempt to parameterise its evolution. This was an approach also used by Longeut-Higgins [40].

The flow velocities have traditionally been measured using Laser Doppler Anemometry (LDA) which, although highly accurate, is limited because it only gives temporal information on the flow at a fixed point.

LDA measurements on laboratory breaking waves have been made by many researchers. Stive [61] and Swan [62] have used LDA to study waves before the point of breaking. In these cases a large number of repeats are required in order to build up a spatial picture of the flow field, which requires the waves to be highly repeatable.

Rapp and Melville [56], Magnaudet and Thais [42] , Hattori and Aono [31], Dommermuth *et al* [18] and Nadaoka *et al* [46] [47] have all made measurements using LDA or LDV (an identical technique) after breaking. The major problem that was identified with such measurements was, that after breaking, the flow is a combination of non-turbulent and turbulent motion. The most straightforward approach to this problem is to perform many repeats of the experiment and measure the ensemble mean motion which can be subtracted from the measured flow velocity, to yield the fluctuating component of velocity. This was the technique that Rapp and Melville [56] used. The assumption that all non-turbulent motion is repeatable is fundamental to this approach, something that is not necessarily true. Also, for this to be done over a large area with a high degree of accuracy it requires a huge total number of repeats.

Similar problems can be identified in field studies, where LDA has been used to study the upper layer of deep water in oceans or lakes [20], [41], [37]. Other researchers have studied the turbulence in the near-shore surf zone [26]. Gargett [25] gives a comprehensive review of the work done on ocean turbulence, covering

mainly the ocean surface boundary layer. Many of the works cited in that paper concern themselves with this boundary layer and refer to an enhanced level of turbulence in this region. In the case of field studies repeat runs of the experiment cannot be used to measure the mean motion so a more satisfactory method needed to be developed.

Many researchers have made efforts to separate the mean motion from the turbulent motion in post-breaking flows both in laboratory and field experiments. Benilov and Filushkin [9] introduce a linear filtration method of separation, while Kitaigorodskii *et al* [35] applied a more complex, statistical method to field data collected by Donelan [19]. Thais and Magnaudet [42] developed a triple decomposition technique that firstly involved calculating the instantaneous stream function from a knowledge of the motion of the surface and then a linear spectral filtration of the remaining flow structures. There is no single perfect method of separation and the various techniques have their relative advantages and disadvantages. The problem of ensuring only non-turbulent motion is removed will continue to cause problems for research in this field.

There have only been a few wave breaking studies using PIV. Skyner [60] made an extensive study using PIV on the pre-breaking dynamics of plunging breakers using wet-film photography. Perlin *et al* [50] performed a similar study concentrating mainly on the motion around the point of overturning.

The advent of digital PIV and techniques for resolving directional ambiguity have created the opportunity for studying turbulent flows. Damm [16] and Westerweel [69] demonstrated that PIV could be effectively used in the study of turbulence. An early study of post-breaking turbulence was made by Quinn *et al* [53] using an image-shifting technique. However, the use of wet film meant that the study was restricted by the time consuming process of film development.

Work done as part of this study [32] shows the initial attempts to extend the post-breaking measurements using digital technology.

Dabiri and Gharib [15] and Lin and Rockwell [38] [39] studied post-breaking structures in steady or quasi-steady breakers. This overcame any concern regarding decaying flow as their regimes were stationary, however, it must be recognised that there is a significant difference between this case and an unsteady breaker.

Numerical simulations of waves up to the point of breaking have been developed successfully. Forehand [23] and Chopra [13] have both simulated the flow using various techniques with reasonable accuracy. The work of Skyner and that of Dommermuth *et al* made direct comparisons between numerical simulations and experiments.

After breaking simulations are in early stages of development. Barnes [7] has attempted to model the action of the vorticity in the post-breaking flow using a number of point vortices and data collected in this study.

One aspect of the post-breaking turbulence that has often been studied is the wave-number spectra. Many researchers have found close agreement with the Kolmogorov -5/3 law [8], [26], [33], but often suggesting slightly different values for the spectral slope, hinting that it is heavily dependent on how strongly two-dimensional the flow is. Both Battjes [8] and Lemin *et al* [37] found evidence of a change in the slope of the spectra that coincided with a transition from two-dimensional to three-dimensional motion.

Chapter 2

Experimental Techniques and Facilities

2.1 Summary

Particle Image Velocimetry (PIV) is an accurate method of measuring the flow velocities in a two-dimensional plane in both gas and liquid flows.

In this study all velocity information was acquired using a digital PIV system, in which, a rotating mirror image-shifting system was employed to fully resolve the complex flow characteristics. The development and adaption of the system in order to enable the study of breaking wave turbulence is described in this chapter. The remaining limitations relating to the implications that the use of image shifting and DPIV have on the accuracy of the technique are discussed. The sources of possible error are introduced and their importance assessed.

All experiments were performed in the same wave flume, using two different types of breaker: an extreme plunging breaker and a gentle spilling breaker. In addition, surface profiles and the motion of the wave paddle were measured for each experiment.

2.2 PIV

The PIV system used was based on the well documented facility at Edinburgh University, initially developed by Gray and Skyner [28, 60]. An in-depth discussion of PIV is given by Adrian [1] [3] and is not entered into here. However as PIV is undergoing continuous development, a brief description will be given, with particular attention given to the recently developed aspects specific to this study, and the areas where the author has made a contribution.

2.2.1 PIV method

PIV is a two staged process consisting of the acquisition of an image of the flow and the analysis of the image to yield full-field velocity information.

Stage 1

The flow should be seeded with small, neutrally buoyant particles which follow the flow accurately and scatter light effectively when illuminated. The illumination is provided by a continuous wave argon-ion laser (wavelength approximately 514nm), which is directed into a scanning beam illumination system. The construction of this system is described by Gray [29] and is shown in figure 2.1. The laser beam is directed onto a highly reflective mirror and then upwards through collimating lens' towards a rapidly rotating octagonal mirror. As this mirror rotates, the beam is reflected along the length of the parabolic mirror and upwards into the flow region of interest. Therefore, the pseudo-light sheet is in fact a single beam periodically scanning through the flow.

The seeding used is conifer pollen, which is nearly neutrally buoyant when saturated [54] and has been found to follow the flow accurately by Gray [28] and to resolve structures much smaller than those considered here by Bruce [12].

The traditional technique for acquiring images of the flow was on photographic
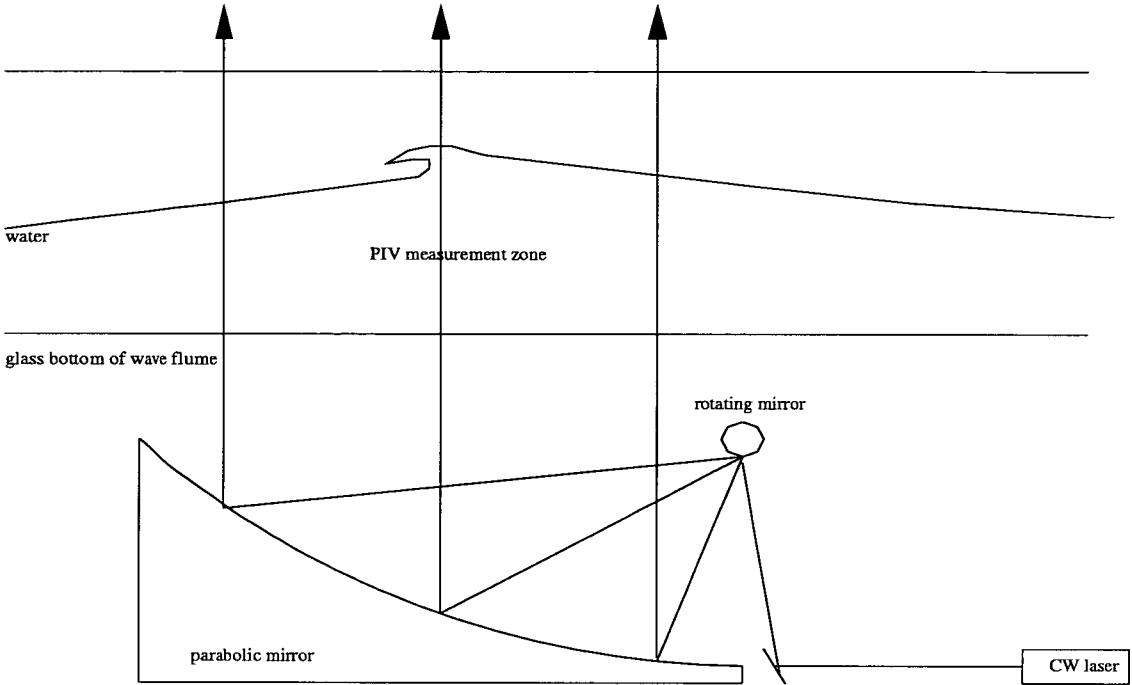
Figure 2.1: The scanning beam system.

film [52, 45, 21]. The technique has been vastly improved and expedited with the introduction of digital PIV, involving the use of CCD cameras and the fully computerised analysis of images [69]. These developments to the PIV system at Edinburgh, have primarily taken place during the course of this study, with a significant contribution made by the author. This will be covered in section 2.4. The exposure of the CCD array should be such that multiple images of single seeding particles appear on the image. There are no absolute optimum values for the number of multiple images, however, this number was generally 3-5 in these experiments. The images appear as bright spots on a dark background.

Stage 2

The analysis of these digital images yield full field velocity information. This stage is performed much faster and accurately using the digital analysis technique compared to the Young's fringes technique described by Skyner [60].

9

The analysis stage exploits the simple principle of velocity being equal to distance divided by time. The distance between successive images of a particular particle, along with the knowledge of the stroboscopic illumination period will yield velocity values. In practice this is done by taking small sub-sections of the PIV image and computationally performing an auto-correlation function on the grey-scales within the subsection.

The correlation between two functions is the degree to which they match up when moved relative to each other. Without entering into a lengthy proof (see Klien and Furtak [36]), the Fourier Transform of the cross-correlation between two functions is given as

$$G(f_1 \otimes f_2) = F_1(u)F_2^\star(u) \tag{2.1}$$

where u is a spatial frequency and the $\star$ denotes the complex conjugate. In the special case of autocorrelation where $f_1 = f_2$ the above equation becomes

$$G(f \otimes f) = |F(u)|^2 \tag{2.2}$$

This relationship is called the *Wiener-Khintchine theorem.* Taking the inverse Fourier Transform now gives the autocorrelation function

$$\hat{\nu} = G^{-1}(|F(u)|^2) \tag{2.3}$$

So if the grey-scales within the subsection are regarded as a function of x and y, then by simply performing an FFT on this function, squaring the modulus and then inverse Fourier Transforming the result, the autocorrelation function is given. A typical autocorrelation function characteristically consists of a large central peak due to self correlation and two secondary peaks corresponding to the correlation of multiple images displaced by one image separation, displaced either side of the central peak. There are also several much smaller peaks due

to the correlation of multiple particle image separations. The velocity value at this point is obtained by removing the central peak and measuring the distance and relative orientation of the two secondary peaks, giving the magnitude and direction of the velocity.

A further discussion of these issues relating to digital PIV applied to this study will be made in section 2.4.

2.3   Image shifting

Many real flows are not uni-directional and consist of velocities in all directions. The autocorrelation method of PIV has an inherent problem in dealing with such flows. There is no way of knowing from a set of multiple particle images, which image is first and which last, and hence which direction the particle is traveling at that point. Therefore a 180° directional ambiguity exists. Additionally there are definite limitations to the particle separations that can be analysed to yield accurate velocity measurements [60]. The restricted range of particle separations on a PIV image and the dynamic range of velocities that these separations correspond to, implies that velocities above an upper threshold value and below a lower threshold value, cannot be measured by a given system.

Image shifting is a technique described by Adrian [2] that consists of imparting a constant velocity throughout the flow such that all velocities appear to lie in the same direction and the range of particle separations lie within the analysable range. This velocity can be removed after the analysis stage leaving the true velocity field. The image shifting system used in this study was developed by Iain Morrison and is described comprehensively in his thesis [45], which also has an in-depth analysis of its implementation.

The set up is shown schematically in figure 2.2. It consists of a flat mirror

light sheet

flow region

flat mirror
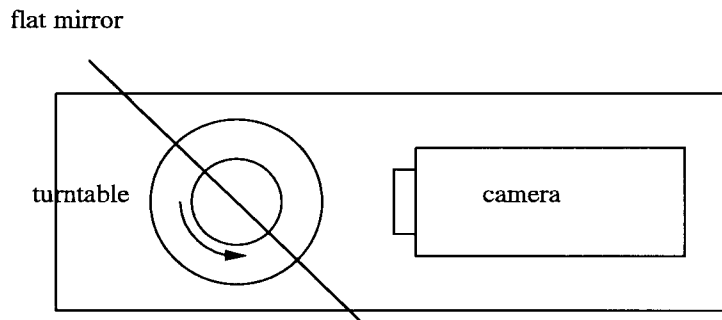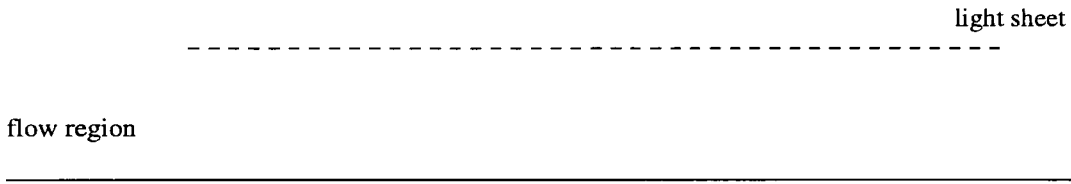
turntable

camera

Figure 2.2: A plan view of the image shifting apparatus and the wave tank.

that sits on a turntable that screws into a solid base. The camera also sits on this base which should be parallel to the measurement zone. The motion of the turntable is accurately controlled by computer so the camera is triggered when the mirror is rotating at the required angular velocity and is at 45° to the plane of the measurement zone.

2.3.1 Image shifting errors

Image shifting introduces a number of errors into PIV [45]. The construction of the system is such that random errors due to variations of the angular velocity of the turntable and camera vibration are minimised. Of more interest and importance are the systematic errors introduced.

Distortion of images
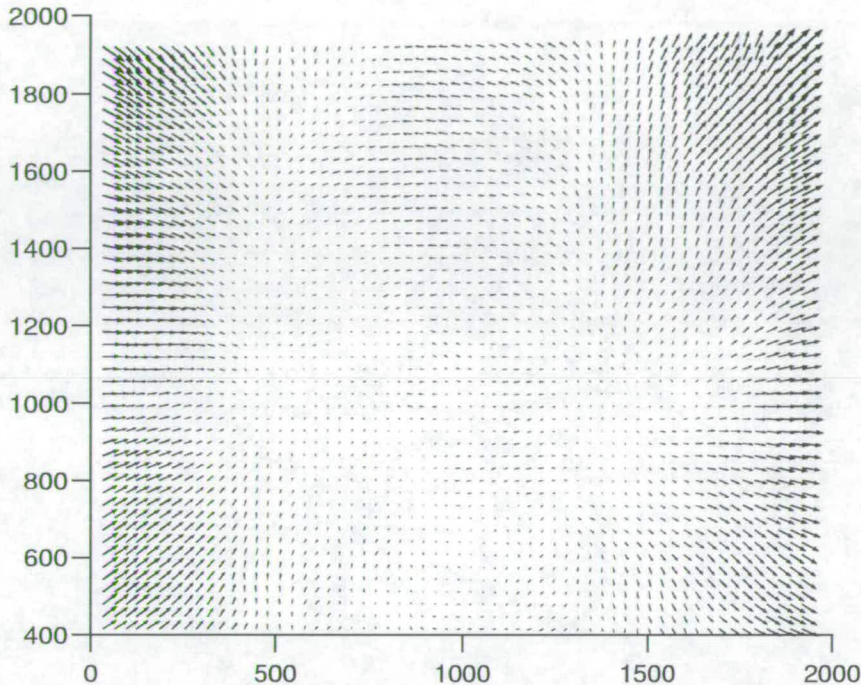
Figure 2.3: Image shifting velocity distortion.

The shift velocity is not uniform throughout the image due to differing path lengths from the CCD array to various parts of the mirror and to the flow. The question arises as to how this effect should be corrected for. Morrison [45] explicitly calculated the form of the distortion throughout the image for the particular experimental parameters he used, proposing that this should be subtracted from the velocity maps. Earnshaw [21] ensemble averaged still-water shift-velocity calibration maps, and used this as the form of the distortion to remove.

The former was ruled out as being too complicated and time consuming compared with the relatively little gained in accuracy. Care must, however, be taken when using the ensemble technique, not to introduce significant small scale noise
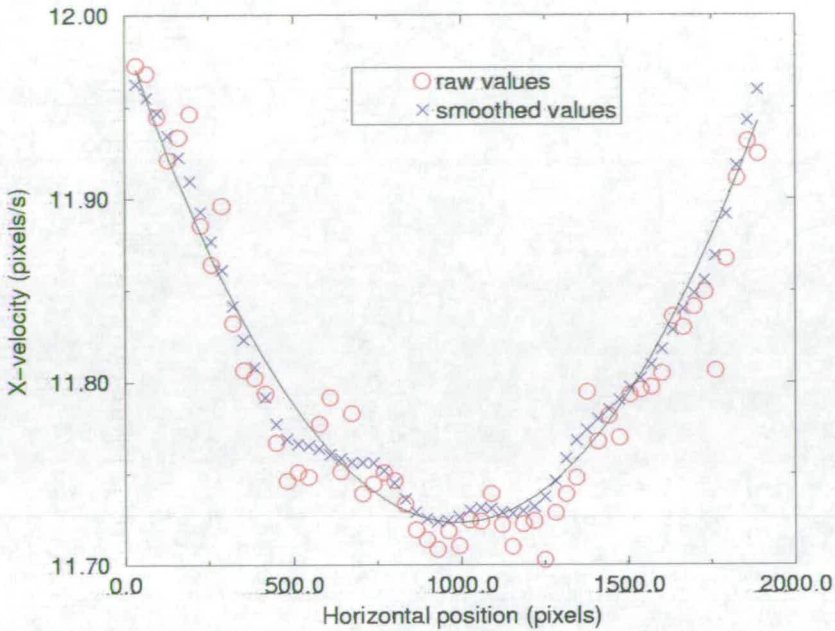
Figure 2.4: Horizontal shift velocity component showing the best-fit quadratic to the smoothed velocities.

into the experimental procedure. If a number of repeated calibration pictures are simply averaged the result is generally noisy. Careful editing and a certain amount of smoothing of the velocity information produces a resultant vector map that closely resembles the characteristic distortion field shown by Morrison [45]. This is shown for an ensemble of ten calibration velocity fields in figure 2.3 (the central velocity is subtracted so that the true form of the distortion can be displayed). The vertically averaged variation of x-velocity with x is shown in figure 2.4. The variation across the measurement zone is of the order of 2% with the most dramatic effects apparent at the edges.

The effect must be accounted for in this study because it is desirable to investigate the largest possible flow region. This is because the features of interest in the flow are "patches" of vorticity that both decay and translate.
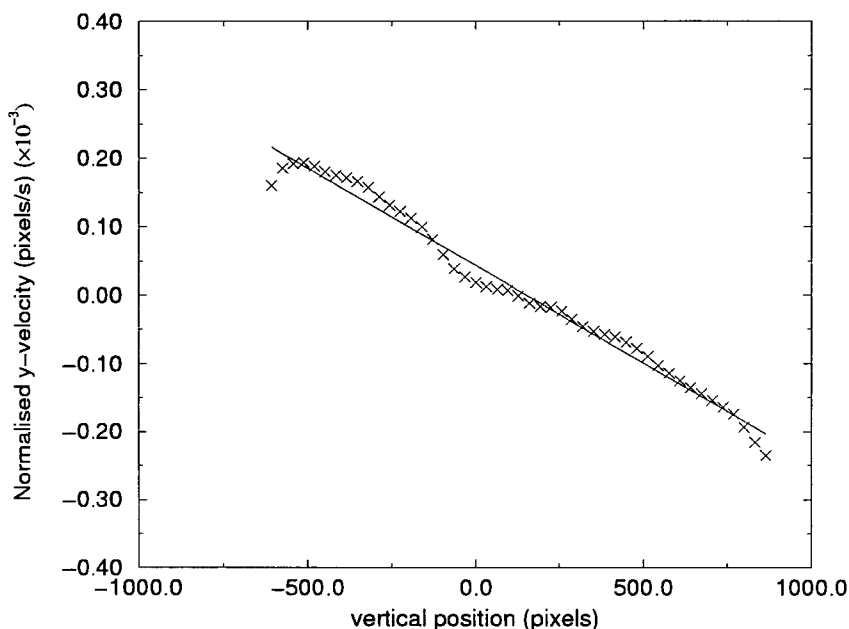
Figure 2.5: Normalised vertical shift velocities.

It was decided that the x-velocities would be corrected by using a quadratic fit to the smoothed data, as shown in figure 2.4. The y-velocities are a different case in that they are dependent on both the horizontal and vertical position within the flow. However, for a constant x-position the relationship between the y-velocity and the y-position is linear. The y-velocities were therefore normalised by the x-value at each point (measured from the centre of the image), averaged horizontally and then a straight line fitted to the data (see figure 2.5). This best-fit was then used to calculate the vertical velocity.

Other systematic errors produce distortive effects that may also cause problems. The reflecting mirror used in this system was sufficiently high quality that there would be no discernible errors due to its flatness.

Variation in the angle of the mirror from 45° when the image is acquired,

translates the flow region and produces a velocity gradient across the image. If this was significant it would be noticeable from observing the horizontal velocity profile as shown in figure 2.4. There appears to be no such difference in velocity values at the extremities in this or other similar profiles.

Using image shifting also has a very important effect on the spatial resolution of PIV. This is dealt with in the next section.

2.4 Digital PIV

2.4.1 Introduction

Digital PIV (hereafter DPIV) is a relatively new development of PIV. In its initial stages of development [69, 71] the low pixel array sizes meant that there was a choice between investigating a larger flow field and losing resolution of smaller scales of motion or, resolving the small scales but reducing the area of study. The introduction of increased pixel array sizes exposed the limitations of computers and frame-grabbing hardware regarding the processing of large image files. However, with the increased availability of affordable hardware in recent times, the use of DPIV has become not only possible but highly desirable.

2.4.2 DPIV experimental system

The CCD camera used for these experiments was a Kodak Megaplus 4.2 which has an array of 2024x2024 pixels. Images can be acquired by the camera and saved in memory situated on a frame-grabbing board, then saved to the hard disc of a PC at a later time. The size of the frame-grabber memory determines how many sequential images can be acquired in a single experimental run. A balance between the requirement for high resolution and the requirement for a number of sequential images needs to be determined. Software was developed by

the author to allow the sequential acquisition of images by dividing the memory available into smaller buffers, allowing seven 2024x2024 pixel images to be stored. The minimum time in which these images could be acquired was limited by the frame-rate of the camera.

Multiple images were obtained at the required phases of the flow, filling up the memory. These were then saved and the experiment was ready for repetition. DPIV is therefore capable of building up a large database of information very quickly, allowing temporal and spatial records to be acquired, repeated and available for analysis in a reasonable time period.

The data was then shunted over the network to a computer where it could be analysed in large batches using analysis software developed within the Fluid Dynamics unit at Edinburgh.

2.4.3   Camera resolution limitations

As discussed, the resolution of the CCD array is a crucial factor in DPIV. Work done by Prasad *et al* [51] has shown that errors produced at the analysis stage are heavily dependent on the resolution. They presented the variation in error due to the combined contributions of the bias and random errors, with the ratio of the particle image diameter to the pixel width (d_τ/d_{pix}). The bias error is due to the uncertainty in locating the centre of a particle image, while the random error is due to effects such as a high velocity gradient in the interrogation region, pixel readout noise and imperfections in the particle images. The random error increases slowly with a larger ratio while the bias error increases quite rapidly at small ratios. They reported that the minimum error was achieved when the ratio $d_\tau/d_{pix} \approx 2$. However, there were additional influences such as the choice of peak locating technique and external limitations on the irregularity of particle images, that had the effect of increasing this value.

The value of this ratio is effectively determined by the type of lens used and the distance that the camera is from the region of study. For a given array size using a particular lens, getting too close to the flow would produce a large value of d_τ/d_{pix}, increasing the random error and also requiring a large (and therefore computationally expensive) interrogation region for the analysis. Too far away from the flow and the bias error would be significant and the analysis would be very inaccurate.

The size of a particle on a PIV image is given by Adrian [3] as:

$$d_\tau = (M^2 d_p^2 + d_s^2)^{1/2} \qquad (2.4)$$

where M is the magnification, d_p the actual size of a seeding particle and d_s the point response function for the lens ($d_s = 2.44(1 + M)f\lambda)$). A typical f-number would be 2.8 or 4, with magnification of approximately 0.03 giving particle image sizes of the order of $4.5\mu m$ on the CCD array. This gives theoretical values of d_τ/d_{pix} as 0.5 - 0.25. These values are an underestimation and do not account for out of focus effects, lens aberrations, pixel noise and the effect of the water and glass in the wave flume.

From the experiments the ratio was measured to be about 6 which is large compared to the values that were quoted by Prasad [51]. However, the choice of Gaussian curve-fitting as the correlation-peak detecting routine and, the fact that images are acquired directly onto CCD array (not onto wet film then CCD array, hence reducing the particle image irregularities), consequently means that the optimum practical ratio of d_τ/d_{pix} is much increased. If the use of other typical array sizes such as 1000×1000 or 700×500 is considered, under otherwise identical experimental conditions, the ratio will be reduced and in danger of being in the range where the bias error is large. It was found practically that this was the case and measuring the flow using the smaller resolution cameras was very difficult.

2.4.4   The effect of image shifting

Image shifting is an essential component of the experimental technique, however, there is a price to be paid for the advantages that it provides. There is a loss of resolution due to compressing all particle separations into the range of separations that are analysable. This is a direct consequence of the introduction of an additional velocity to the flow.

It is important to use the smallest possible shift-velocity so that the loss in resolution is minimised. However, the experimental system could only be programmed with one shift-velocity during the acquisition of a sequence of images. With the flow being decaying turbulence, the shift velocity was determined by the nature of the flow at the instant of the first acquired image. Therefore subsequent images were over-shifted and would not be utilising the maximum resolution available. Furthermore the shift velocity had a minimum of $5^o s^{-1}$. Therefore, if the camera is taken further from the study zone in order to capture a larger field of view, the shift will automatically get larger ($v_s = 2wL$ where w is the angular rotation rate and L is the mirror to measurement zone distance). The loss of resolution due to this effect is unavoidable. The effect of a larger shift velocity spreading multiple images further across the PIV image cannot be countered by lowering the illumination pulse separation time and the exposure. To do so has the effect of introducing a corresponding loss in accuracy and resolution of the technique. Decreasing the exposure also decreases the illumination on the array to such an extent that the analysis of the image can become impossible.

2.4.5   Digital analysis

The digital autocorrelation technique has been described earlier in this chapter. Some thought must be given to the size of the interrogation area used in the

analysis (the size of the small subsection of the image that is taken to be analysed to yield one vector). There are a number of factors to consider that have an important affect on the size of this area. There is a lower bound on the number of particles N, within an interrogation area such that $N > 15$, with the ratio of truncated particle images to full images required to be small. This problem can be easily overcome by seeding the flow heavily, being careful not to do so too heavily due to the possibility of diffraction limiting the identification of individual particles. This was a recurring problem in the breaking wave study as there is often a large injection of pollen into the flow when the wave breaks, due to the tendency of pollen to rise in the water. This was successfully limited by gently tapping the water surface prior to an experiment.

Conversely the interrogation size cannot be too large due to the computation taking too long and more importantly, the requirement of the velocity variance within the interrogation region to be small.

Practically, the limitations of the experimental system dictate the particle separations and sizes on the CCD array, with the interrogation size being chosen accordingly. The ideal particle separation is approximately 0.25 x Interrogation width. Since a particle typically covers approximately six pixels, the realistic choice of interrogation area is 64x64 pixels. In general the 32x32 pixel size produced reasonable velocity information but with a greater number of erroneous vectors. This would be particularly true with lower resolution cameras where errors due to biasing of the correlation-peak detection, and the difficulty in achieving small particle separations with image shifting became predominant.

After analysis erroneous vectors could be filtered by thresholding the signal to noise ratio of the correlation measurement for each vector. The velocity values at these points could then be interpolated from surrounding values. This is discussed

in chapter 3.

2.5   Experimental facility

Experiments were performed in the wave flume at Edinburgh University, originally designed and built by Dave Skyner [60]. Two contrasting breaking waves were chosen for the purpose of the experiments.

2.5.1   Wave Flume

The flume is 9.8m long 0.4m wide and has a still water depth of 0.75m, it's construction is shown in figure 2.6. It consists of three sections with an absorbing beach at one end and a wave-making paddle at the other.

The paddle is hinged at it's base and is driven by a motor connected to a drive belt. The paddle also contains a force transducer so that while outputting the programmed wave signal it can also absorb any reflections. This is a very important component of the paddle as it enables the water to become still much sooner after breaking due to remnant reflections being absorbed. This is advantageous in shortening the time after a wave breaks before another experimental run can be performed. The wave paddle is controlled by a PC via the wave generating software (written by Edinburgh Design) which can produce a variety of wave spectra and types. For the purpose of this study a breaking wave is generated by focusing a number of separate wave components at the desired point in the flume. In this case an upper and lower frequency limit on the spectrum is specified along with a slope in the spectrum between the limits. The software then calculates the various phases to ensure focusing of the components at the desired point in the flume. The wavemaker paddle always had a ramp-up time of two seconds to avoid an initial impulse paddle movement. The waves used, had
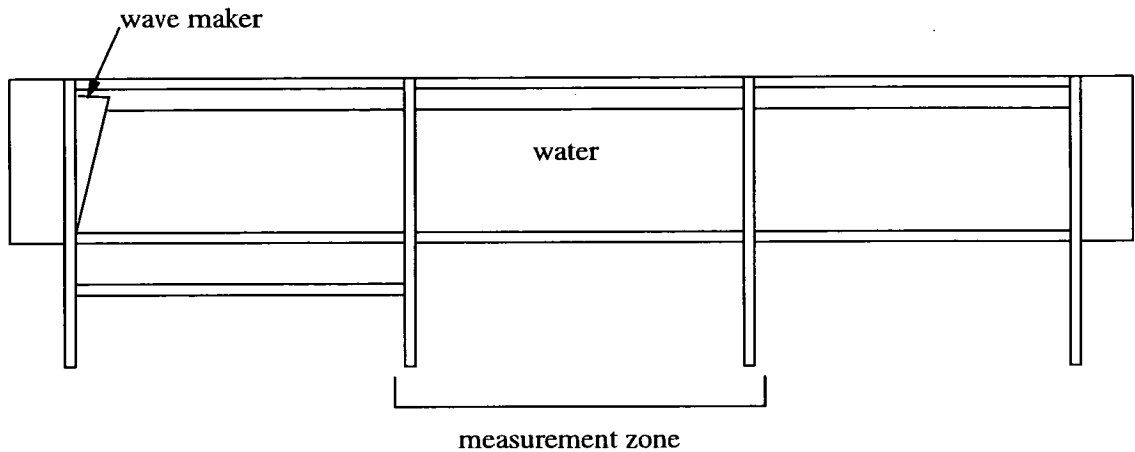
Figure 2.6: The wave flume.

thirty-one components to the spectrum separated by $0.0312 Hz$. This method is believed to model the naturally occurring mechanism of unsteady breaking in the field.

By varying the gain on the output signal the strength of the breaking event can also be controlled. If the gain is small the waves focus without breaking and then disperse, travelling to the end of the tank where they are absorbed. As the gain is increased a very gentle spilling breaker with a small amount of white water is observed, a further increase eventually produces a plunging breaker. If the gain is then increased even further, a point is reached where two breaking events occur.

The controlling PC also samples channels that can be connected to wave gauges to measure surface elevations and, to a position transducer to measure the positional output of the wave paddle itself. These two measuring devices will be detailed later in this section.

The absorbing beach at the other end of the flume is a wedged shape passive absorber which absorbs most of the waves reaching it, limiting reflections into the experimental region to a minimum.

22
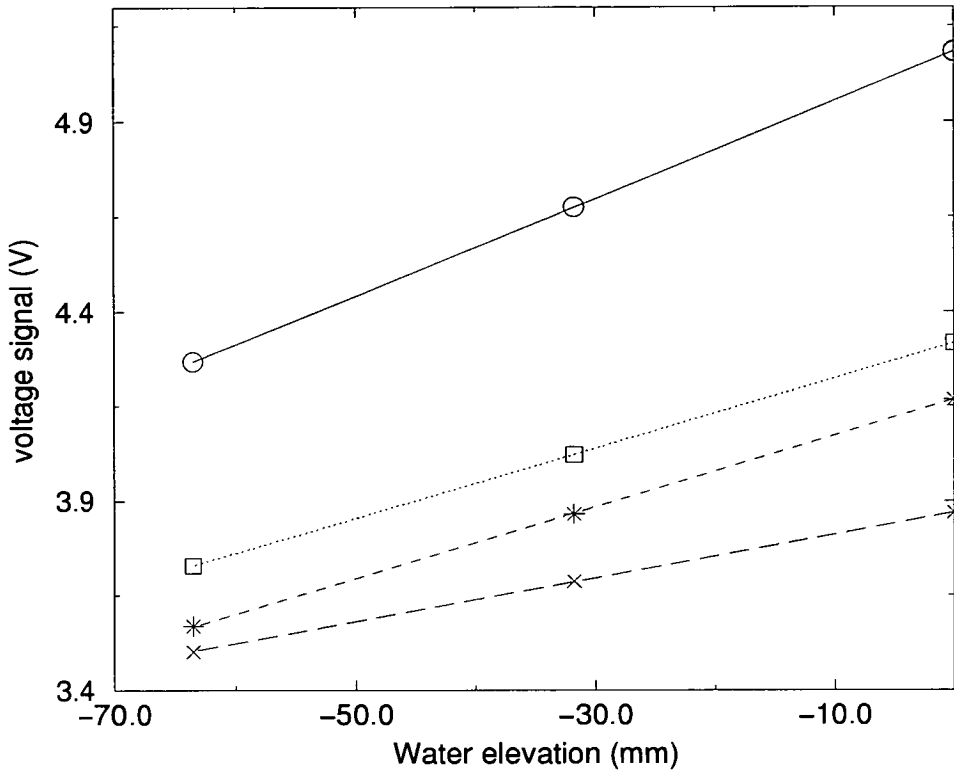
Figure 2.7: Calibration graphs for the four wave gauges.

The walls and the base of the flume are made from thick high quality glass which allow the experimental regions to be optically accessed by the illumination and image acquisition systems.

2.5.2 Wave gauges

The wave gauges are used to provide accurate water elevation information at various positions as a function of time. This is important for monitoring the repeatability of the waves, the loss of energy in the breaking region and the energy of the waves themselves.

The gauges are conductive and consist of two parallel vertical rods whose

conductivity is proportional to the depth of water in which they are immersed. These are carefully calibrated, by measuring their still water response when the depth of immersion is varied. This is done by using spacers on which to rest the gauges. The response is shown to be linear in the calibration graph (figure 2.7). This calibration was repeated on every new day that experiments were performed to account for temperature variations in the water that may influence the response of the gauges. The gauges were sampled at a rate of 16 samples per second.

2.5.3   Position transducer

The position transducer is a device for measuring the exact position of the wave paddle as a function of time during the generation of the wave components. It consists of an extendible spring loaded wire connected to a potentiometer. The base of the transducer is secured at a fixed point and the wire is connected to the paddle. When the paddle and wire move the output voltage of the transducer varies and is sampled by the PC. The transducer was calibrated by extending it by accurately measured distances and sampling its output. The data from this device is not used directly in this thesis, its use is for further work on comparisons with numerical wave-flumes where the experimental conditions can be mirrored exactly by specifying the movements of the paddle.

2.6   Experiments

Two different waves were generated from the same input spectrum parameters by varying the voltage gain of the signal to the paddle. The surface elevations were sampled at four different points, two before breaking and two after.

For each breaker, a time sequence was acquired and then repeated a number of times. This was then repeated at several different positions starting from the

breaking point and covering a total distance of 1.70m in the downstream direction. The CCD camera was triggered from the PC that controls the wavemaker, with the timing being referenced to the clock cycle of the wavemaker. The interval between successive acquisitions was normally 0.75s. Intervals much lower than this were not achievable due to limitations on the reset time of the image shifter and the frame rate of the camera.

Care was taken to ensure that the fluid motion decayed to a small level before repeating another experiment.

Chapter 3

Data Analysis Techniques and Wave Theory

3.1 Summary

Techniques and methods used to process and analyse velocity vector information are outlined in this chapter. Velocity vector maps are a very useful visual tool for studying the flow but by further processing the data, additional characteristics can be displayed. An outline of the method used to extract turbulent velocities from the measured flow is presented. This is central to much of the analysis performed in later chapters. The procedure for accurately calculating vorticity and subsequently circulation are introduced along with energy and velocity profiles and power spectra.

Also a brief outline of linear wave theory and present theories on breaking waves is contained in this chapter. Finally the methods and justification of scaling the experiments to the ocean situation is discussed.

3.2 Vorticity and circulation

3.2.1 Vorticity

Vorticity is very useful as an additional flow-visualisation tool. The visual impact of a velocity vector map is limited. Since the flow studied here consists of various coherent structures, the use of vorticity maps with velocity vectors overlayed provides a good visual representation of the spatial flow structures.

Vorticity for a velocity field is defined as the curl of the velocity field (see Tritton [67]). In practical terms, from a two-dimensional PIV velocity map, the vorticity at a vector point (i, j), that has a velocity value $(u_{i,j}, v_{i,j})$, is given by

$$w_{i,j} = \frac{(v_{i+1,j} - v_{i-1,j})}{2\Delta x} - \frac{(u_{i,j+1} - u_{i,j-1})}{2\Delta y} \tag{3.1}$$

where Δx and Δy are the x and y dimensions of the vector grid. Due to this calculation producing large errors in the vorticity, a smoothing kernel was applied to the surrounding velocities and the vorticity calculated from these smoothed values. This is not the only accurate method, vorticity can also be calculated from the eight surrounding points [69].

There are problems with vorticity calculations near the surface of the flow due to the surface not being flat, leaving only partially complete lines of vectors. With lots of absent vectors it becomes very difficult to interpolate the velocities at these positions, implying that any calculated vorticity values are highly erroneous. Therefore, the first few lines of velocity values are generally disregarded and vorticity ignored. There were often a very small number of outlying vectors (obviously noisy vectors) in the main body of the flow. The smoothing routine described above also acted to interpolate velocity values at these points, so that reasonable vorticity information could be obtained.

3.2.2 Circulation

Circulation is a useful concept, it can be easily calculated and gives a measure of the vortex strength. Circulation around a simple closed loop is given by the line integral of the velocity (see Saffman [58]).

$$\Gamma = \oint_C \underline{u}.\underline{dr} \tag{3.2}$$

It follows from Stokes theorem that this is equivalent to the flux of vorticity through a surface S bounded by the curve C. That is to say that

$$\Gamma = \oint_C \underline{u}.\underline{dr} = \int_S \underline{w}.\underline{dS} \tag{3.3}$$

The circulation therefore gives a measure of the vortex strength.

From PIV data the circulation can be calculated by just summing the N vorticity values within the loop and multiplying by the area, A_i, of each gridcell:

$$\Gamma = \sum_{i=1}^{n} \underline{w}_i A_i. \tag{3.4}$$

3.3 Data manipulation

3.3.1 Separation of turbulence from mean-flow components

In order to study the evolution of the turbulence produced at the instant of breaking, it is essential that it can be distinguished from the non-turbulent flow. The contributions to the motion within the surf-zone are steady-current, periodic-wave and turbulence. There is also an additional contribution from large-scale rotational motion that is not turbulent. This is produced by the shearing of the mean surface-current on the remainder of the flow and has a significant magnitude [64]. Therefore the motion can be defined as having the contributions mean-current, periodic-wave, large-scale rotational motion and fluctuating motion [49] [46].

For experiments performed with LDA or LDV the mean motion is often defined by the result of averaging the LDA signal over many repeats. Nadoaka *et al* [46] states that this still does not account for the fluctuating part of the velocity that is not turbulent and is associated with the unrepeatability of the wave paddle. Also it assumes that all non-turbulent contributions that are a consequence of the wave itself, are perfectly repeatable. Nadoaka [46] decided upon a numerical filtering method which essentially involves choosing a cut-off frequency above which the motion is regarded as turbulent. This makes the equally incorrect assumption that there is no overlap between the scales of turbulent and non-turbulent motion.

Thais and Magnaudet [64] use a more complicated two-stage method to overcome this. Firstly, the motion due to the waves is extracted through determining the instantaneous stream function from a detailed knowledge of the behaviour of the free surface. The second stage then just relies on linear filtration of the remaining rotational orbital motion, leaving the turbulent fluctuations.

The problem of wave and turbulent motion being mutually superimposed in the frequency domain is recognised as being unavoidable in this study. There are not enough repeats to obtain mean motion from ensemble averaging, and the knowledge of the instantaneous surface fluctuations is not sufficient to enable the wave components to be calculated from it. Therefore the most accurate method available is to simply locally filter spatial frequencies at an appropriate wavenumber. This has limitations that have been highlighted above, but careful choice of the wavenumber at which to filter will limit the inaccuracies due to overlapping of the large-scale non-turbulent rotational motion and large scale turbulence.

The frequency spectrum of the surface profile just after the breaking point

is shown in Figure 3.1. The fundamental harmonic in this spectrum is the most intense peak and occurs between the specified upper and lower limits of the input wave paddle spectrum. The second harmonic can be seen quite clearly between frequencies of about 1 and $2Hz$ but subsequent harmonics are not quite so clear as there is significant overlap. There are no significant peaks further down the spectrum, indicating that the wave component contribution to the motion is small above $2Hz$.

A frequency of $2Hz$ corresponds to a spatial wavelength of approximately $40cm$, well above the observed upper limit on the size of turbulent structures in this study. Therefore, the concern is with the overlap of the large-scale non-turbulent motion and the turbulence itself in the spatial domain.

It was decided from visual inspection that most turbulent fluctuations would be of a smaller size than $15cm$, which seemed to be an upper limit on observed vorticity sizes. Furthermore it is the order of the wave amplitude, implying that this is likely to be a physical upper limit on the size of a turbulent fluctuation. $15cm$ corresponds to a frequency of $3.2Hz$

The practical method of filtering out all motion which has scales larger than $15cm$ (19 vectors), is to calculate the local average at each point in the vector map, over a grid size of 19×19 vectors. This value can then be removed from the central velocity value to give an estimate of the turbulent velocity component at that point. This was easily done with a UNIX script.

In figure 3.2 two horizontally integrated vertical velocity profiles are shown for the two different waves. The feature shown here which is common throughout almost all such profiles is the characteristic shape, showing a decrease in the horizontal velocity component until it reaches a minimum at around $0.006v_p$, it then increases below this point. This feature is characteristic of the recirculation
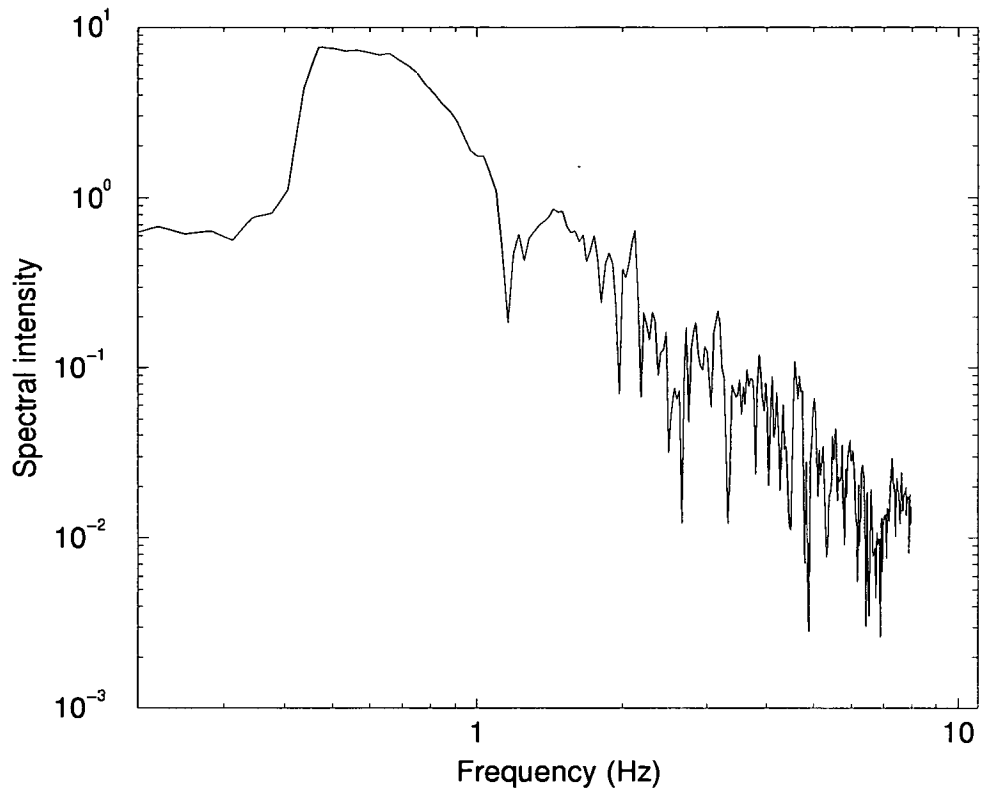
Figure 3.1: Surface profile spectra for a probe placed just after the breaking point.
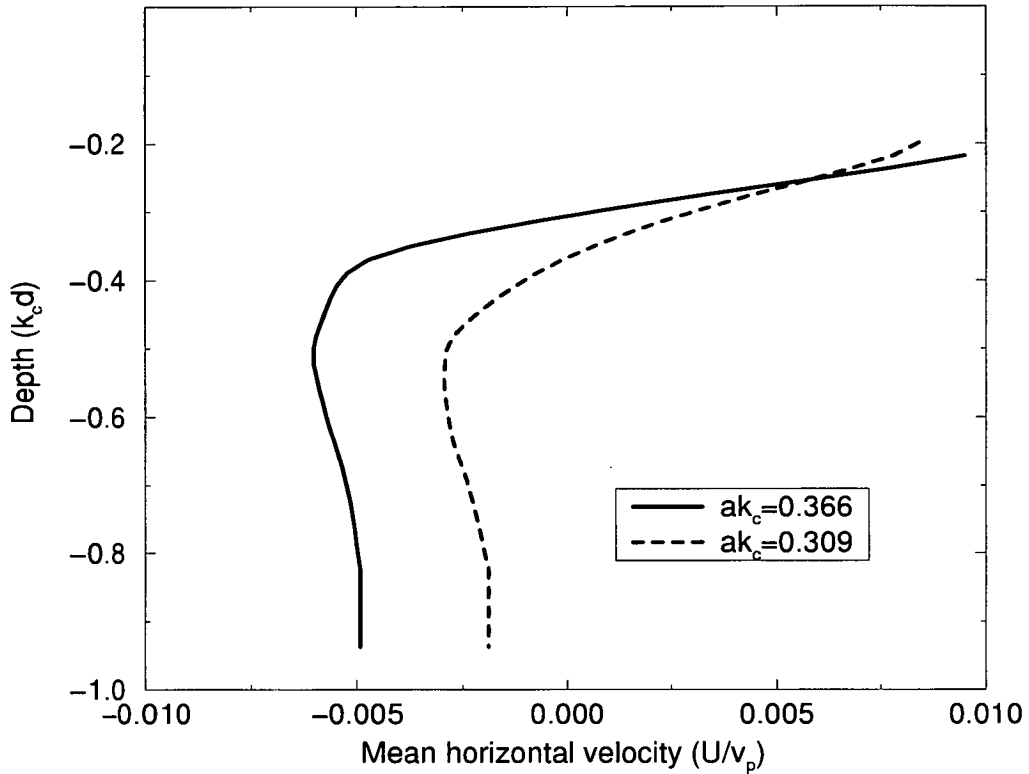
Figure 3.2: Vertical profiles of horizontal velocity components for the mean motion calculated using the spatial grid method.

that occurs in these such experiments and is a highly repeatable and hence non-turbulent effect. This feature is slightly less obvious at instances when there is significant wave motion traveling through the experimental region.

3.3.2 Smoothing

In section 3.2.1 the smoothing of data in order to display vorticity information was discussed. When measuring turbulent quantities it is important not to smooth away small scales that make a legitimate contribution to the turbulence. However, if the noise level of the experimental technique could be identified, then smoothing

over these scales would be highly desirable. In section 3.4.2 it is stated that the realistic size of a spatial fluctuation that can be resolved is two-vectors wide, so smoothing over two vectors is considered legitimate.

3.4   Presentation of data

3.4.1   Energy and velocity profiles

Depth profiles were calculated from the PIV data by averaging horizontally across the flow for each row of data. The rms horizontal turbulent velocity component, u_{rms}, and the estimated turbulent kinetic energy, $u^2 + v^2$, were both presented in this way.

The turbulent kinetic energy value does not include the third (out of plane) component which is impossible to measure using the present PIV system and therefore difficult to estimate (it can be measured using stereoscopic PIV [5] but this is in its early stages of development). The validity of omitting it depends on the assumptions that firstly, it is small compared with the two in-plane components and secondly, it does not change significantly over the time-period that data is taken. The first assumption is likely to be correct, we know that the flow is strongly two-dimensional from observations of long-lasting coherent structures that often appear in similar positions from one wave to the next. The second assumption is unlikely to be valid because increasing isotropy with time is a characteristic feature of breaking wave flows (Battjes and Sakai [8]). In a similar calculation Rapp and Melville [56] approximated the third turbulent component to be of the same magnitude as the vertical component, stating that this seemed to be a better assumption than setting it to zero. This is more likely to be a good assumption for a long time after breaking than for the time period used in this study, where, although the value of this component will increase it should

still remain small compared to the other two components. Therefore the third component was ignored.

Another important assumption that is made in the calculation of the depth profiles, is that the turbulence does not have a different character at different positions across the vector map. If the turbulence is occurring in patches which are mixed to different depths and more than one patch occurs in one of the experimental regions, then this assumption will be violated. The regions studied were carefully chosen so that the distinct patches could be studied without too much flow into or out of the study region. This was never perfectly achieved although it was always assumed that it would only be a small perturbation on the main effect. There was more overlap of different turbulent regions in the study of the spilling breaker. This was not too much of a problem as the different regions appeared to have similar properties. There will be some decay in the horizontal direction which will result in the profiles being weighted towards the higher intensity turbulence. This was regarded as an acceptable error that is unlikely to have an effect on conclusions made from the profiles.

3.4.2   Power spectra

A common method of analysing a random stationary function is to calculate it's power spectrum. This concept is introduced in books by McComb [43] and Frisch [24]. In turbulence, the spectra represents the fundamental cascade of energy from low to high wavenumber or the transfer of energy from large scales to small scales.

If the horizontal velocity values of the nth line of vectors in a flow map is regarded as a function $U_n(x)$, its Fourier Transform ($F(U_n(x))$) is a function of wavenumber k and is given by

$$S_n(k) = F(U_n(x)) \tag{3.5}$$

The power spectrum, $E_n(k)$ is obtained by squaring the modulus of this function:

$$E_n(k) = |F(U_n(x))|^2 = |S_n(k)|^2 \tag{3.6}$$

The power spectrum of a single line of vectors calculated using this method is likely to be a noisy function due to the low sampling rate (there are only about 60 vector points across one vector map). The power spectra were therefore averaged over a number of horizontal lines at the top of the vector map to obtain a more accurate and smooth spectrum. The justification here was that if the top region of the flow field was considered roughly homogeneous, then the spectra could be assumed to be similar throughout this region. In reality the spectra will change in character with depth due to the decay of turbulent flow velocities with depth, although this is shown to be quite a small decay in the upper regions (see chapter 5). Therefore the power spectrum obtained from a single velocity map is given by:

$$E(k) = \frac{1}{n_2 - n_1} \sum_{k_{min}}^{k_{max}} \sum_{n_1}^{n_2} E_n(k) \tag{3.7}$$

Where n_1 and n_2 are the start and finish lines in the vector map and k_{min} and k_{max} are the wavenumbers corresponding to the maximum and minimum spatial frequencies.

Programatically this calculation was achieved by performing a Fast Fourier Transform (FFT) on each of the 20 horizontal lines of horizontal velocity values nearest the water surface (the top 2 lines were disregarded as they tended to be very noisy and often had information missing). From this, the power spectrum was calculated for each line and averaged over each spatial frequency.

To perform an FFT the data sample must have 2^n values, which was ensured by padding the data sample with zeros. This is a commonly used fourier technique that is discussed in most standard text books on the subject (see Bracewell [11]).

The spectra seemed to be noisy at high wavenumbers so all spectra were cut off at a wavenumber that corresponded to a spatial structure of two-vector separations in size, which is the limit of a size of structure that can be resolved using PIV.

3.5 Computer analysis

In the previous sections a number of quantities that could be derived from the original raw PIV data were introduced. These were calculated using C programs or UNIX scripts. The raw PIV data consisted of 4 repeats of sequences of 7 images at 4 different positions for 2 different waves, a total of 218 PIV images each with approximately 3600 vector points. The analysis requires smoothing functions, spectral analysis, local (spatial) averaging, energy and velocity profile calculations and data scaling functions to be performed. All computer programs were written by the author or developed from routines originally written by David Hann (smoothing and spectral analysis functions) [30].

With such an extensive data set and a large number of separate UNIX and C programmes to be executed it was important to coordinate the analysis effectively. This was done by using C-shell scripts in UNIX which allowed all the analysis programmes to be executed on each PIV image in turn, outputting the relevant data in specified files.

3.6 Waves

3.6.1 Linear theory

Linear potential theory gives a good approximation of the flow within water waves, providing they are small amplitude and the motion is irrotational, incompressible and inviscid. If this is the case then the velocity potential satisfies

Laplaces equation (see Sawaragi [59] or Rahman [55]). Using suitable boundary conditions at the surface (Bernoulli's equation) and the sea-bed this can be solved to yield the results below (for a wave traveling in the positive x-direction).

$$\phi = \frac{ga}{w}\frac{\sinh(k(h+z))}{\cosh(kh)}cos(kx - wt) \tag{3.8}$$

Where a is the wave amplitude and w the angular frequency, given by the dispersion relation

$$w^2 = gk\ tanh(kh) \tag{3.9}$$

The horizontal and vertical velocity components can be determined from equation 3.8 as

$$u = aw\frac{\cosh(k(h+z))}{\sinh(kh)}cos(kx - wt) \tag{3.10}$$

$$v = aw\frac{\sinh(k(h+z))}{\sinh(kh)}sin(kx - wt) \tag{3.11}$$

For deep water where $h/\lambda > 1/2$ then $tanh(kh) \rightarrow 1$, which leaves the deep-water dispersion relation.

$$k = (2\pi f)^2/g \tag{3.12}$$

Finally the waves travel with a phase velocity

$$v_p = \frac{w}{k} \tag{3.13}$$

3.6.2 Breaking wave theories

Although there is no absolute theoretical description of the nature of wave breaking there are a number of theories that help describe and clarify the process around the time that breaking occurs.

Stokes theory for small amplitude waves follows from linear theory and predicts that at breaking the surface profile of the breaking crest has angle of 120°. This has been confirmed by experimentation to be the case when the ratio of the depth to the wavelength (h/λ) is greater than $1/10$.

Other conditions required for breaking are that breaking occurs when the horizontal component of particle velocity at the wave crest becomes faster than the wave celerity and that the progressive wave loses it's symmetrical shape. The result of these theories are that the commonly used limit for deep water breaking waves is that $(H_0/\lambda) = 0.142$, where H_0 is the wave height at breaking (approximately double the maximum wave amplitude).

There are a number of different classifications of breaker type. The two important classifications here, are the plunging breaker and the spilling breaker. Knowledge of these have already been assumed but a formal definition seems appropriate.

A plunging breaker shows a very asymmetrical profile with a steeper front face compared to the back surface. When it breaks the crest curls over a large air pocket, entraining air and producing a large vortex or surface roller. This is normally followed by one or more splash-ups.

A spilling breaker is not quite so asymmetric and is characterised by the appearance of white water at the crest. The wave generally breaks slowly, with turbulent water spilling down the front face.

Explaining either type of wave more extensively has proved difficult, which probably has resulted in the lack of numerical simulations that cover the instant that the wave breaks. Bonmarin [10] described the plunging process qualitatively and produced some simple but effective descriptors.

Descriptions of spilling breakers have been attempted for modelling purposes

by Peregrine [6], with opinion on the best approach divided. The spiller is sometimes regarded as a surface roller riding almost passively on the water and otherwise described by considering the whole region of turbulence where the roller is continuously mixing with the rest of the turbulent fluid in the wave.

The source of the turbulence is not completely clear. The water falling down the front face of the wave is an obvious contribution to the turbulence but the main source is suggested to be from the shear between the turbulent region and the previously undisturbed water, due to the large velocity differential between the two water masses. This theory for the source of the turbulence can be extended to plungers where there is a large mixed-up region of fluid dumped into the flow at breaking, the shear from the rest of the flow subsequently produces vortical and turbulent motion.

3.7   Scaling of wave parameters

In order that comparisons can be made between different studies by independent researchers, some convention must be used by which to non-dimensionalise the various wave parameters. The standard used in this thesis essentially follows that employed by Rapp and Melville [56].

The important parameters that characterise the wave itself, are the non-dimensional amplitude and the bandwidth of the input frequency spectrum. The wave amplitude is non-dimensionalised using the central wavenumber of the input spectrum, k_c. The bandwidth of the input spectrum is given by $\Delta f / f_c$ where f_c is the central frequency of the spectrum.

The central values in the spectrum were calculated directly from the input spectrum values calculated by the wavemaking software. The spectrum was not a simple flat-topped spectrum but was specified by an upper limit, lower limit

and a slope between the two. The central frequency of the spectrum was therefore calculated as a weighted mean and the central wavenumber value calculated from the deep water dispersion relation in equation 3.12.

The velocities were scaled with the phase velocity of the central component of the wave packet. It therefore followed that the turbulent kinetic energy per unit mass was scaled with the square of the phase velocity. No convincing justification can be made for using the phase velocity as the scaling parameter for the velocities; the reason for its use here is to emulate the method used by Rapp and Melville [56].

Using the results obtained from linear theory earlier in this chapter, the scale of velocities that are present in the waves used in this study can be considered. The upper limit on the velocity under a wave can be approximated from equation 3.10 as

$$u = aw \qquad (3.14)$$

Using the method of scaling the velocities outlined above this gives an upper limit to the magnitude of velocities that might be expected in the flow, of ak. Measured velocities are very unlikely to be greater than this value as the measurements are taken after breaking, when the velocities have decayed from the pre-breaking value predicted by linear theory.

The values of the non-dimensional parameters for the waves used in this study and the scaling parameters themselves are presented in table 3.1.

Also shown in the table are the same parameters from the experiments of Rapp and Melville [56], whose results are used as comparisons throughout this thesis.

It is interesting to test the breaking criteria, introduced in section 3.6.2, in the context of this study. The value of (H_0/λ) is 0.116 for the plunger and 0.0985

Parameter	This study		Rapp study	
	plunger	spiller	plunger	spiller
f_c	0.7970	0.7970	0.88	0.88
v_p	1.9589	1.9589	1.7742	1.7742
ak_c	0.3656	0.3093	0.352	0.278
$\Delta f / f_c$	1.1762	1.1762	0.73	0.73

Table 3.1: Table of scaling parameters and scaled parameters for this study and the experiments of Rapp and Melville.

for the spiller. These were estimated using the wavelength of the central value in the spectrum and double the amplitude as the wave height. The reason that the values are significantly lower than the value from the breaking criteria could be due to the fact that high frequency waves contribute more to breaking than low frequencies. Therefore the use of the central frequency value could be argued to be unjustly weighted towards a low frequency value.

Chapter 4

Investigation of Vorticity and Circulation

4.1   Summary

In this chapter results are presented from experiments performed on two different deep water waves, covering an upstream distance of about 1.5m, over a time period of 4.45 seconds beginning 1.7s after breaking. Each sequence was repeated a number of times. The main regions of vorticity created by the action of the crest and the subsequent splash-ups are investigated using high-speed video footage and PIV velocity vector maps.

These flow-visualisation techniques are used to describe the breaking process in detail, emphasising the mechanisms that occur to produce the subsequent flow structures. The evolution of these structures is described. It appears that the early stages following breaking are not purely a time when structures decay, there is strong evidence to suggest that the subsequent flow is dictated by the events immediately following breaking.

The decay of the integrated vorticity (circulation) is also investigated in the region immediately following the point of impact of the plunging crest. This is extrapolated back to the breaking time and the value compared with an order of magnitude estimate for the circulation of the crest before breaking. 32% of the

initial circulation appears to be transferred into this region, a figure that could prove to be a useful comparison for future studies.

4.2   Experimental design

The precise regions of study are shown in figure 4.1. The regions overlap, providing a comprehensive investigation of the flow. This, however, creates difficulties in the presentation of information as the separate fields cannot just be tagged on the end of each other for visualisation. The precise position and time of breaking are difficult parameters to identify or define. The onset of breaking was defined as the time at which the input spectral components to the wavemaker were focussed. The triggering signal that caused the image-shifting device to activate and hence trigger the CCD camera, was produced by the wave making hardware. This was convenient as it enabled the instances that images were acquired to be accurately referenced to the breaking time.

The position at which breaking occurred has been indicated in figure 4.1 and was visually identified from high-speed video information, as the point at which the crest of the plunging breaker first hits the undisturbed water underneath. This becomes more difficult to identify with spilling breakers. Bonmarin [10] defined the onset of breaking for spilling breakers as the point at which foam occurs at the front face of the wave. Using this as the criteria in this study, it was found that the onset point was similar for the spilling and plunging breakers used.

The definition of the breaking position is not considered to be particularly accurate in the case of either breaker. There is not a large amount of importance attached to getting the value of this parameter exactly correct.
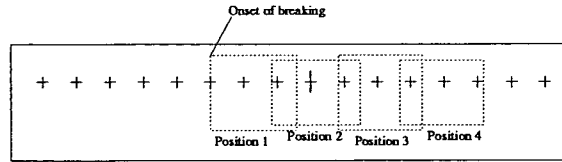
Figure 4.1: Regions investigated within the middle section of flume (wave travels left to right).

4.3   Inferences made from observations

Observations made from the video footage were very useful in describing general features of the flow, giving an overall picture of the process. All video information was acquired using a high-speed video camera borrowed from EPSRC, that acquired images at a frame-rate of $200s^{-1}$.

In the case of the plunging breaker there are distinct vortical regions that are left after breaking. It has been suggested that the plunging crest itself does not appear to physically create the vorticity but serves to mix up a certain mass of fluid that is dumped into the flow [22]. The main vortical region is then created by the shear on this mass of fluid from the exterior irrotational flow. This usually results in one or more long-lasting clockwise rotating vortex that translates through the measurement zone. The splash-ups can be said to have a similar effect but of less intensity, creating less obvious coherent structures which decay and dissipate into more chaotic structures quite rapidly.

The spilling breaker does not have the vigorous mixing effect of the plunging jet so a less intense vortical region is left in its wake. Fluid is introduced into the flow nearer the surface and appears to spread itself more evenly across the flow, leaving less distinct patches than in the plunging case. The structures are therefore of smaller scales but the mechanism suggested for creation of turbulence through shearing of the fluid mass, is the same. This process is similar to that

described by Rottman et al [57].

Using the observations made above as a useful starting point for a description, the PIV velocity record can also be used as a flow-visualisation tool to describe the flow. Figures 4.4 - 4.30 show a sequence of vorticity plots with velocity vectors overlayed for the plunging breaker. They all show sequences of seven realisations, beginning 1.7s after breaking and extending to 6.20s at 0.75s intervals, except position 1 where there are only six in the sequence.

Region 2 was identified from the video information as the region in which the main vorticity due to the initial impact of the plunging crest is deposited. Immediately it is clear that there is a relatively well defined patch of vorticity that moves across the region. The velocities on the upper side of this patch are very large, adding weight to the argument that the patch of mixed fluid is sheared by the rest of the flow. Figures 4.31 - 4.52 show a similar sequence for the spilling breaker for the same time period after breaking.

There are differences between the two cases that highlight the observations made from the high-speed video footage. A very large circulation can be identified in the plunging example, that in total, is of the order of half the region of study. The equivalent circulation in the case of the spiller is maybe only a quarter of the study region, however it only includes one vortex, whereas the plunging case appears to be a large scale circulation that contains complicated flow structures that could be described as being two or more separate vortices. Despite these smaller vortices, the main large-scale circulation is dominant and long-lived, still being very much in evidence in the final vector map of this sequence.

4.3.1   Plunging breakers

The plunging breaker produces turbulence in quite distinct patches, the first of which appears at a distance of about 0.25m from the original breaking point.

This patch is fragmented initially and moves slightly to the left at times 2.45s and 3.20s. This is a result of this patch being produced by water that splashed backwards at breaking and then more fluid being pushed in this direction by the large-scale circulation that exists to the right (next position). There is a coherent vortex near the surface and two pairs of smaller vortices at depths of 0.15m and 0.2m. The near surface vortex moves a small horizontal distance of about 5cm and overtakes the deeper vortices, which remains almost stationary. There is a slight sinking of these deeper vortices in the early stages from 0.15m depth to about 0.25m.

At position 2 the main mass of mixed fluid can be seen. It seems to get stretched and contorted during the sequence, presumably by the wave motion, causing the position of the patch to oscillate. The patch itself is not a single vortex but a number of separate structures that can be seen to almost separate at T=3.2s and 3.95s only to apparently recombine in the next image. The patch moves approximately 20cm during the course of the 4.5s that the information was acquired, without mixing significantly in the vertical direction. The vorticity dissipates most significantly between the final two realisations. The final notable feature is the existence of strong horizontal shearing velocities at the surface, which is the mechanism by which the coherent vortices are produced and maintained.

Position 3 shows a lot of small-scale motion spread evenly across the surface with a pair of coherent vortices initially at a distance of 1.1m after the breaking point and a depth of 0.2m. The vortex pair diffuse with time and travel slowly across the flow field. Again, the near-surface vortex translates further through the flow. This is a common feature in all flow fields presented here, and is likely to be a consequence of the shearing from the mean-wave motion being stronger near

the surface. The deeper vorticity mixes vertically in the early stages and then appears to rise in the final stages. It is difficult to make too much of a judgement regarding the vertical mixing from this dataset as the wave motion masks the true behaviour of the turbulence. A much longer time period for the sample would be required to reach any definite conclusions. The patch of vorticity in this section extends to a greater depth than in the previous region studied. It was expected that the deepest mixing would occur in region 2, due directly to the plunging jet. This result is therefore unexpected and is discussed in the next chapter.

At the final position, the majority of activity was confined to very near the surface and the structures were of smaller scales than elsewhere in the flow. Due to the overlap between the last two positions there was some considerable flow of structures that were studied in region 3, into this region. These structures have a different form in the data for region 4 than for region 3, where they were mixed to a greater depth. This highlights a feature of the flow where sometimes, the turbulence appears to be pumped downwards into deep water and on other occasions, seems to be carried more in the forwards direction. This was also identified in Bonmarin's [10] qualitative study.

4.3.2   Spilling breakers

At position 1 the turbulent patch begins slightly closer to the point of breaking than for the plunger. This is at a distance of approximately 0.2m after the theoretical breaking point. As with the plunger there is a movement backwards between the first two frames. The patch then moves away forwards quite quickly, reaching a distance of 0.35m by T=5.45s. The scales of the structures are smaller than for the plunger. The depth of mixing is about 0.2m, which does not change much over the whole sequence. However, there are a pair of vortices that are separate from the main patch that begin on the far right at a depth of 0.15 and

eventually sink to depth of 0.2m.

Position 2 shows a number of small vortices spread along the near-surface region of the water in patches that are much closer together than in the example of the plunging breaker. The far left vortex hardly moves at all, changing its position by only approximately 5cm in the time period of 4.5*s*. This is also true of the middle vortex and the more chaotic patch at the far right, the main body of which moves out of the region by the final frame.

In position 3 a concentrated patch of mixed-up fluid can be seen at the far left of the flow-field, consisting of several positive and negative vortices. In the subsequent fields these vortices diffuse from their original compacted positions, spreading both down and across the flow. The most intense vortex in this collection, a negative vortex near to the surface, moves horizontally from 0.85m to 1.07m downstream of the breaking point. A large amount of this movement seems to occur between the times T=5.45s and T=6.2s. The downward mixing is of the order of 5cm, from a depth of 0.15m to 0.20m. There is another separate vortex very near to the surface at a depth of just 5cm that moves across the region from 1.1m to 1.25m and mixes vertically down to a 0.1m depth, although it does seem to do something erratic in the very last flow-field where it rises towards the surface. This again lends credence to the argument that there is a strong wave component that shifts all the motion at this particular instant, momentarily disguising the true positions of the structures.

The furthest downstream position shows very little vorticity or turbulence. There is a small amount near the surface, although it is very difficult to see if this is vorticity or just edge effects. There is a small amount of flow into the region towards the end of the sequence.

4.3.3 Conclusions and explanations from visualisation of plunging and spilling breakers

There are some important points that need to be reiterated concerning the features of the vorticity maps. There are both general similarities and fundamental differences for which explanations should be attempted.

The most obvious difference is the contrast in the form of the turbulent region left behind after breaking. The scale of the structures in the wake of the plunger are generally larger more intense vortices compared to those in the case of the spiller. They appear to be formed in definite distinct patches that do not seem to merge together at any stage.

In the spilling case the smaller structures are almost evenly distributed through the post-breaking region. Splash-ups do occur in this case but manifest themselves in the form of a near continuous set of vortices. This is similar to the structure of the wake behind a steady spilling breaker where there is a continuous stream of discrete structures.

It is no surprise that the depth to which the vortices mix is greatest in the case of the plunging wave. It is however unexpected that the deepest mixing occurs in region 3 and not region 1 or 2 where the effect of the plunging jet might have caused increased deepening. On further inspection of the high speed video information the reason for the above can be identified.

As the wave breaks the crest hits the undisturbed water, causing entrainment of air and a body of mixed-up fluid. This also causes a splash-up which hits the undisturbed water further downstream. A similar mixed-up region now exists here. However, immediately following this, a secondary surge from the large scale circulation that follows the initial breaking, travels over the top of this second turbulent patch pumping it both forward and downwards. As stated in

the previous section, this occurs to various degrees, causing an inconsistent depth of mixing that is generally the maximum. Even though there is no such dramatic plunging event in the spilling breaker this effect is still noticeable.

On examination of the two distinct regions identified for the plunger, the vorticity appears to be nearly exclusively negative in the main patch (as seen in region 2), while being a mixture of positive and negative in the subsequent patch (as seen in region 3). This is because the shear and circulation are very strong in the vicinity of the main patch. These effects are instrumental in the generation of vorticity resulting in negatively rotating vortices dominating. The splash-up however, has less of an intense circulation associated with it and does not have such strong forward motion, in which case vortices of both senses are more likely to exist.

The vorticity present in the region closest to breaking in the case of both waves, seems apparently separate from the main patch in region 2. It is caused by the same process as the main patch but is produced by fluid that is left behind, having been pushed backwards after the impact of the initial crest. This is supported by observations made in the previous section, where it was clear in the early stages that the vorticity in region 1 moved back towards the breaking point.

Perhaps the most interesting feature that is displayed by the vorticity and velocity maps for both waves, are the indication that during these early stages following breaking there are still processes occurring that are not only affecting the nature of the turbulent region, but are involved in the production of turbulence. For example, the heavy contortion of the turbulent patch early in the sequence and additionally, the dissipation and diffusion of vorticity that seems to occur in the final stages, provides evidence to this effect.

The motion of the discrete vortices that are formed in the flow seems to be dictated by their position. It is consistently evident that deeper vortices travel at a smaller horizontal velocity than those nearer the surface.

Finally it is worth noting that rather than being a completely separate case the spilling breaker appears to be a weaker example of the plunging breaker. This is not only suggested by the video information but also by the presence of similar structures of generally smaller scales. This is mentioned by Banner and Peregrine [6] where they state that a spilling breaker often appears to be very small scale plunging event.

4.4 Circulation

Circulation is a convenient quantity to measure from the vorticity maps because it is easily calculated by summing individual vorticity values, providing a value for the strength of the vortex. It seems logical to compare the circulation after the breaking event with an order of magnitude calculation before breaking.

4.4.1 Circulation at breaking

Care must be taken when considering circulation before breaking as there is no circulation around any point within a potential flow. However, irrotational flow about a torus can have non-zero circulation around curves which thread the hole. In order to apply this to the wave before breaking it must be assumed that at the instant that the plunging jet hits the forward face of the wave the flow is fully connected. In addition to this, the comparison itself implies the assumption of the conservation of circulation. Generally circulation is conserved in an ideal barotropic fluid acted on by conservative forces.

Despite no formal proof that either of the above assumptions are justified, the

relationship is worth investigating as it would provide useful details on how the activity of the wave distributes itself in the breaking region.

In order to calculate the circulation at the breaking point, the instant at which the jet tip hits the forward face of the wave should be considered (see figure 4.2). Up to the point shown the flow is essentially irrotational (see Skyner's thesis). Consider 2 simple, closed curves C_1 and C_2, where the curve C_1 traces out the boundary of the trapped air pocket and the curve C_2 encloses C_1 and is embedded in the fluid. Both curves pass through the intersection point and R is the region between them (shown as the shaded region in figure 4.2. Now consider the circulation around the loop enclosing the region R

$$\Gamma = \int_{C_2} \underline{u}.\underline{dr} - \int_{C_1} \underline{u}.\underline{dr}$$
$$= \int_{C_2 - C_1} \underline{u}.\underline{dr} \tag{4.1}$$

By Stokes theorem

$$\Gamma = \int_R \nabla \times \underline{u}.\underline{ds} \tag{4.2}$$

However the flow is irrotational, hence $\Gamma = 0$

$$\int_{C_2} \underline{u}.\underline{dr} = \int_{C_1} \underline{u}.\underline{dr} \tag{4.3}$$

Hence the circulation around C_2 equals the circulation around C_1, so for simplicity the path integral around the boundary of the air pocket can be used.

The velocities around this loop are not accurately known, but can be estimated. It is known that breaking occurs when the crest velocity is equal to the wave celerity. From numerical simulations of deepwater waves [68] the maximum crest velocity is known to be of the order of $1.5v_p$, while velocities near the base
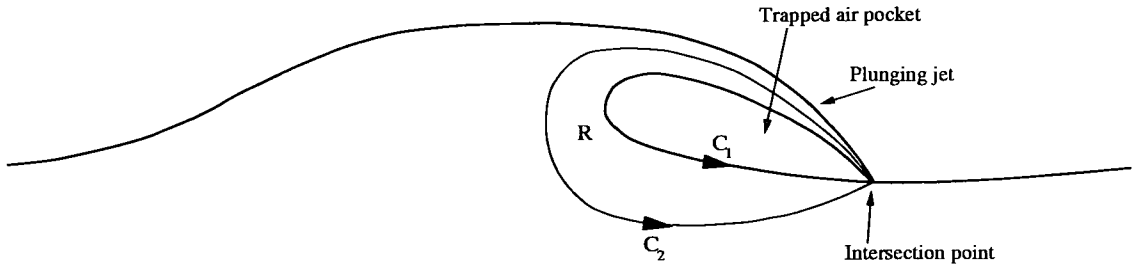
Figure 4.2: Jet tip hitting forward face of wave.

of the loop are almost perpendicular to the ellipse, implying a near-zero velocity component along the direction of the curve.

As an approximation we can say that along the top edge of the loop the velocities are all of the order v_p, while along the lower edge of the loop, all the velocities are of the order of zero. From observations of still frames from the high-speed video record, the circumference of the loop is estimated as a, the wave amplitude. An order of magnitude estimation of the circulation is therefore $av_p/2$.

4.4.2 Circulation calculated after breaking

In order to analyse the circulation from the experimental measurements, the vorticity values presented in the form of vorticity maps must be considered. Looking at the vorticity plots for the plunging breaker at position 2, it can be seen that although the patch can be easily identified there is a significant amount of vorticity that is probably not associated with it. This should not be included in a total circulation value for this patch as these vortices will be either surface vortices or, more likely, edge effects from the vorticity calculation itself. The object is to calculate the total circulation around the patch of turbulence, which is practically done by summing the vorticity values within this area and multiplying by the area occupied by one vector (see chapter 3). The most straightforward method

for doing this is to threshold all the vorticity values within the whole vorticity map. This would not only then eliminate contributions from surface components but also disregard background noise vorticity levels, so eliminating the requirement to physically identify the patch. These levels are between 1 and -1, often being substantially less.

To calculate the circulation in region 2, a threshold of vorticity below $-1s^{-1}$ would suffice, eliminating all positive vorticity which is evident at the surface and all the background noise, giving the strength of vorticity in the region. This is not a highly accurate method because it assumes that all important vorticity is negative and below $-1s^{-1}$ in value. It does however give an insight into how the vorticity diffuses to lower levels and how the vortex strengths are changing.

Figure 4.3 shows the change in circulation calculated using this method over the 4.5s data collection time, averaged for all repeats at position 2. If the relationship is taken as being a straight line (it probably will not be but due to this being early stages of the flow, the true relation will be masked) and extrapolate back to T=0s then an estimate for the maximum circulation around this main vortical patch can be made.

4.4.3 Conclusion from comparison

The value gained from extrapolating the graph in figure 4.3 was $0.04456m^2s^{-1}$ and the value of $av_p/2$ is $0.14006m^2s^{-1}$ which implies that the circulation around this patch is approximately 32% of the estimated value for the maximum circulation.

This calculation probably gives a lower bound to the fraction of circulation that is distributed within the region directly below the overturning crest. In reality, both the circumference of the trapped air pocket and the velocities around the curve, are likely to be smaller than the values used here. The value obtained
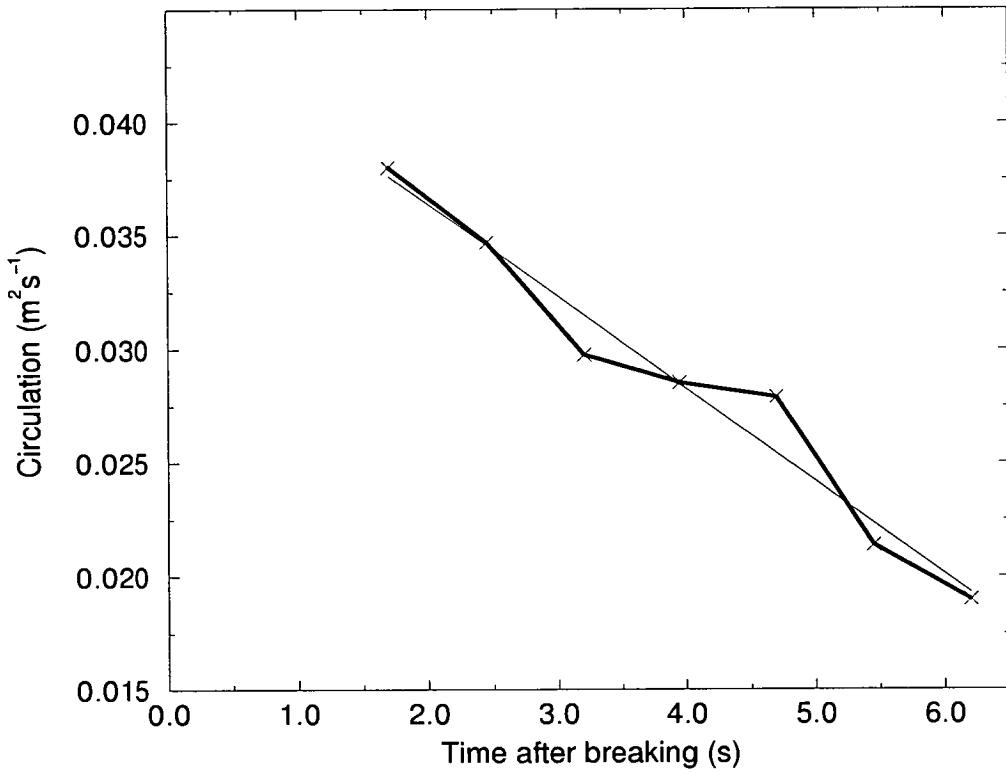
Figure 4.3: Variation of circulation within region 2 with time.

is of the correct magnitude to suggest that conservation of circulation in the way described here, is quite likely.

This is only an order of magnitude comparison and to make any definite conclusions a more accurate estimation of the circulation at the instant that the crest hits the previously undisturbed water, needs to be made. This could be accurately calculated with a numerical simulation up to the point of breaking using exactly the same input wave parameters used in the experiment [14] [23].
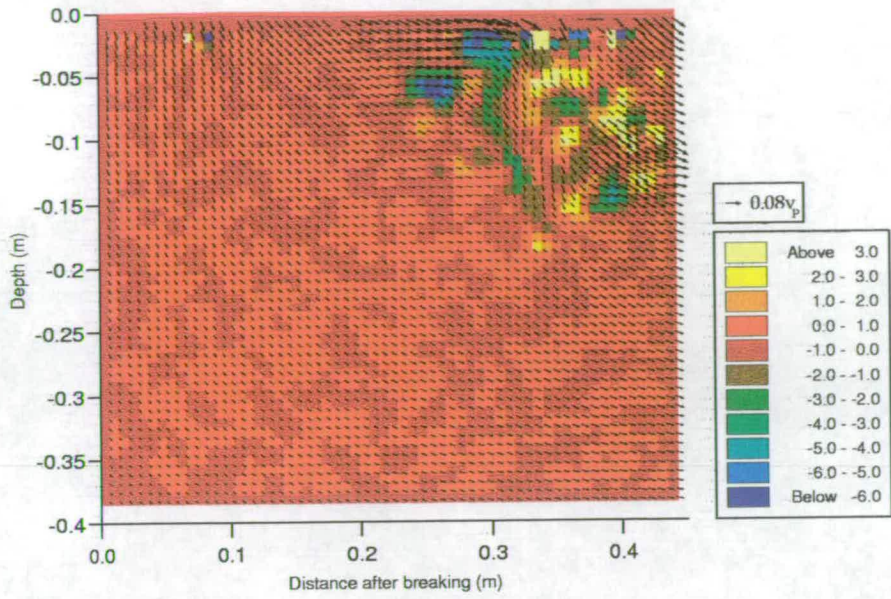
Figure 4.4: Vorticity levels (s^{-1}) for plunging breaker at position 1, T=1.70s
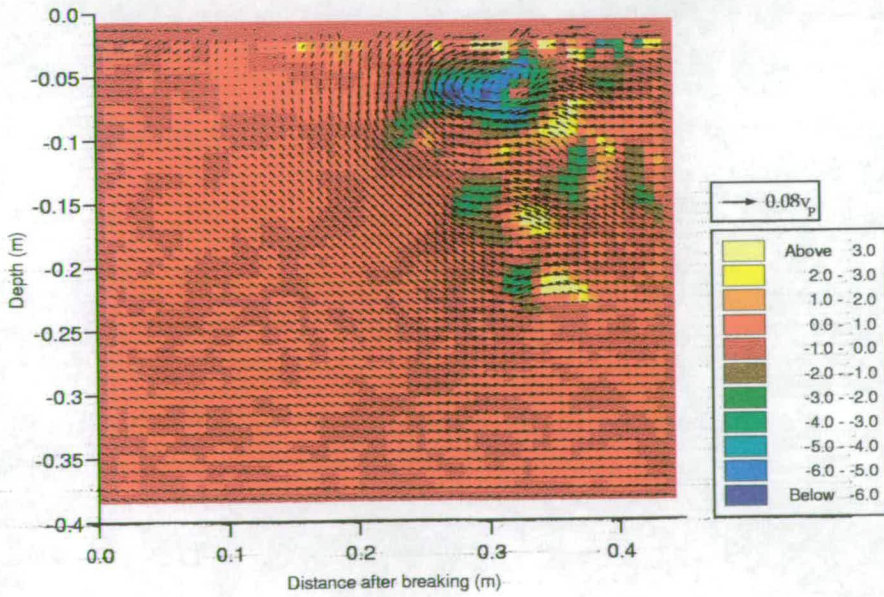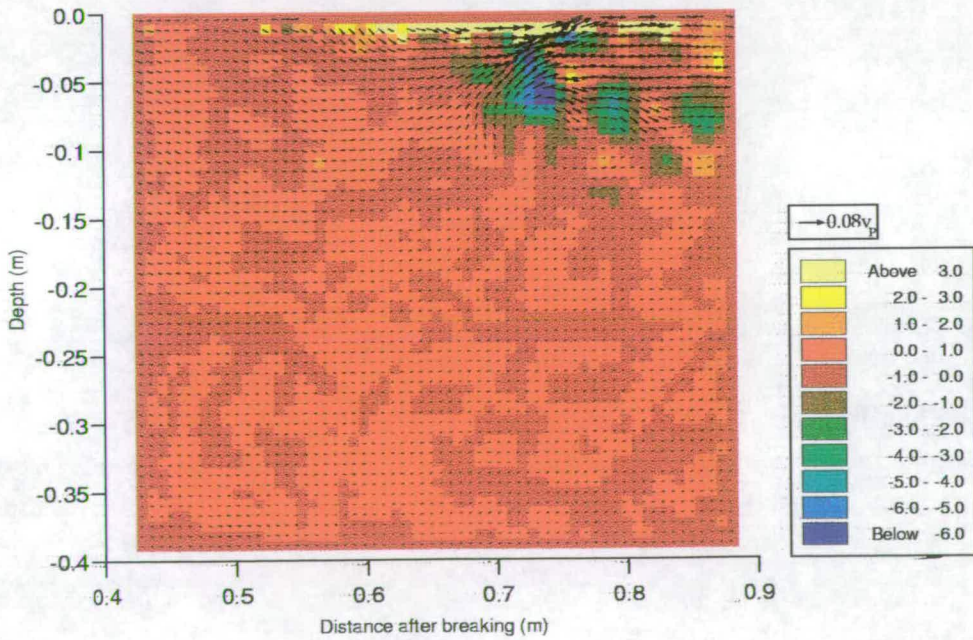

Figure 4.5: Vorticity levels (s^{-1}) for plunging breaker at position 1, T=2.45s
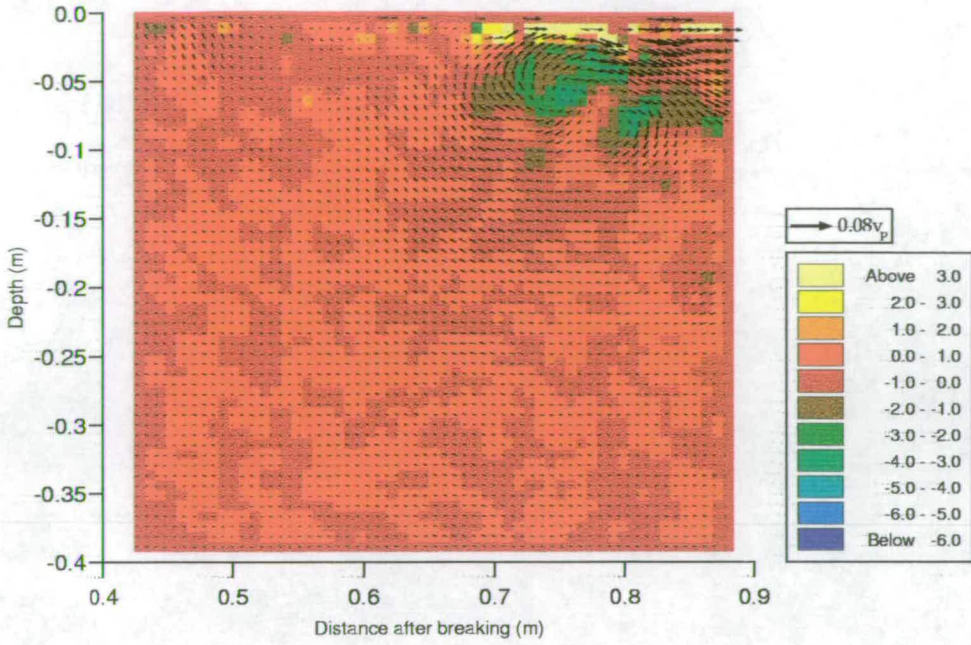
57
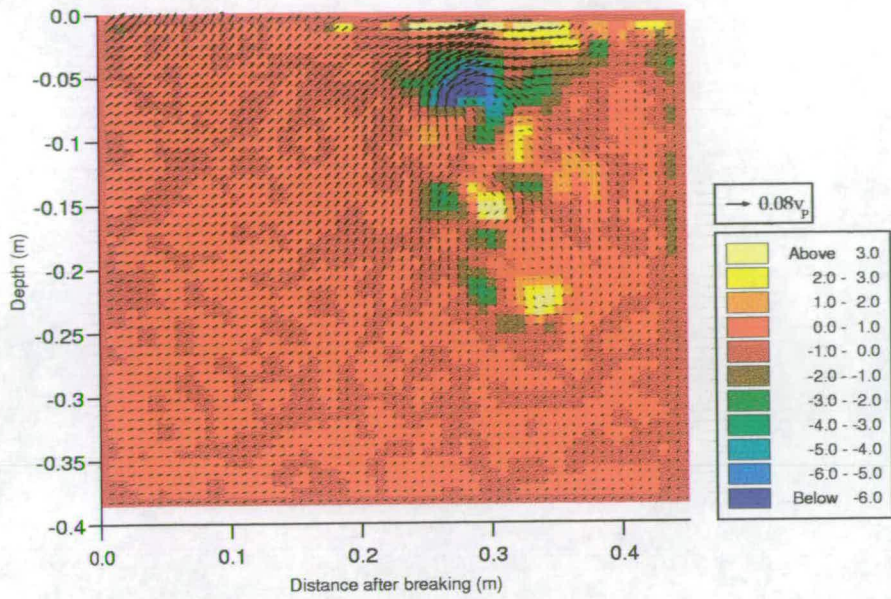
Figure 4.6: Vorticity levels (s^{-1}) for plunging breaker at position 1, T=3.20s
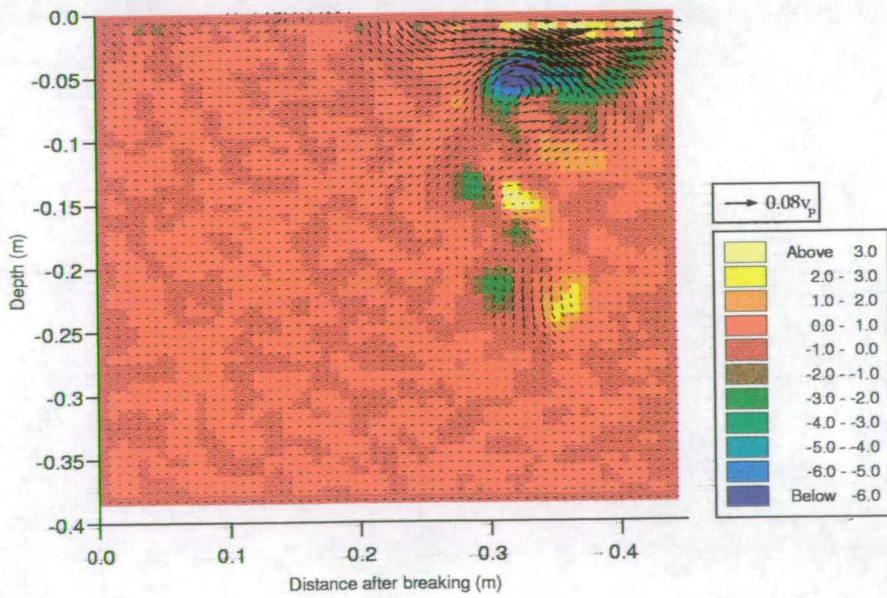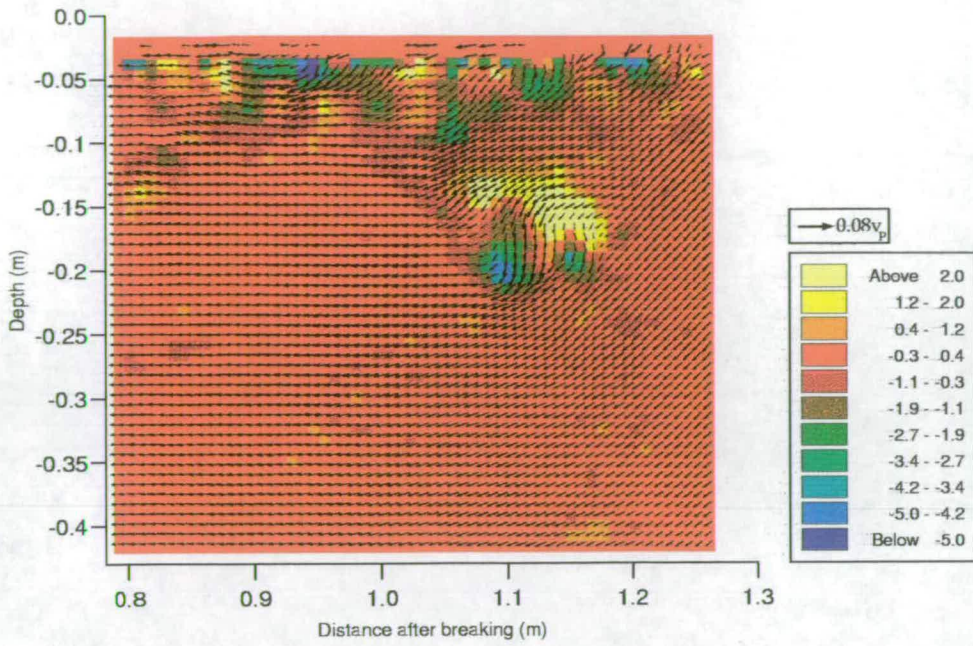

Figure 4.7: Vorticity levels (s^{-1}) for plunging breaker at position 1, T=3.95s
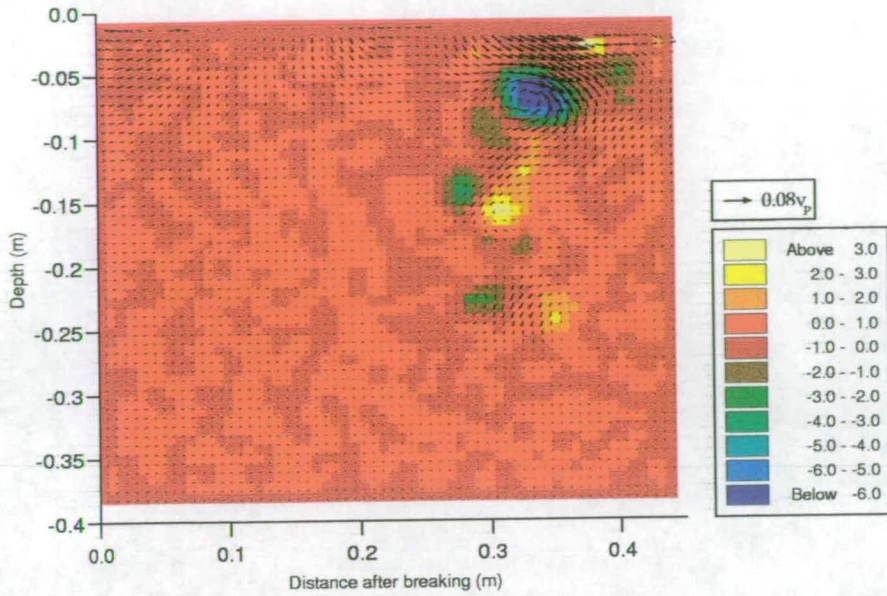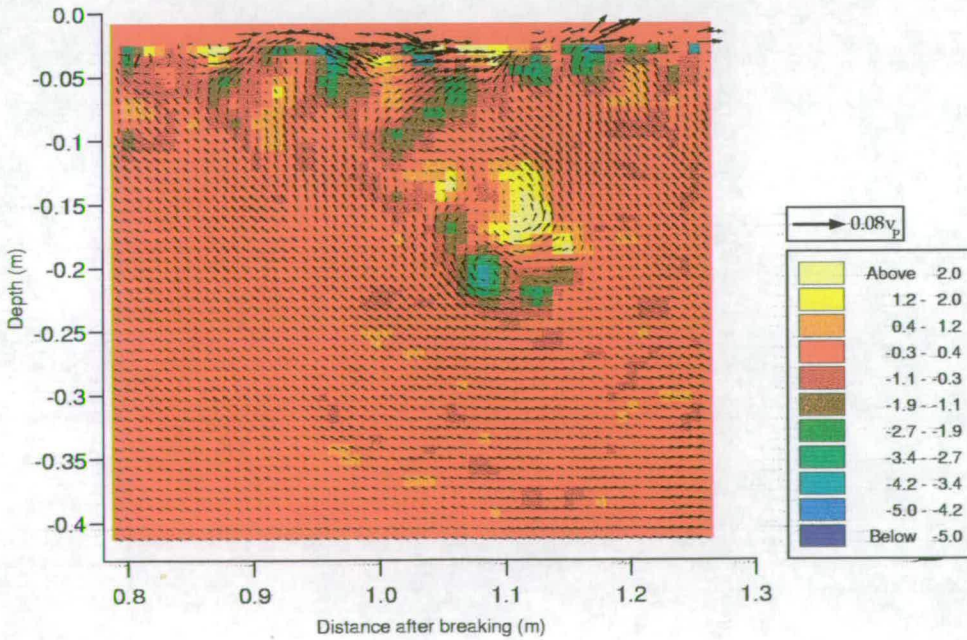
Figure 4.8: Vorticity levels (s^{-1}) for plunging breaker at position 1, T=4.70s
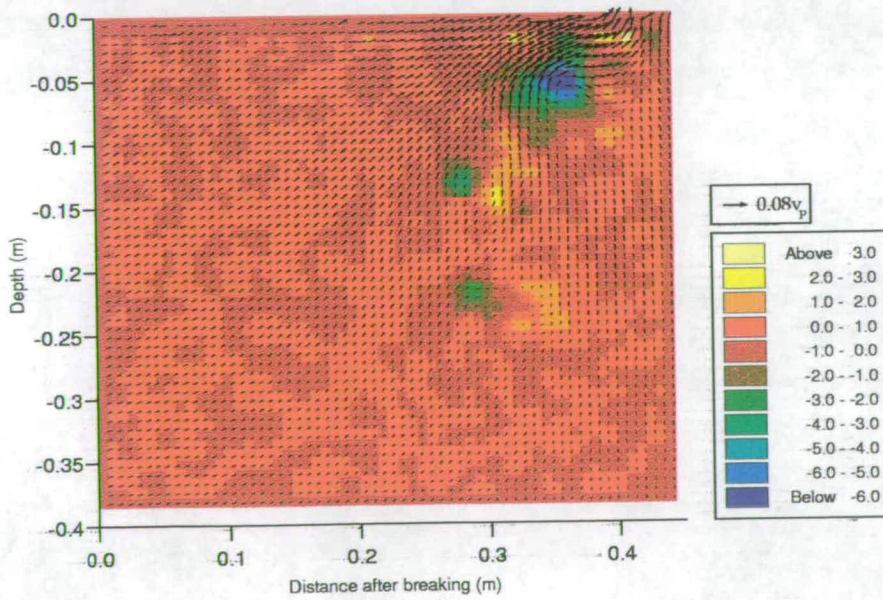
Figure 4.9: Vorticity levels (s^{-1}) for plunging breaker at position 1, T=5.45s
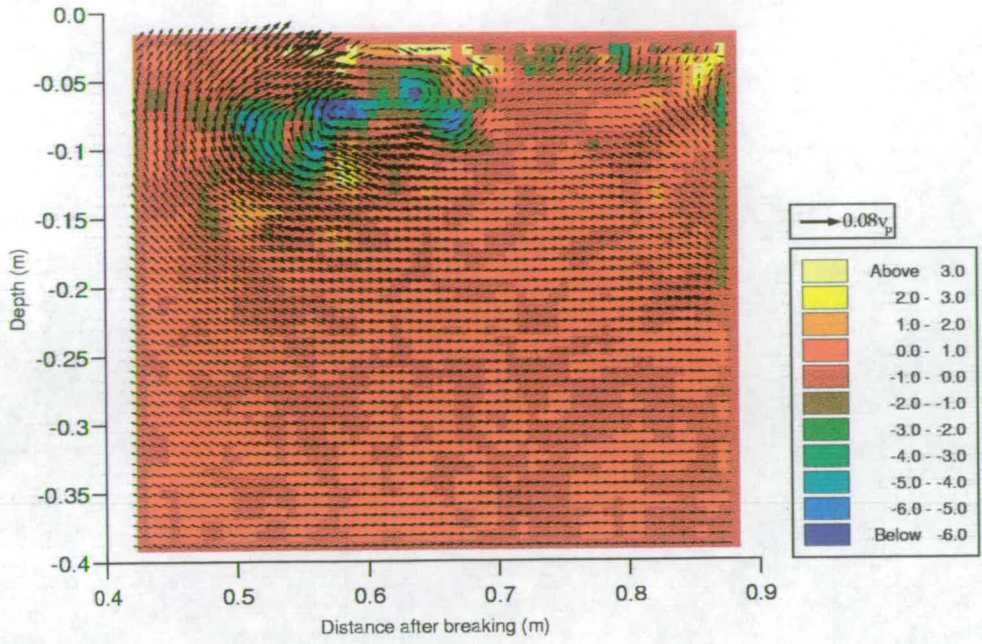
Figure 4.10: Vorticity levels (s^{-1}) for plunging breaker at position 2, T=1.7s
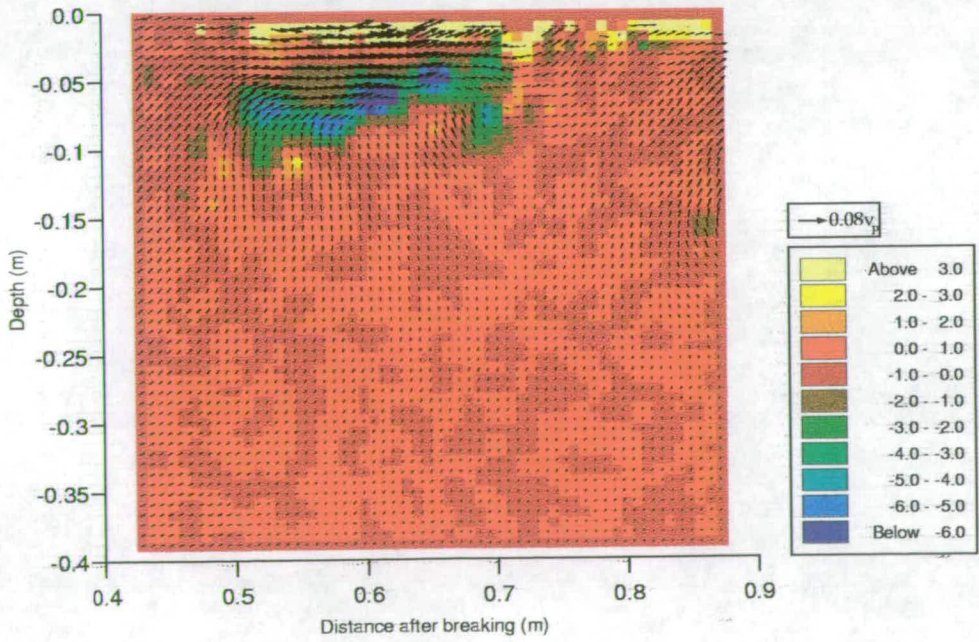
Figure 4.11: Vorticity levels (s^{-1}) for plunging breaker at position 2, T=2.45s
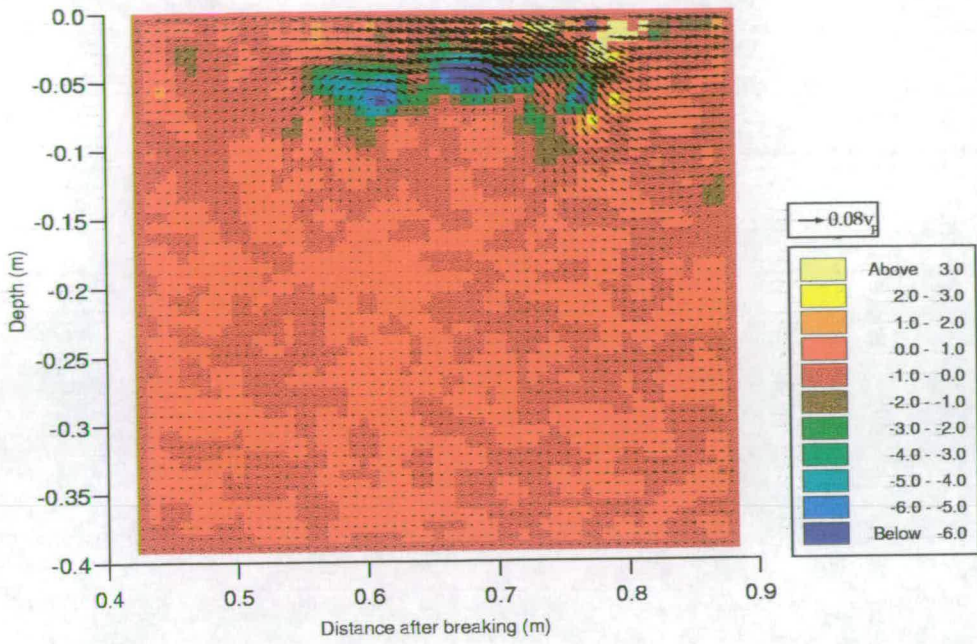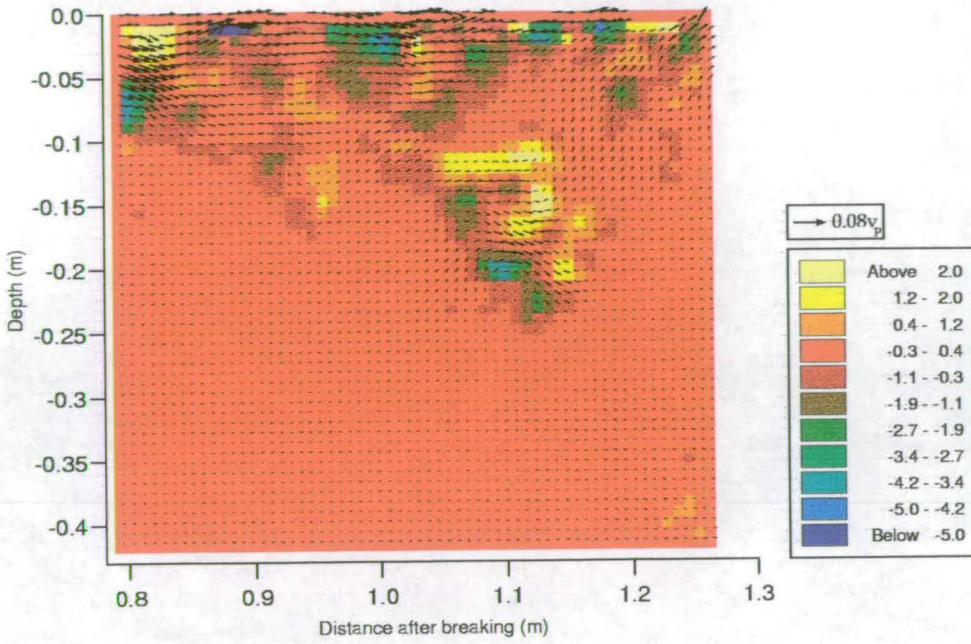
Figure 4.12: Vorticity levels (s^{-1}) for plunging breaker at position 2, T=3.20s
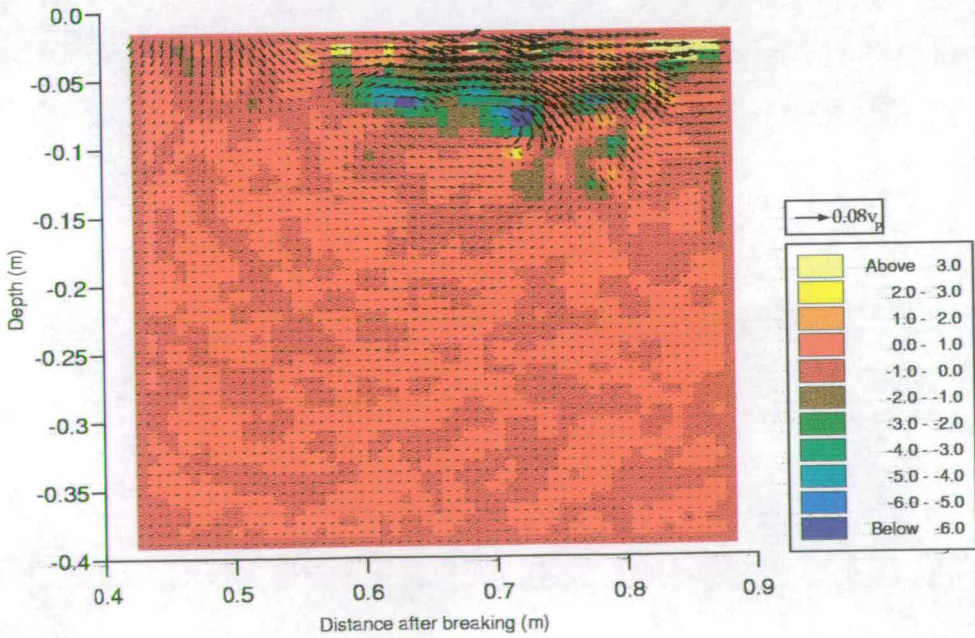
Figure 4.13: Vorticity levels (s^{-1}) for plunging breaker at position 2, T=3.95s

61
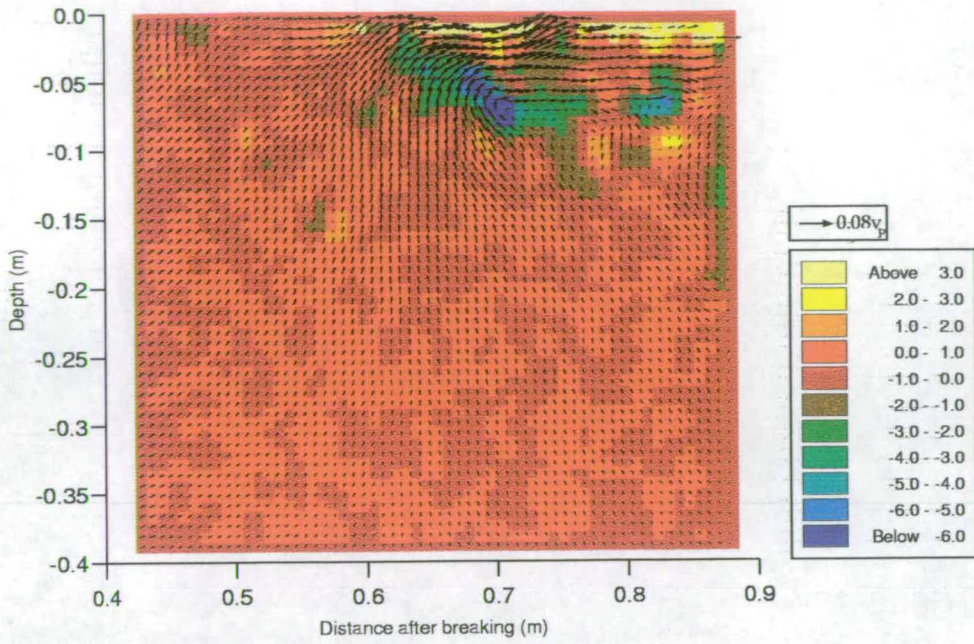
Figure 4.14: Vorticity levels (s^{-1}) for plunging breaker at position 2, T=4.70s

Figure 4.15: Vorticity levels (s^{-1}) for plunging breaker at position 2, T=5.45s

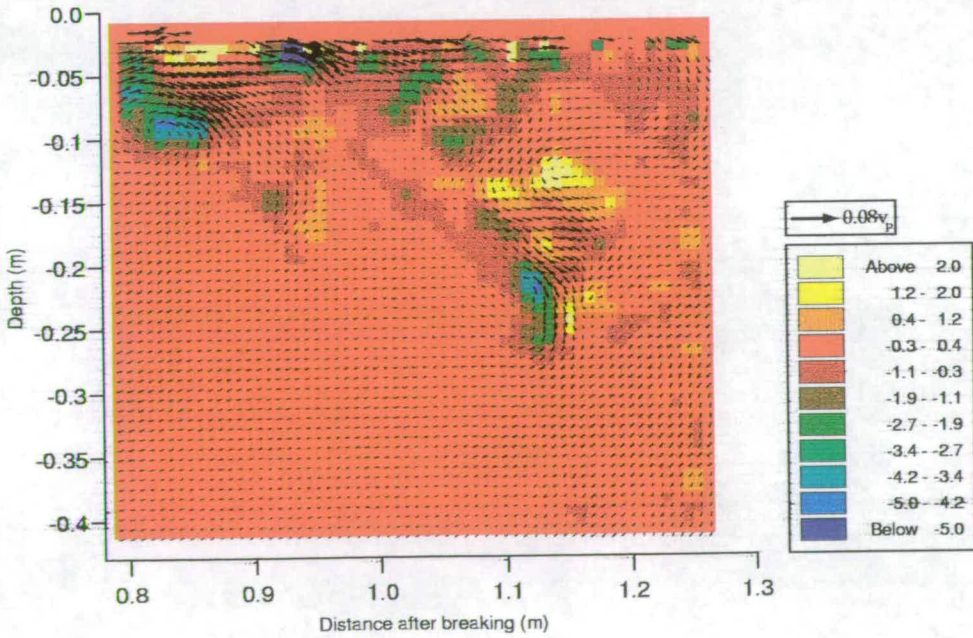**Figure 4.16:** Vorticity levels (s^{-1}) for plunging breaker at position 2, T=6.20s

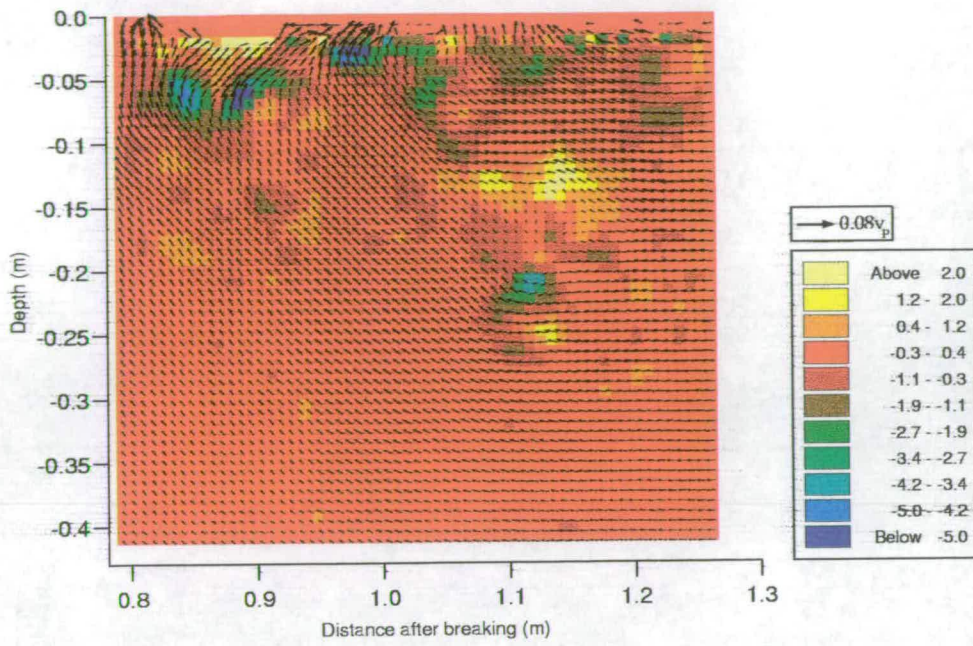**Figure 4.17:** Vorticity levels (s^{-1}) for plunging breaker at position 3, T=1.70s

Figure 4.18: Vorticity levels (s^{-1}) for plunging breaker at position 3, T=2.45s

Figure 4.19: Vorticity levels (s^{-1}) for plunging breaker at position 3, T=3.20s

Figure 4.20: Vorticity levels (s^{-1}) for plunging breaker at position 3, T=3.95s

Figure 4.21: Vorticity levels (s^{-1}) for plunging breaker at position 3, T=4.70s
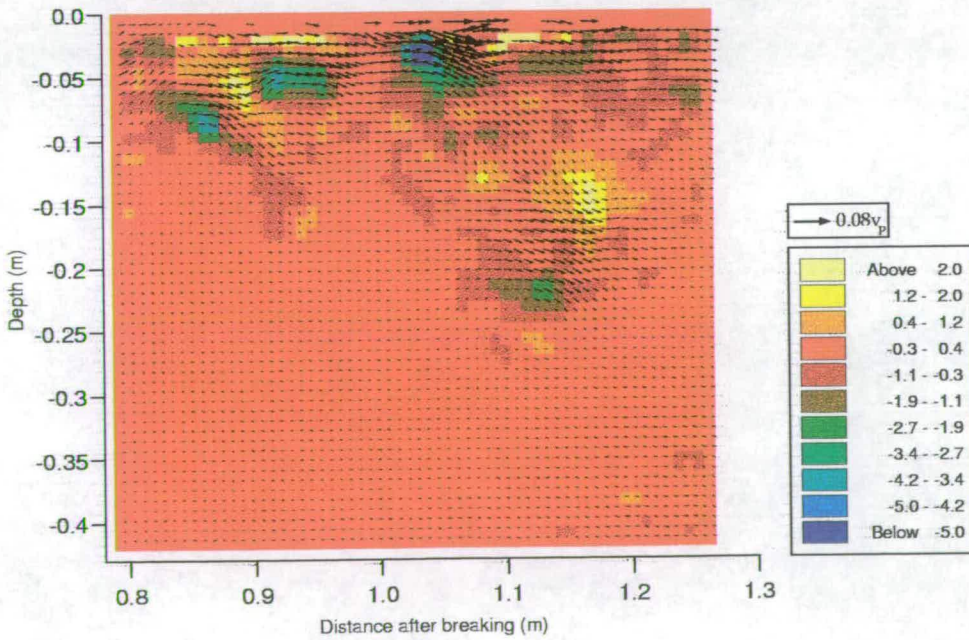

Figure 4.22: Vorticity levels (s^{-1}) for plunging breaker at position 3, T=5.45s
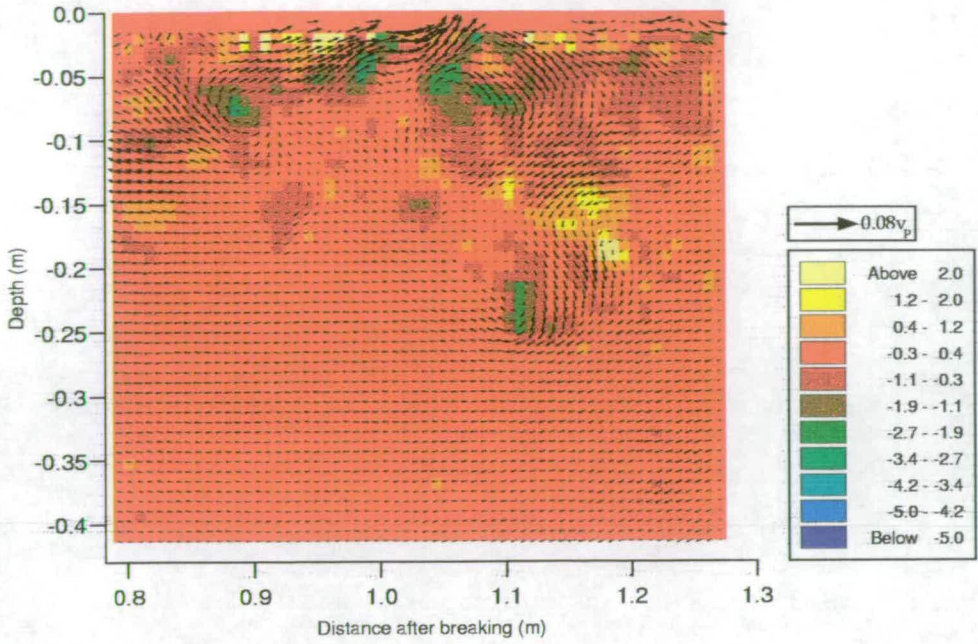
Figure 4.23: Vorticity levels (s^{-1}) for plunging breaker at position 3, T=6.20s
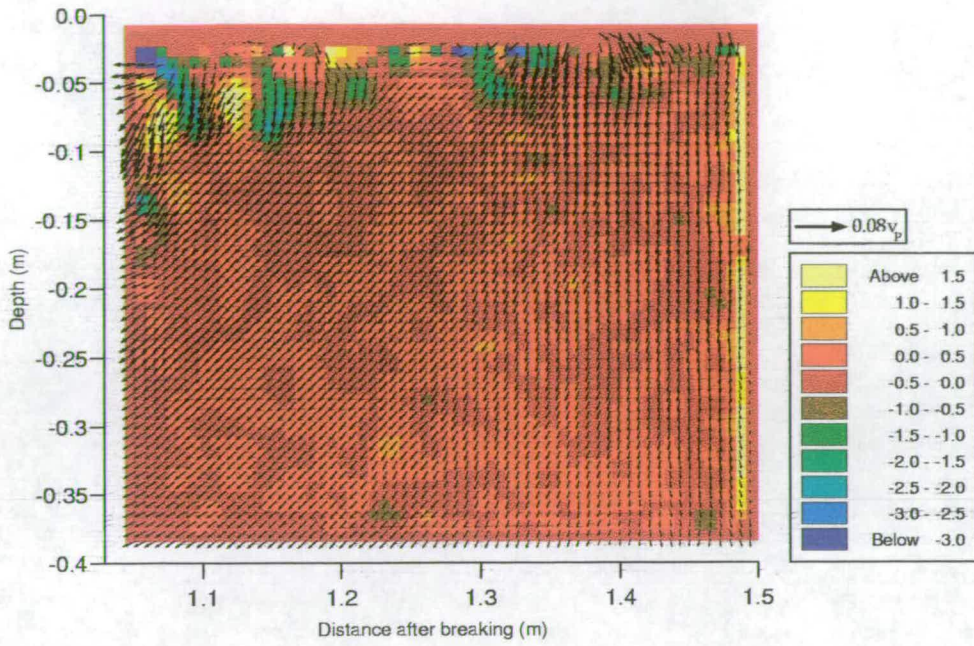
Figure 4.24: Vorticity levels (s^{-1}) for plunging breaker at position 4, T=1.70s
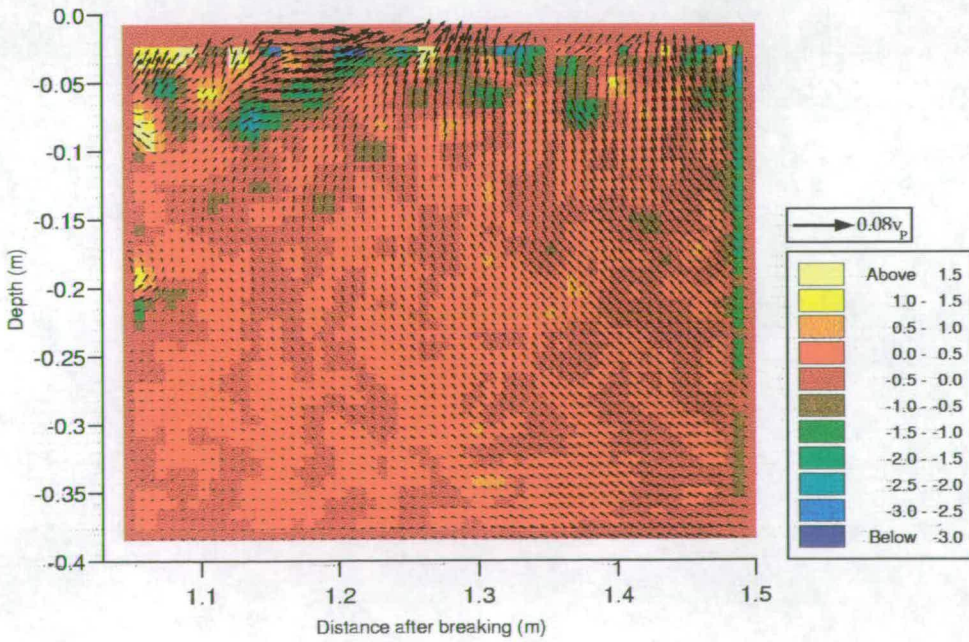

Figure 4.25: Vorticity levels (s^{-1}) for plunging breaker at position 4, T=2.45s

Figure 4.26: Vorticity levels (s^{-1}) for plunging breaker at position 4, T=3.20s

Figure 4.27: Vorticity levels (s^{-1}) for plunging breaker at position 4, T=3.95s

Figure 4.28: Vorticity levels (s^{-1}) for plunging breaker at position 4, T=4.70s

Figure 4.29: Vorticity levels (s^{-1}) for plunging breaker at position 4, T=5.45s
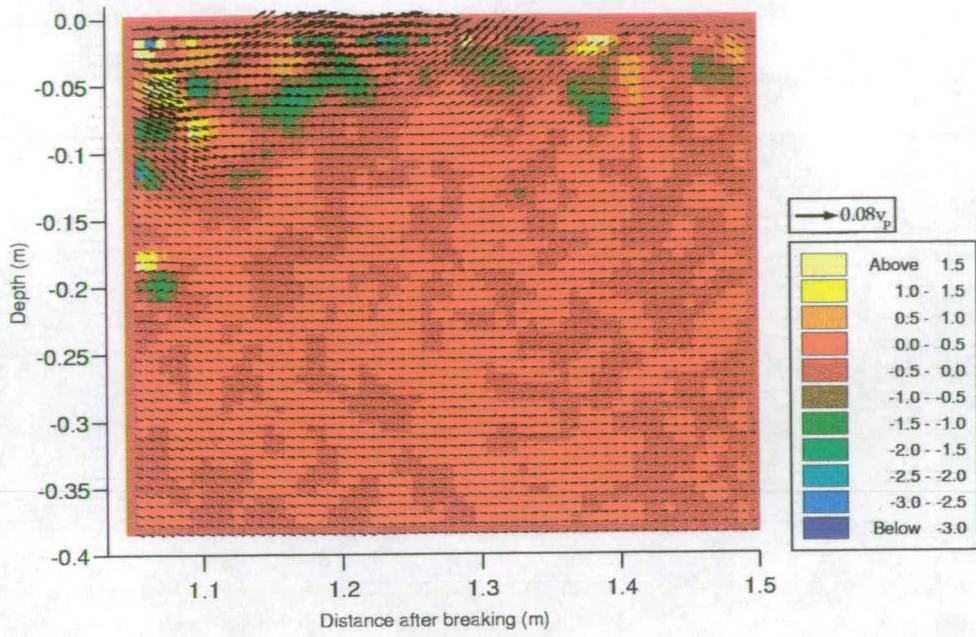
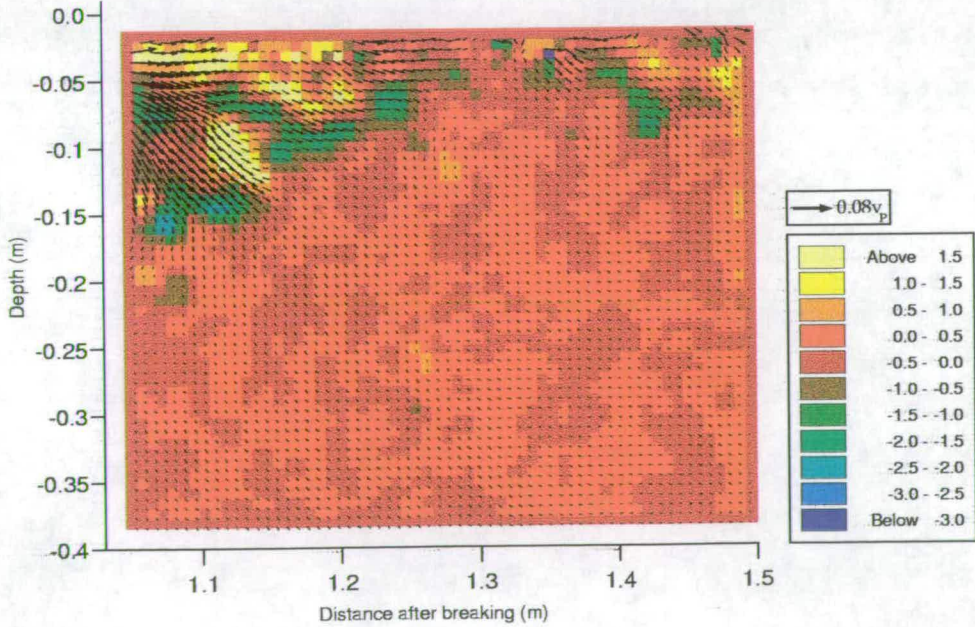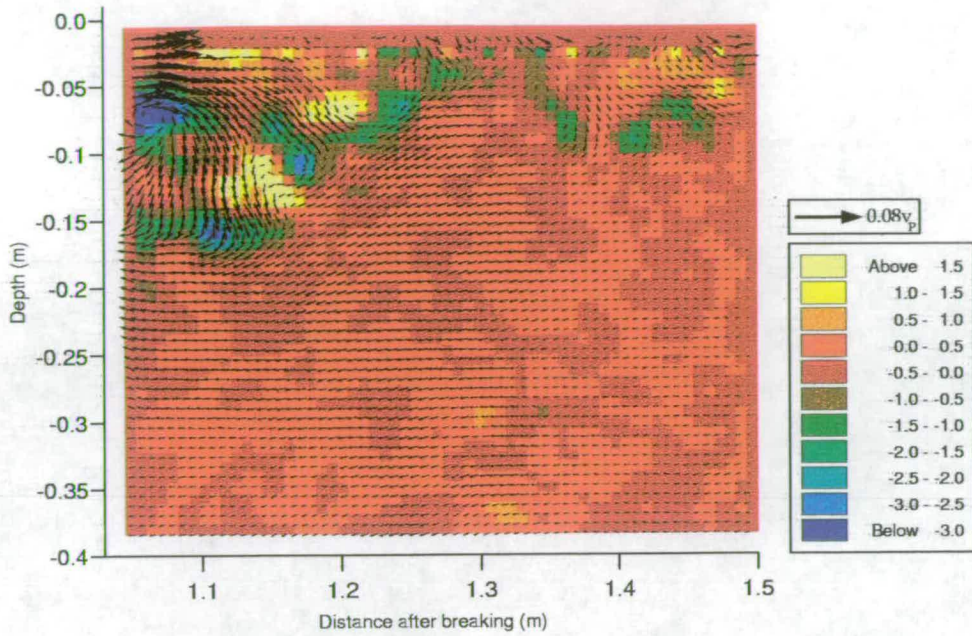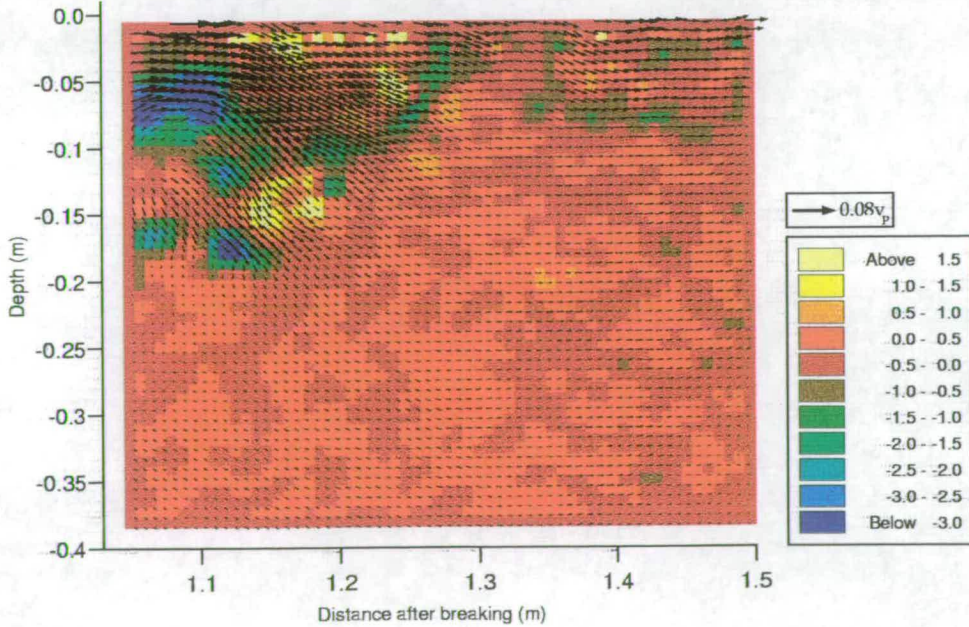**Figure 4.30:** Vorticity levels (s^{-1}) for plunging breaker at position 4, T=6.20s

Figure 4.31: Vorticity levels (s^{-1}) for spilling breaker at position 1, T=1.70s

Figure 4.32: Vorticity levels (s^{-1}) for spilling breaker at position 1, T=2.45s

Figure 4.33: Vorticity levels (s^{-1}) for spilling breaker at position 1, T=3.20s

Figure 4.34: Vorticity levels (s^{-1}) for spilling breaker at position 1, T=3.95s

Figure 4.35: Vorticity levels (s^{-1}) for spilling breaker at position 1, T=4.70s

Figure 4.36: Vorticity levels (s^{-1}) for spilling breaker at position 1, T=5.45s

Figure 4.37: Vorticity levels (s^{-1}) for spilling breaker at position 2, T=1.7s
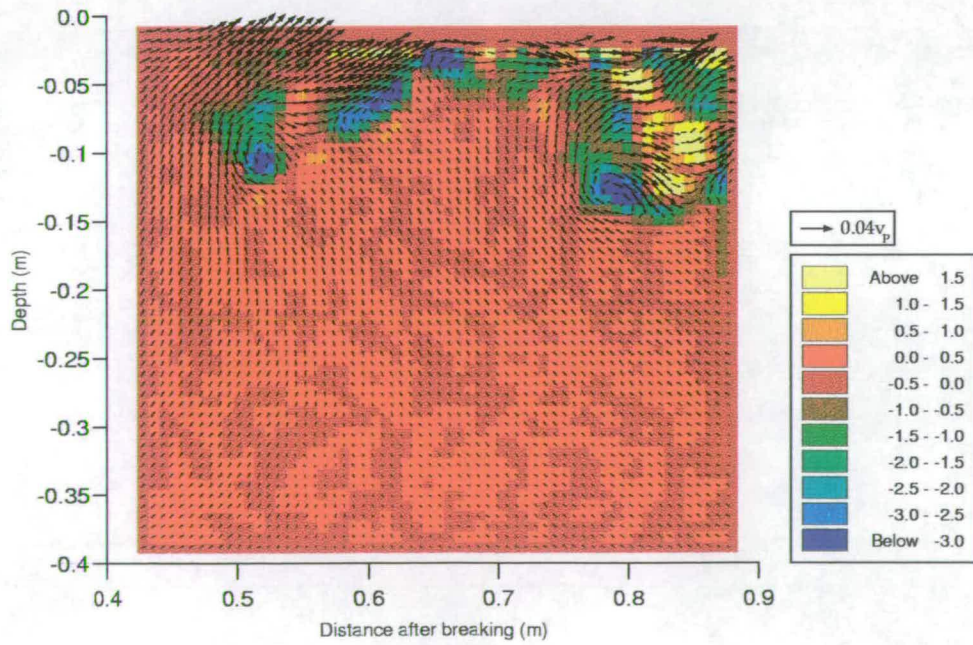
Figure 4.38: Vorticity levels (s^{-1}) for spilling breaker at position 2, T=2.45s
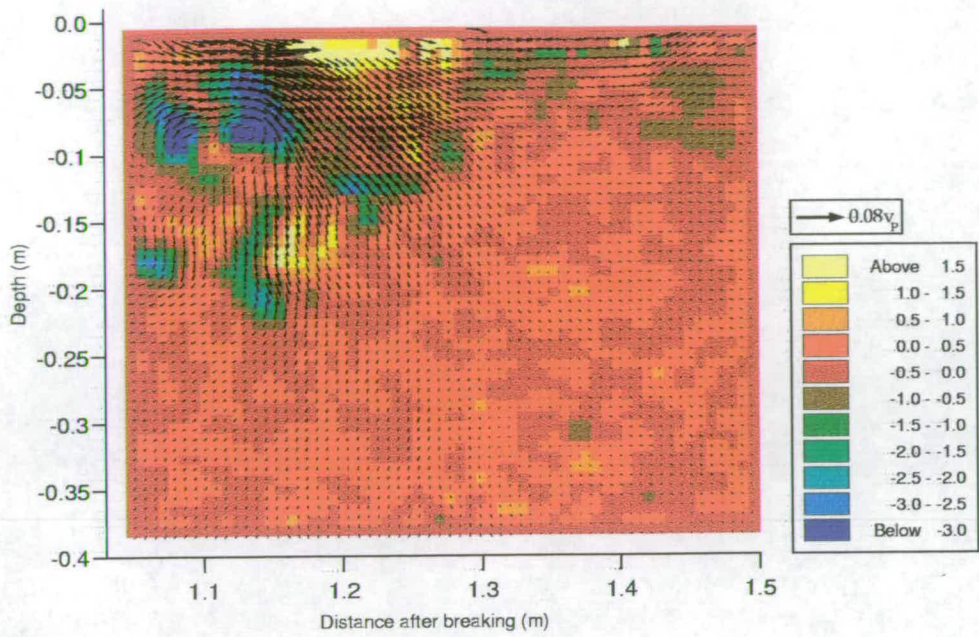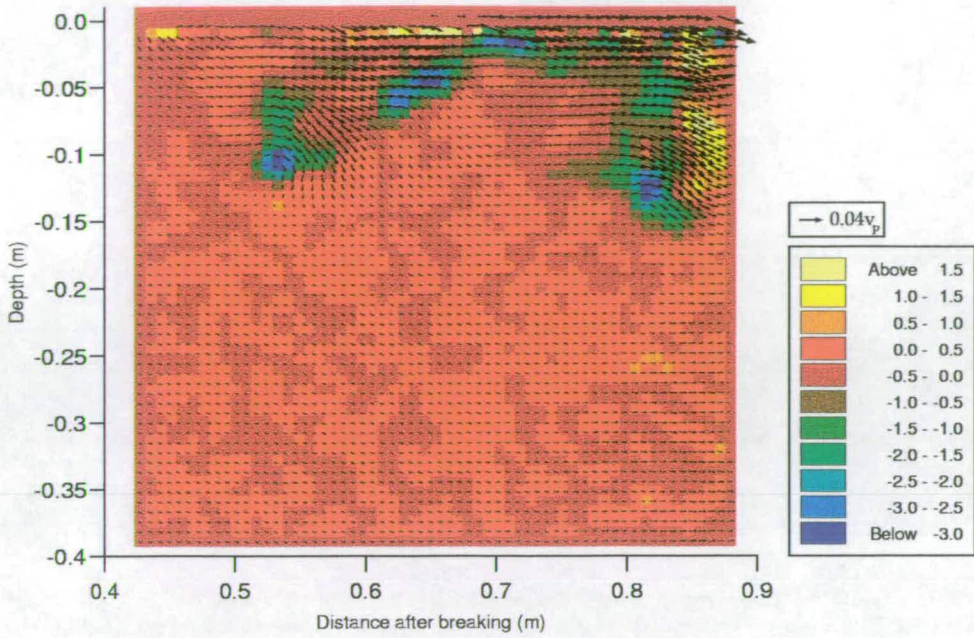
Figure 4.39: Vorticity levels (s^{-1}) for spilling breaker at position 2, T=3.20s
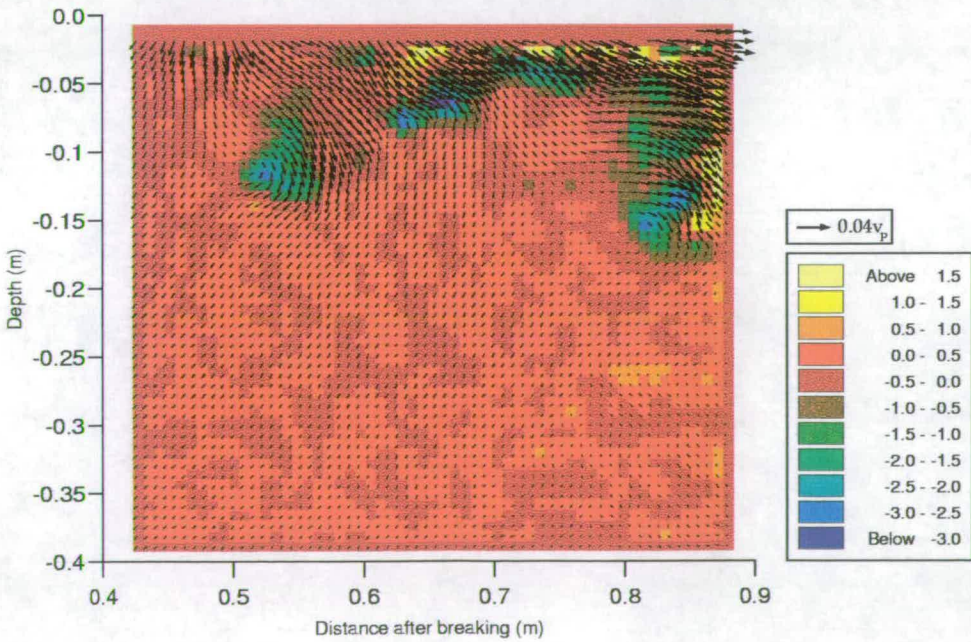
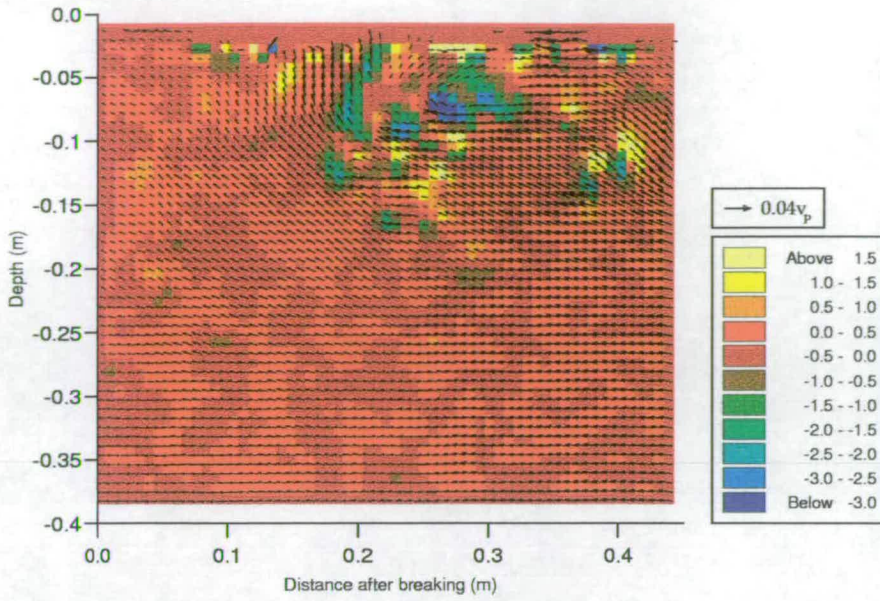**Figure 4.40:** Vorticity levels (s^{-1}) for spilling breaker at position 2, T=3.95s
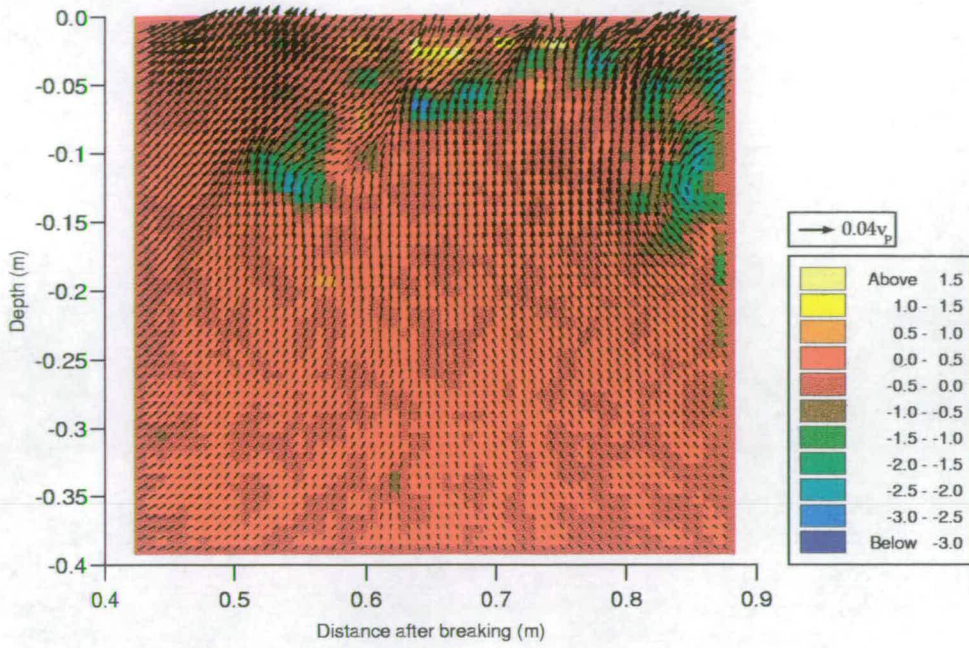
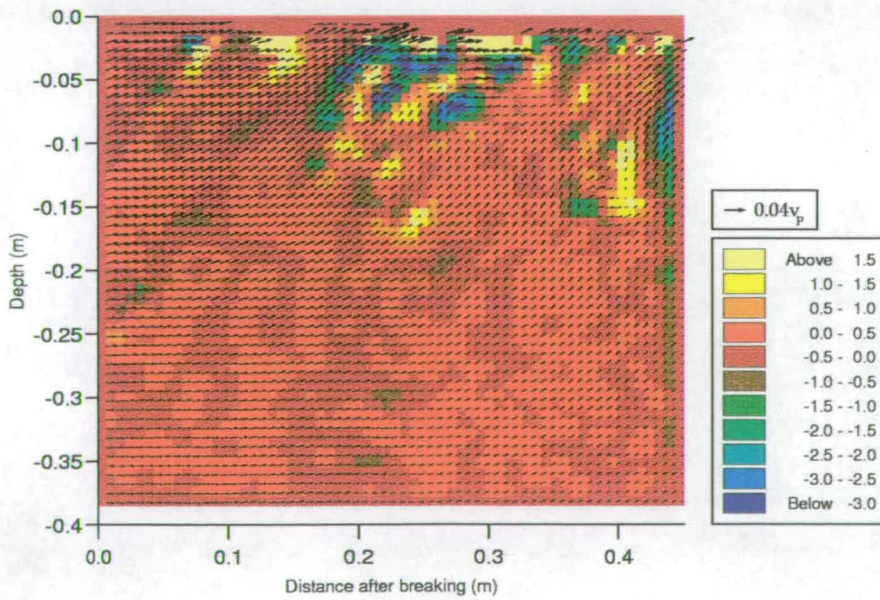**Figure 4.41:** Vorticity levels (s^{-1}) for spilling breaker at position 2, T=4.70s
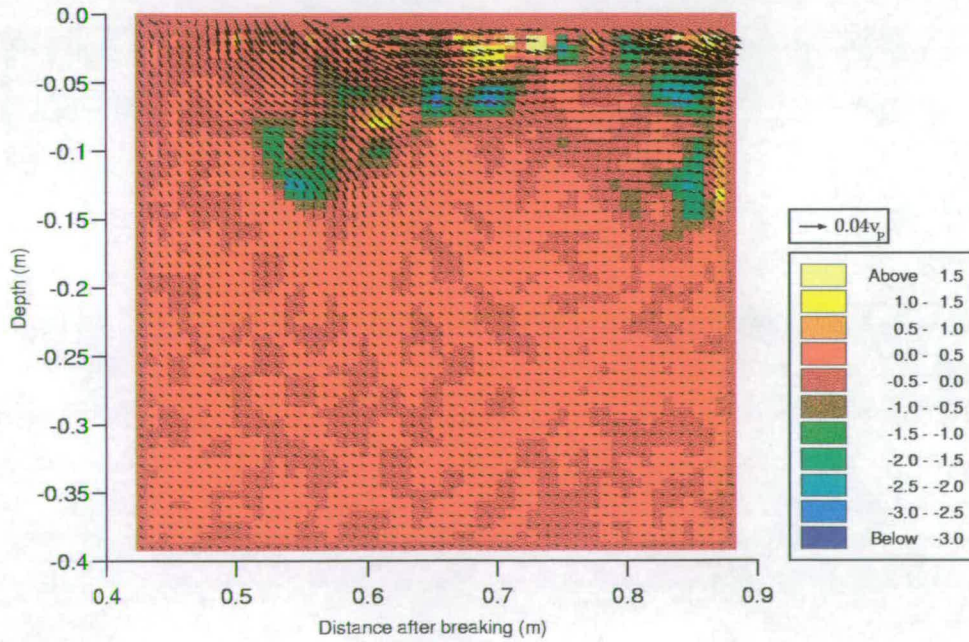
Figure 4.42: Vorticity levels (s^{-1}) for spilling breaker at position 2, T=5.45s
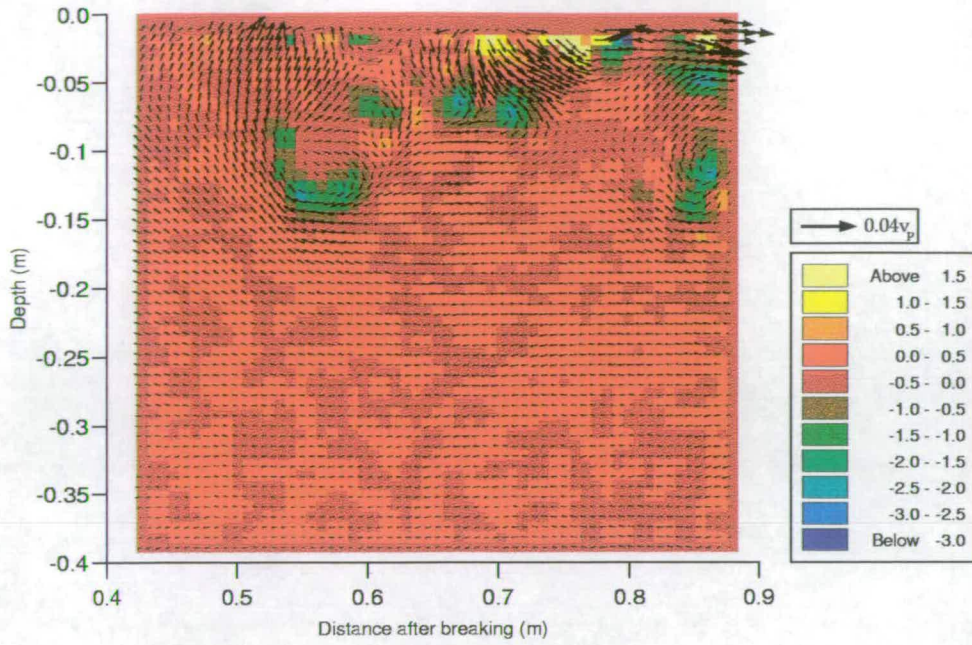
Figure 4.43: Vorticity levels (s^{-1}) for spilling breaker at position 2, T=6.20s
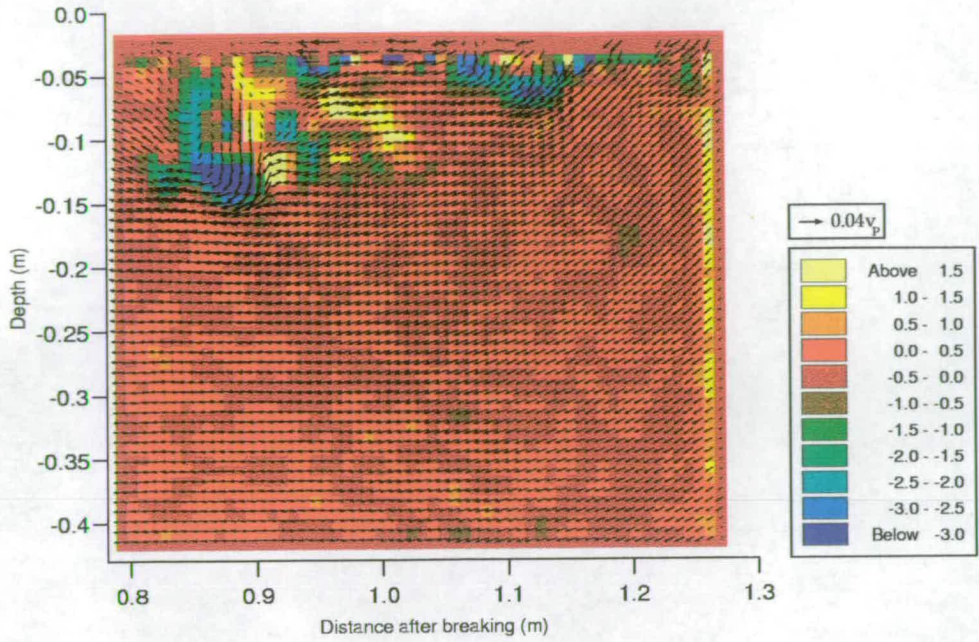
Figure 4.44: Vorticity levels (s^{-1}) for spilling breaker at position 3, T=1.70s
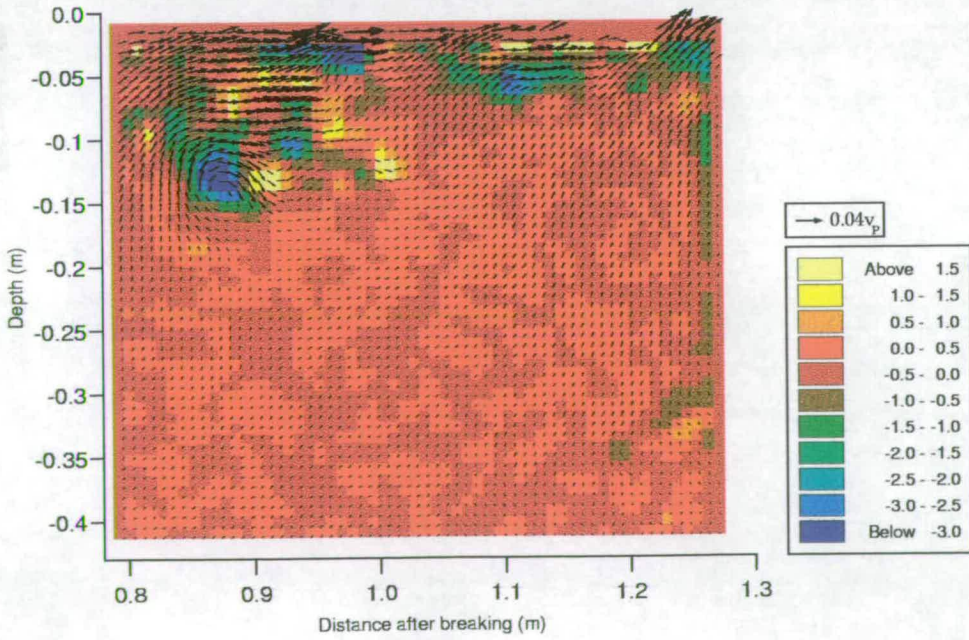
Figure 4.45: Vorticity levels (s^{-1}) for spilling breaker at position 3, T=2.45s
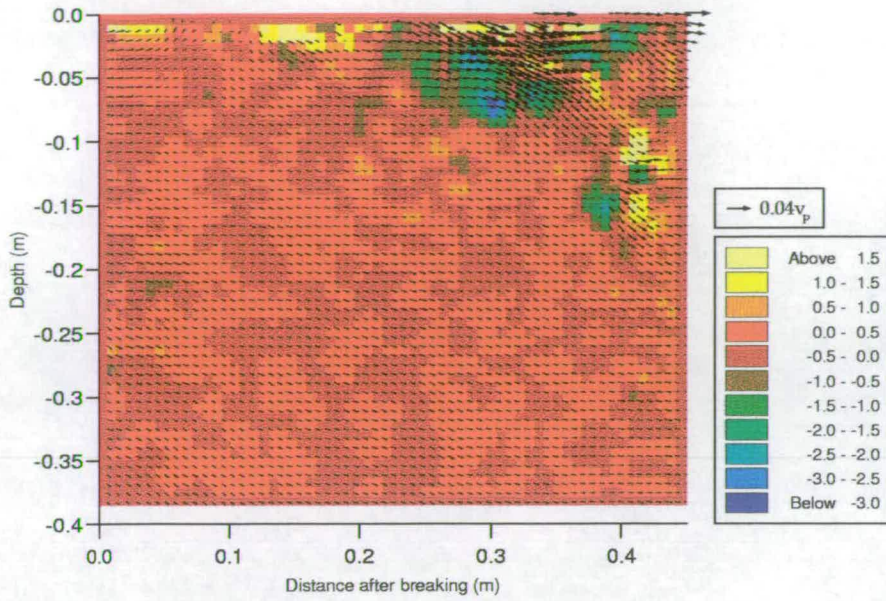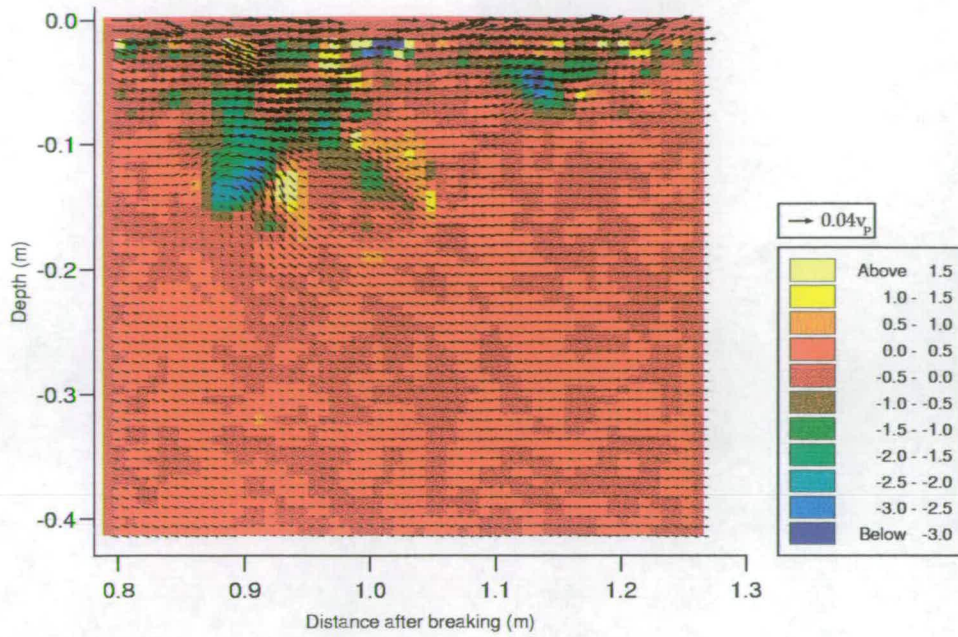
Figure 4.46: Vorticity levels (s^{-1}) for spilling breaker at position 3, T=3.20s
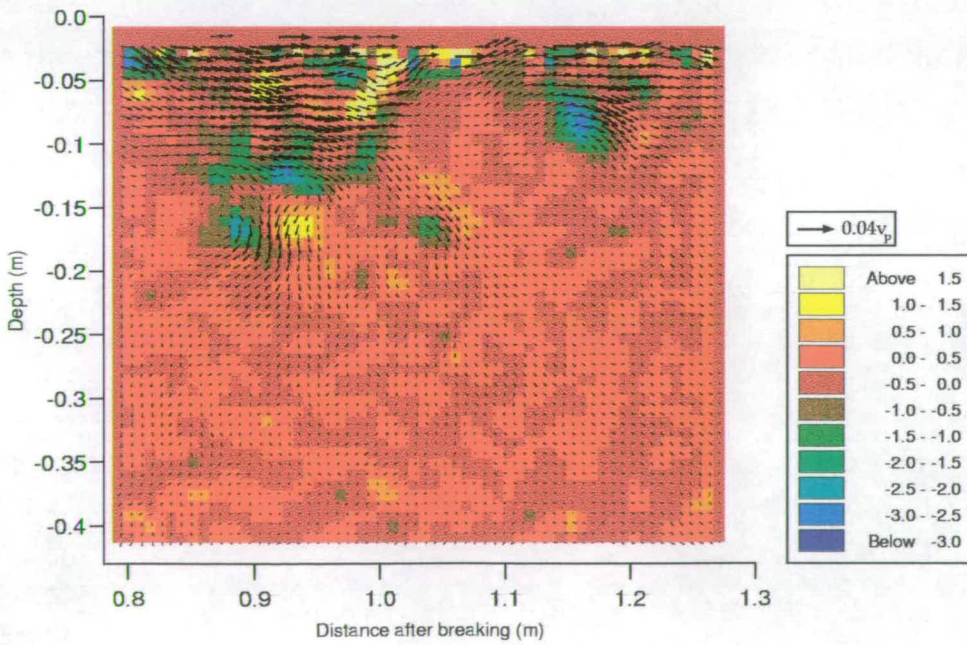
Figure 4.47: Vorticity levels (s^{-1}) for spilling breaker at position 3, T=3.95s
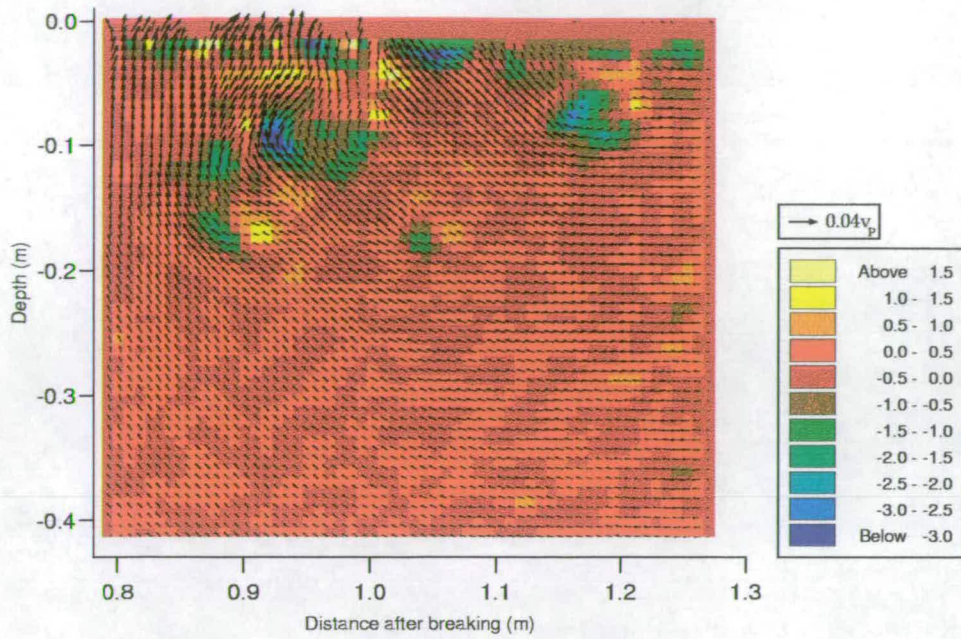
Figure 4.48: Vorticity levels (s^{-1}) for spilling breaker at position 3, T=4.70s
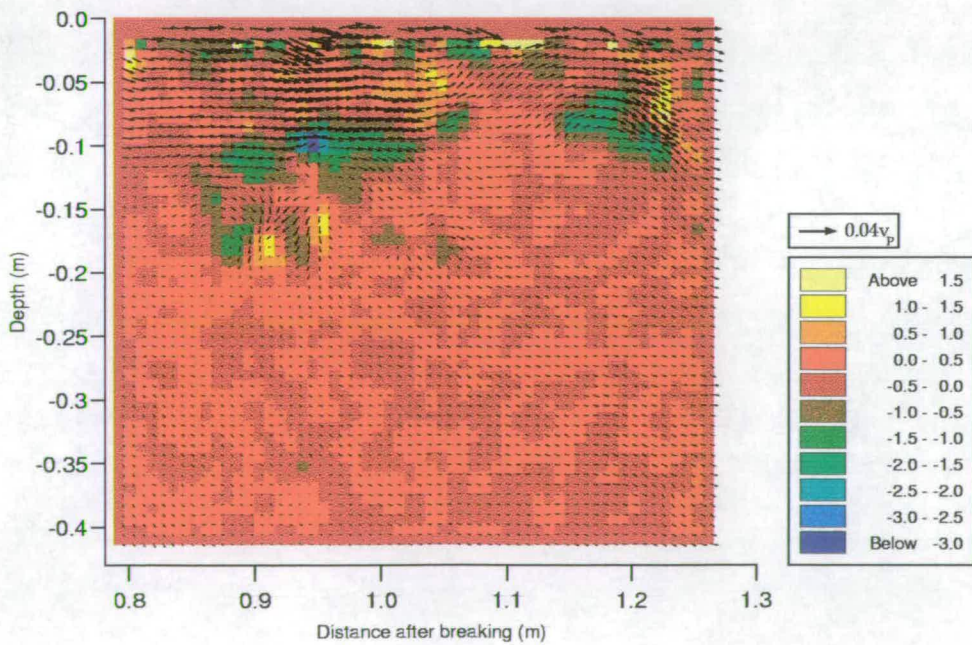
Figure 4.49: Vorticity levels (s^{-1}) for spilling breaker at position 3, T=5.45s
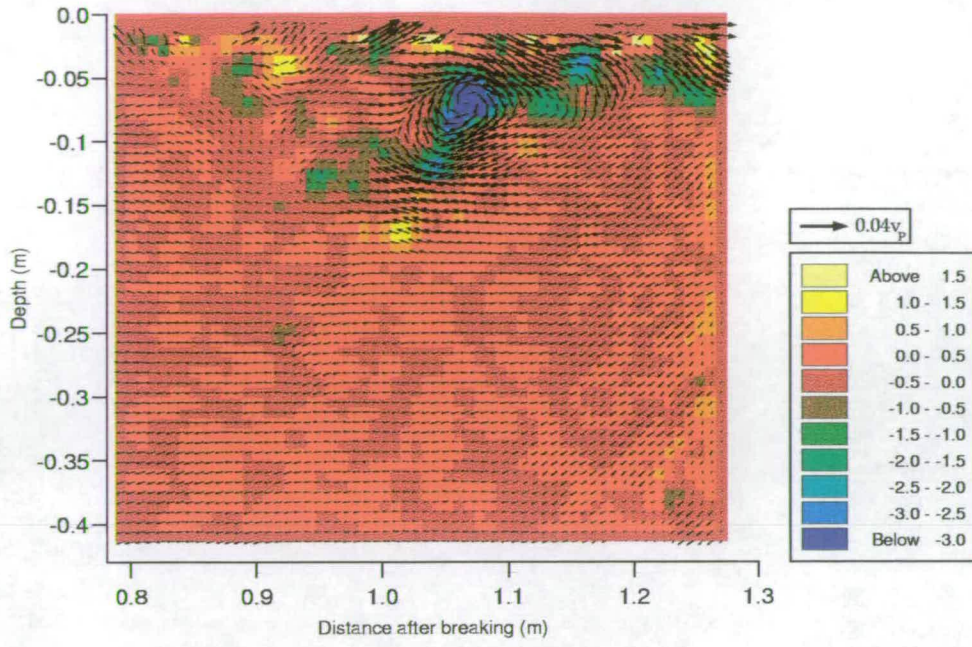
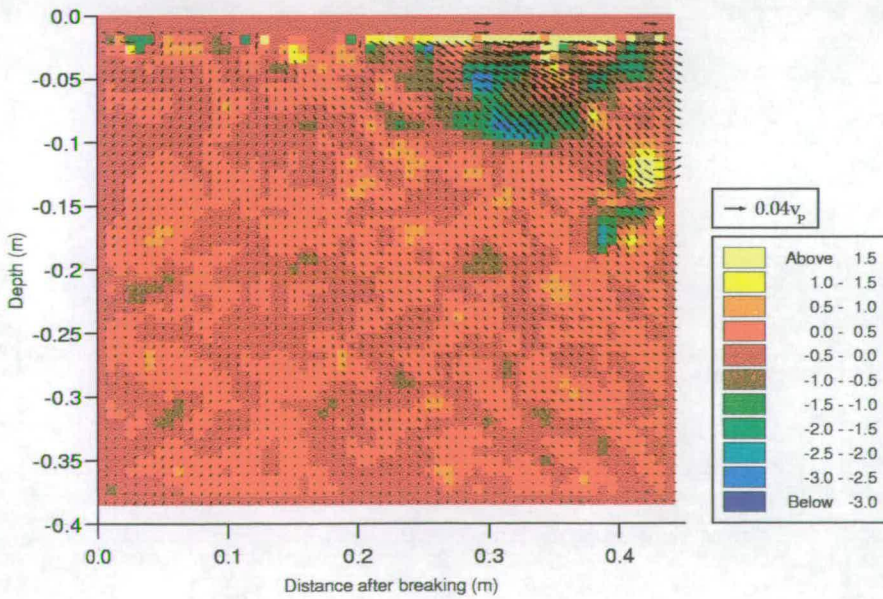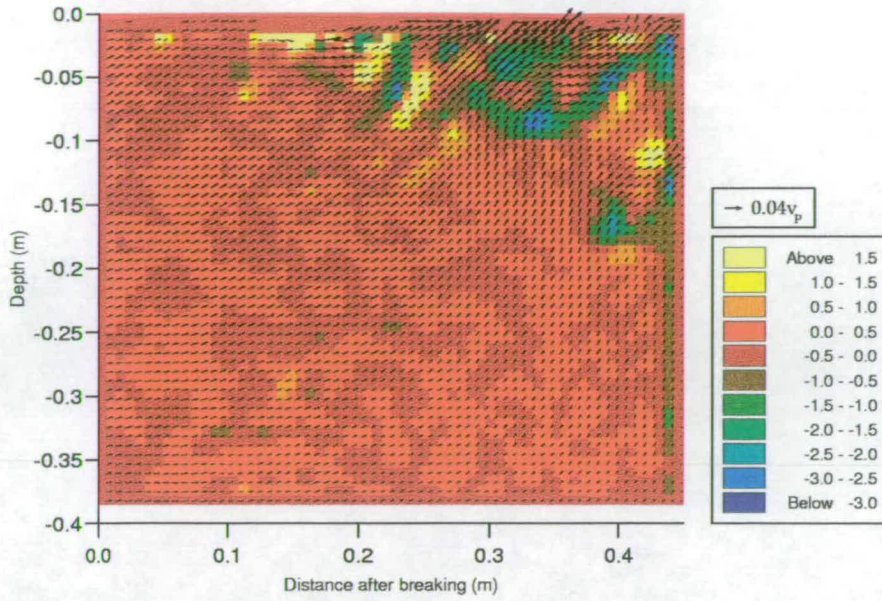**Figure 4.50:** Vorticity levels (s^{-1}) for spilling breaker at position 3, T=6.20s
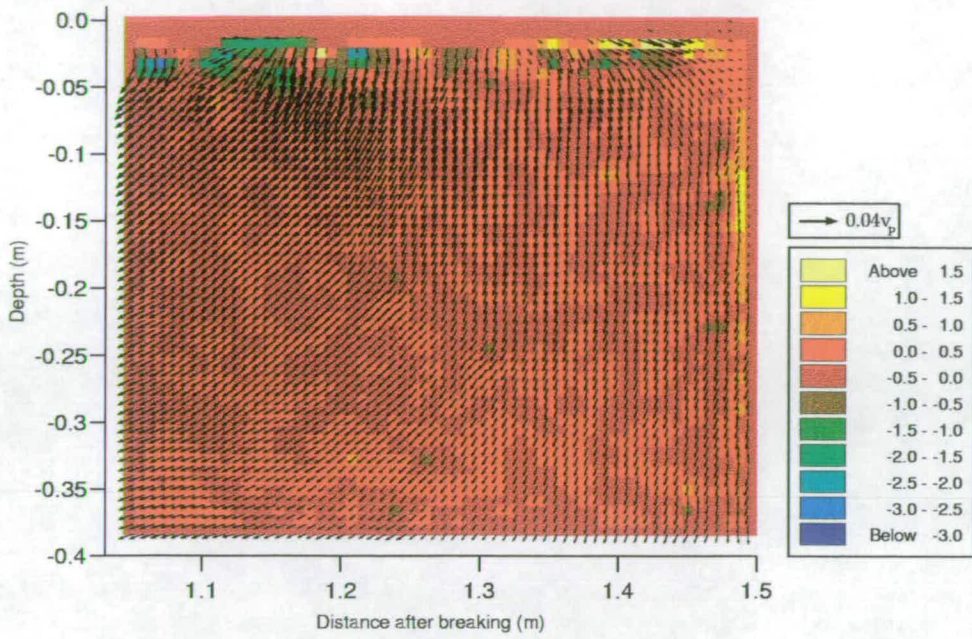
Figure 4.51: Vorticity levels (s^{-1}) for spilling breaker at position 4, T=1.70s
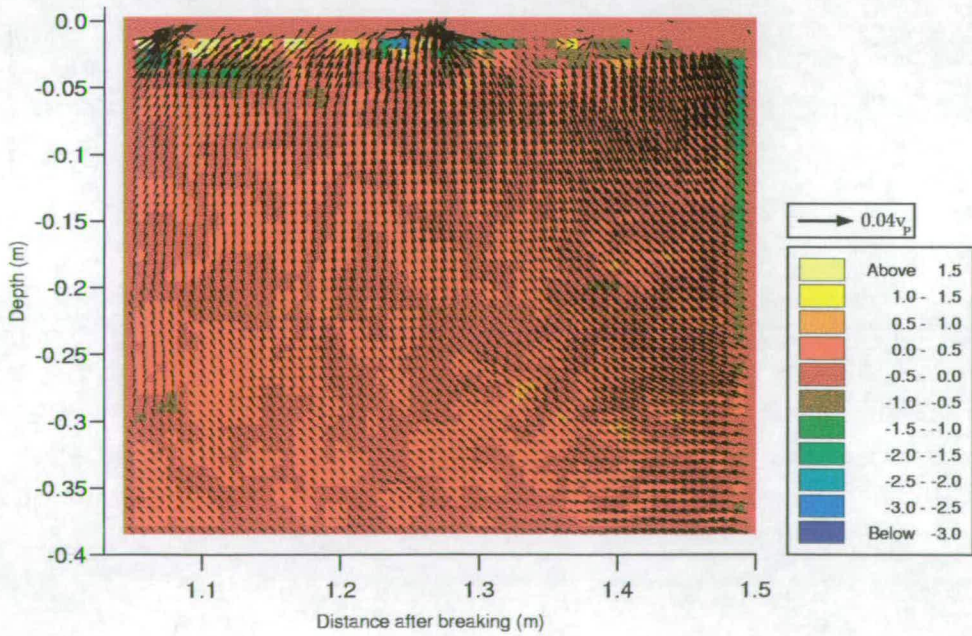
Figure 4.52: Vorticity levels (s^{-1}) for spilling breaker at position 4, T=2.45s
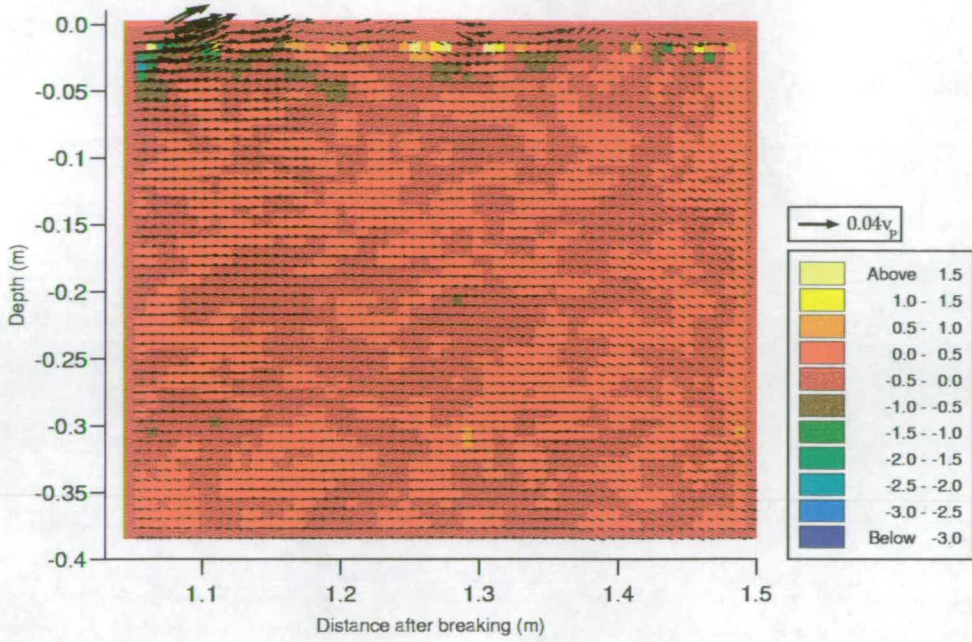
Figure 4.53: Vorticity levels (s^{-1}) for spilling breaker at position 4, T=3.20s
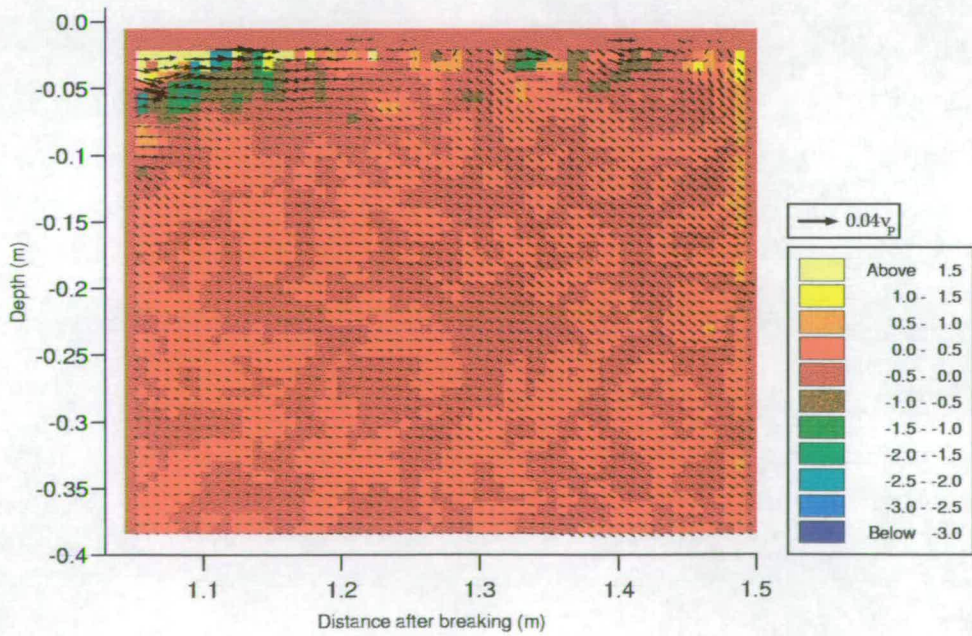
Figure 4.54: Vorticity levels (s^{-1}) for spilling breaker at position 4, T=3.95s
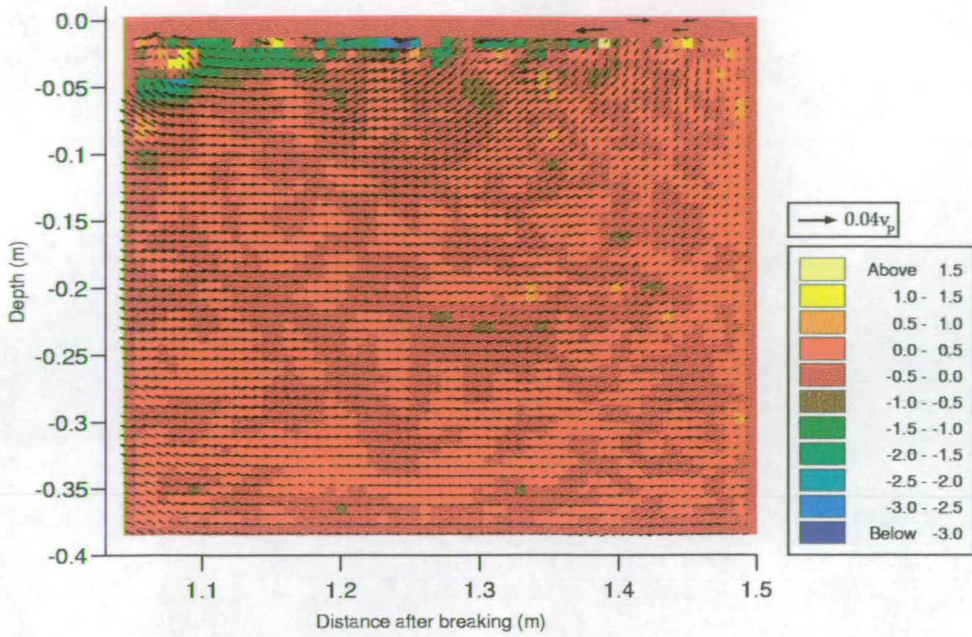
Figure 4.55: Vorticity levels (s^{-1}) for spilling breaker at position 4, T=4.70s
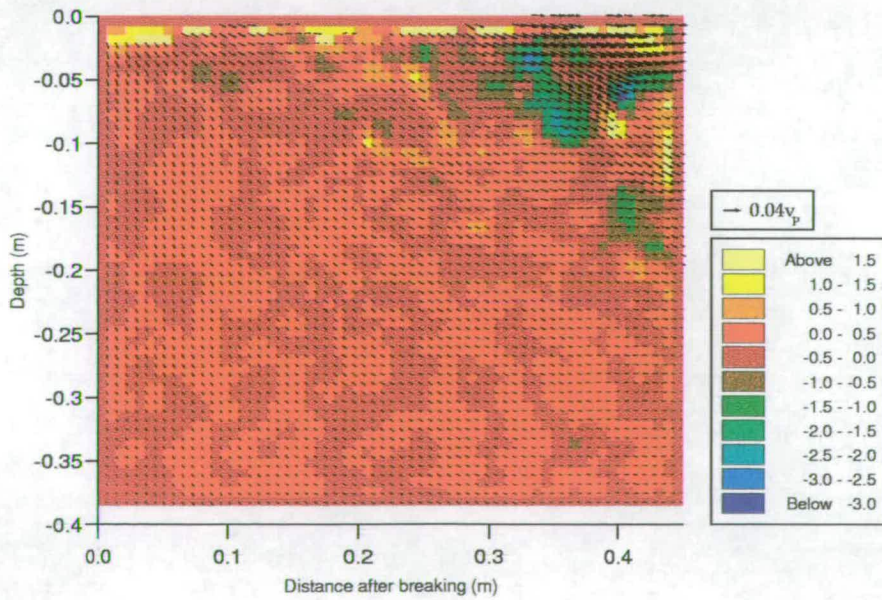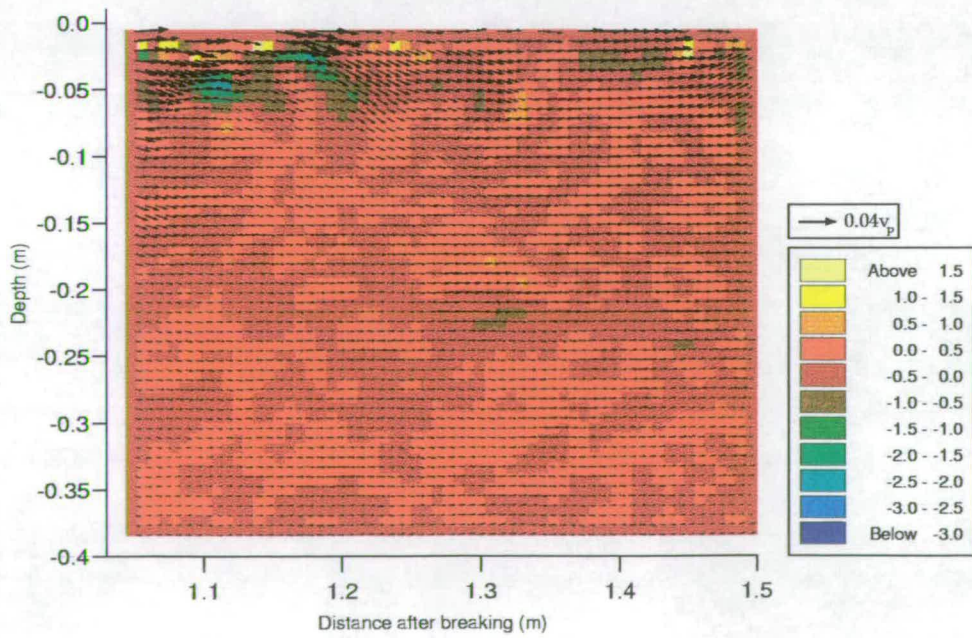

Figure 4.56: Vorticity levels (s^{-1}) for spilling breaker at position 4, T=5.45s
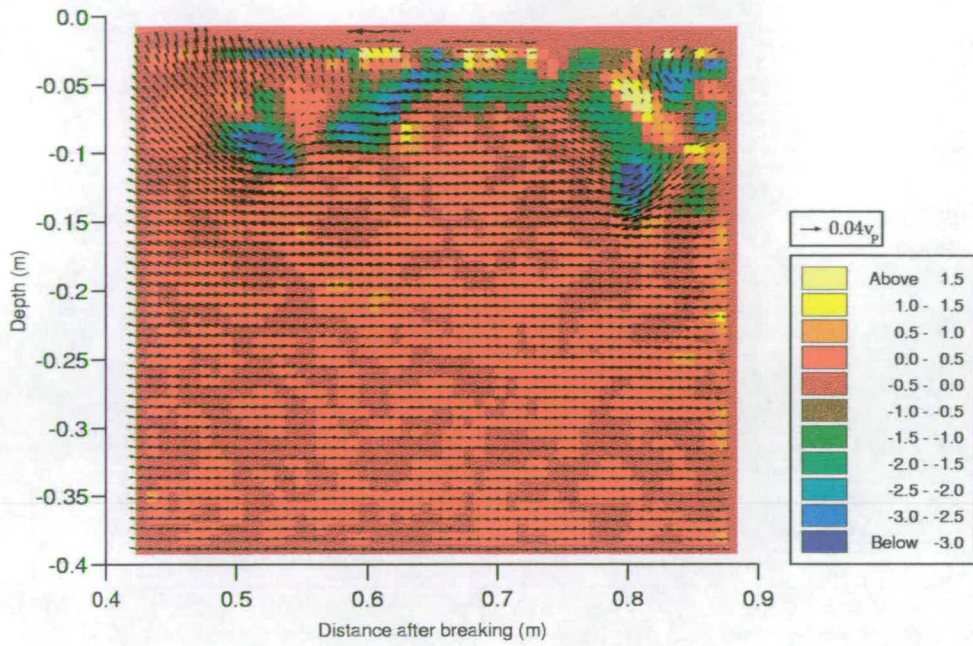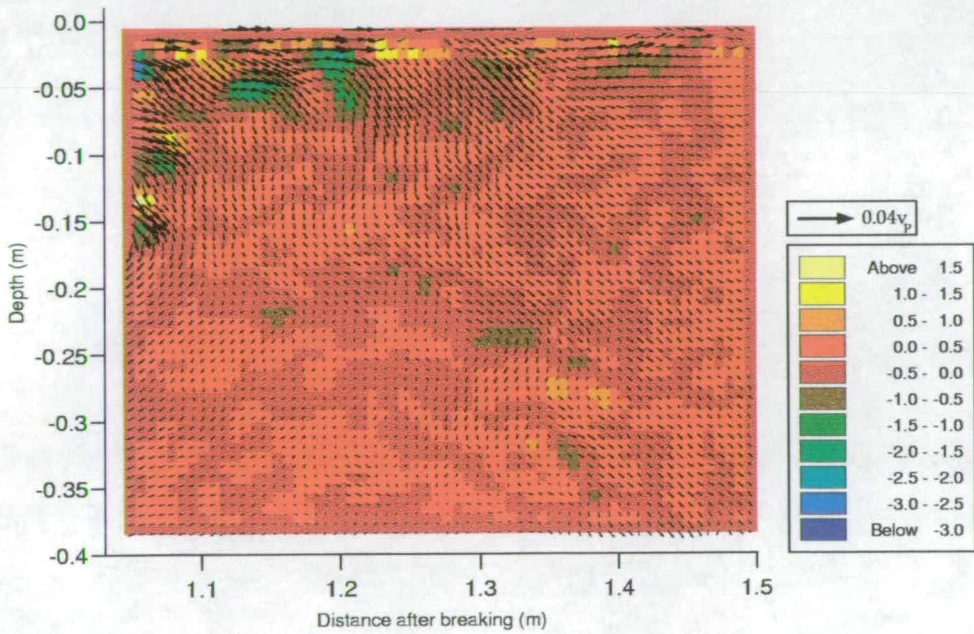
Figure 4.57: Vorticity levels (s^{-1}) for spilling breaker at position 4, T=6.20s

Chapter 5

Turbulence Created by Spilling and Plunging Waves

5.1 Summary

In this chapter a quantitative analysis of the post-breaking flow is presented. The surface profile data obtained from wave gauge measurements are utilised to describe the relative spectral differences between the pre-breaking and post-breaking surface motion. It is concluded that low frequency waves propagate through the region without significant loss of energy and that high frequency waves contribute more to the breaking event.

Turbulent quantities are derived from PIV data for both plunging and spilling breakers. Turbulent velocities are extracted using a local averaging technique to remove the mean-flow components. This is outlined and discussed in chapter 3.

The spatial decay of turbulence levels in the near-surface region is investigated. Depth profiles of turbulent kinetic energy and root mean-square horizontal turbulence are presented for both waves at all experimental positions. These enable the extent and form of the mixing and the value of turbulence levels to be discussed. Direct comparisons are made with the work of Rapp and Melville [56] with broad agreement reached.

Power laws are fitted to the depth profiles which, in many cases, have two

distinctly separate regimes. The mechanism behind the creation of these regimes and the values of the power-law relationships are discussed in the context of existing turbulent theories. The study is also extended, with the analysis developed in this thesis performed on data from a similar study. This is shown to further justify the conclusions reached.

The decay of the total turbulence over the time period that the experiment was performed is calculated for each wave. The turbulence decays inversely with time.

Finally the power spectra are calculated for the upper layer of the experimental region. These are shown to be in close agreement to theoretical and experimental results from other researchers. Explanations relating to the form of the spectra are offered, with some evidence of a fundamental difference between the spectra for the different waves.

5.2   Surface profile spectra

Surface elevation profiles are effective in showing how the energy from the initial wave packet is distributed within the breaking region. Figures 5.1 and 5.2 show the surface profiles from wave-gauge measurements made just downstream of the breaking point, for both waves used in this study. The records are referenced with respect to the theoretical breaking time, taken as the instant at which the input waves were focussed, t_b.

In both cases there is considerable surface movement after the wave has broken, reinforcing the observation that there is significant wave related motion present in the PIV velocity records acquired. For example there is a large after breaking component present at around the time that the first image is acquired
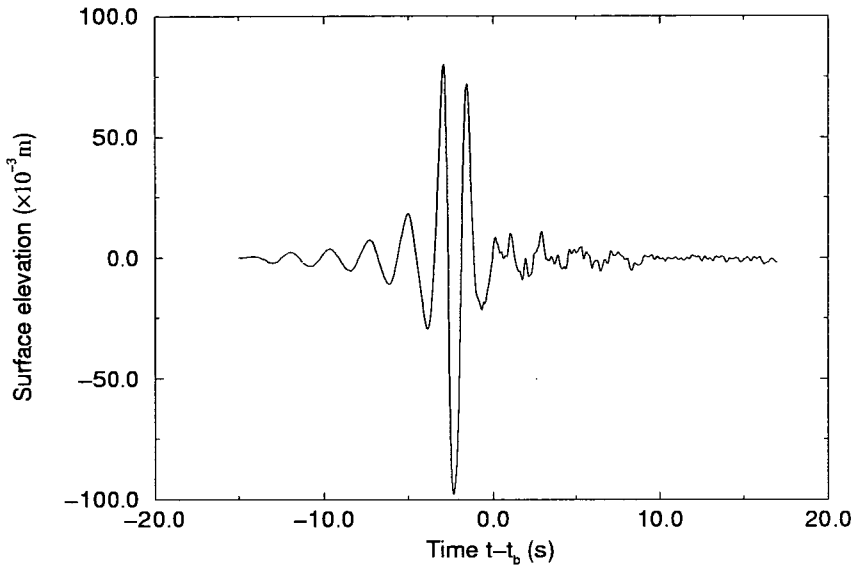
Figure 5.1: Surface elevation profile for the plunging breaker recorded just downstream of the breaking point
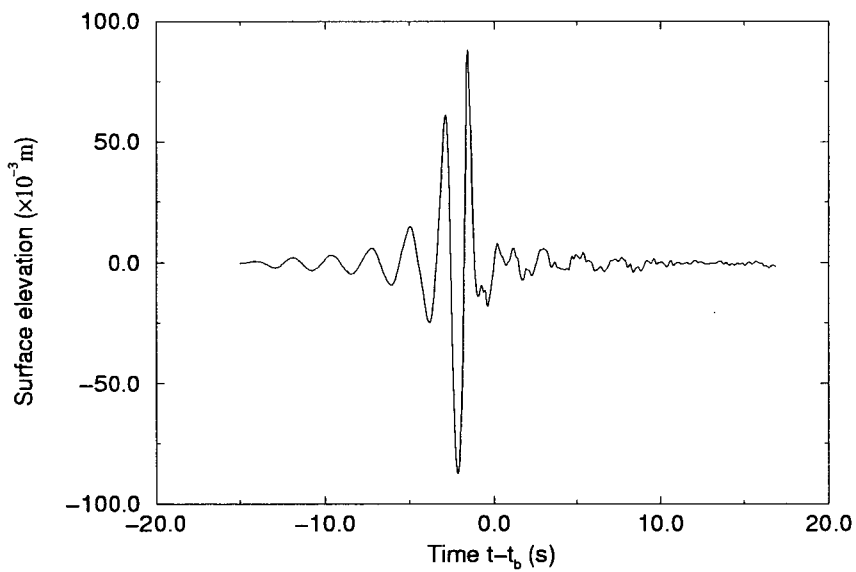
Figure 5.2: Surface elevation profile for the spilling breaker recorded just downstream of the breaking point

and then another peak at about 4s after breaking, which corresponds to the the fifth and sixth images out of the sequence of seven.

Figures 5.3 and 5.4 show the spectra of these surface profiles before and after breaking. The plunging breaker loses a large amount of energy from the high-frequency part of the first harmonic and all of the second harmonic, while the spilling breaker loses energy from these frequencies in much smaller proportions. This shows that the amount of energy deposited into the water as a result of plunging breaking is considerably higher than for spilling.

It appears from these results that low frequency waves propagate through breaking without significant loss of energy. This occurs in both of the wave examples. High frequency waves are required to obtain the required steepness for ocean breaking and since the plunger is a more extreme wave, there is a more dramatic decrease in these frequencies in this case.

5.3 Turbulent mixing

The spatial distribution of turbulence in the upper layer indicates the extent of mixing caused by the breaking event. The variation and form of this distribution over time, space and with the different waves, should be quantified.

A 19x19 vector spatial average was used to approximate the mean (non-turbulent) flow at each point in a vector map. This value was then subtracted from the measured velocity value, resulting in the removal of all spatial frequencies that have fluctuations of scales greater than this size, equivalent to a wavelength of about 15cm.

The mean square turbulence (MST) at each point in the flow is calculated by squaring the horizontal and vertical turbulent velocities, then averaging them
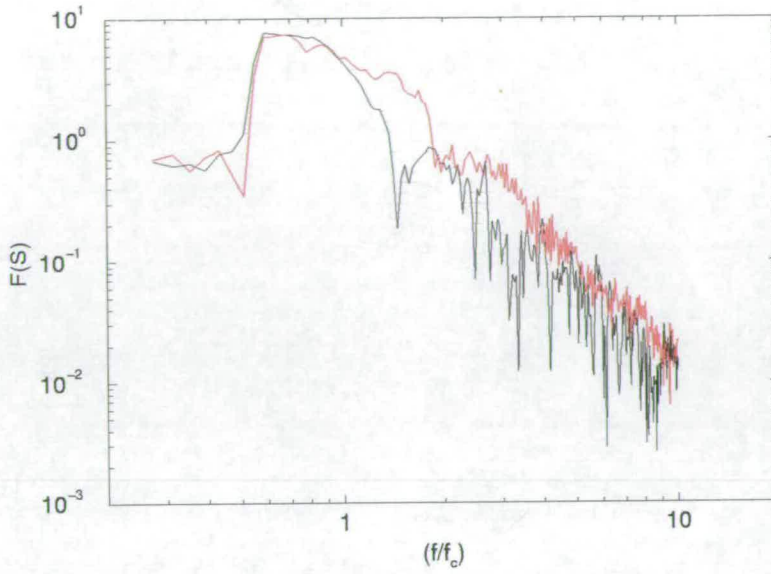
Figure 5.3: Surface elevation spectra for plunging breaker before and after breaking (red shows spectra before the breaking point)
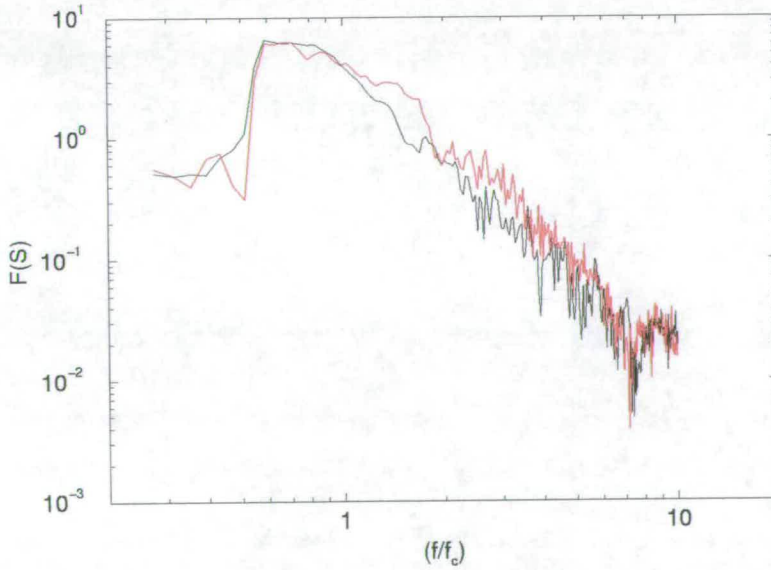
Figure 5.4: Surface elevation spectra for spilling breaker before and after breaking (red shows spectra before the breaking point)

horizontally for each line, yielding vertical (depth) profiles of the turbulence. The MST values are non-dimensionalised with v_p^2, the square of the phase velocity of the central component of the wave packet, while the depth is scaled with k_c, the wave number of the central component of the input spectrum.

5.3.1 Observations from turbulence depth profiles

The nature of the turbulent kinetic energy profiles, particularly the extent of the vertical mixing are demonstrated effectively when displayed on log-linear graphs. These are shown for each of the four different positions studied, with the profiles for the plunger and spiller displayed on the same axes. Figure 5.5 shows typical turbulence profiles for the two breaker types at the first and second positions studied. The turbulence falls off with depth for both cases and reaches a small, constant value that we can call a negligible level of turbulent energy that corresponds to the point where noise become dominant over turbulence (this is further discussed in the next section).

The turbulence extends to a non-dimensionalised depth of approximately 0.4 for the spiller and 0.6 for the plunger, at position 1. This compares with depths of 0.5 and 0.7 respectively for position 2. Figure 5.6 show the two further regions of experimentation. At position 3 the spiller has mixed to a depth of just over 0.6 and the plunger to just over 0.8. The turbulence at the final position extends to depths of 0.4 and 0.7 for the spiller and plunger respectively.

These depth values can be compared to the non-dimensional amplitudes of the respective waves, which are 0.309 and 0.366 respectively. The maximum depth to which the spilling breakers' turbulence appears to mix within this timescale is about double the wave amplitude, while the plunger mixes to a maximum that is greater than double the amplitude.

The fact that the mixing is a maximum in region 3 confirms the visual analysis
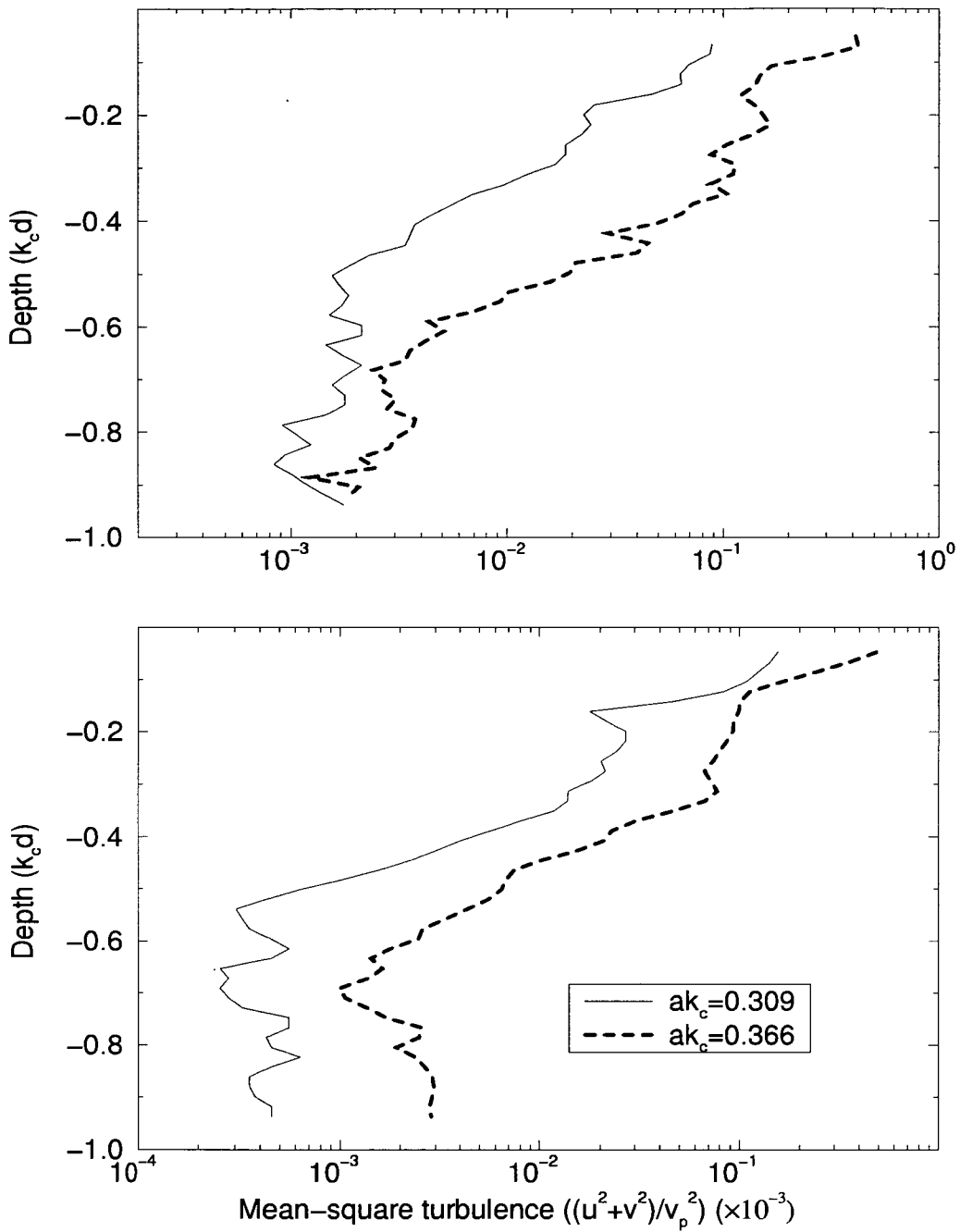
Figure 5.5: Turbulent energy against depth for the spilling and plunging breakers at positions 1 and 2.
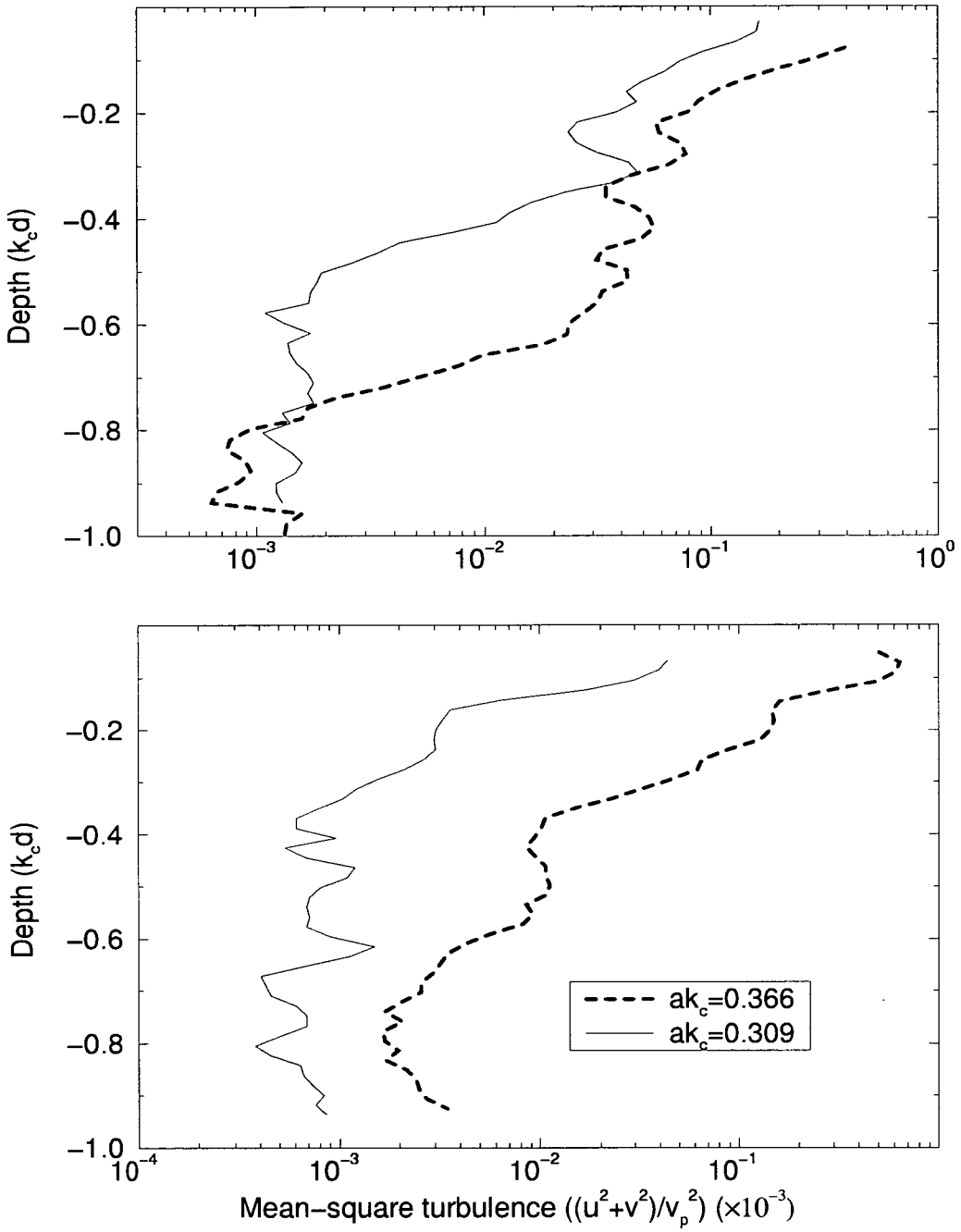
Figure 5.6: Turbulent energy against depth for the spilling and plunging breakers at positions 3 and 4.

of the vorticity maps presented in chapter 4, where it was described in terms of the secondary wave-motion pushing the fluid downwards at this point.

Although the results presented here are typical, there is deviation in the degree of mixing when the experiments are repeated, reflecting the unpredictable nature of the post-breaking flow. On visual inspection of the breaking process, variations in the vorticity field can be observed. The extent to which the plunging jet and the subsequent secondary wave-motion (as discussed above) mixes the fluid, appears to vary.

Figures 5.7 and 5.8 show the scatter of the turbulence profiles from repeats of the experimental data, captured at the same instant of time after breaking for each wave. The motion near the surface is, as expected, more unpredictable and varried than near the bottom. The variation in the depth at which noise becomes dominant is likely to be due to fluctuations in the noise level when repeat experiments are performed (this is of the order $0.1k_cd$). The near-surface variations are due to the unpredictability of breaking.

There is no apparent evolution in the depth of mixing with time. The overwhelming part of the mixing occurs in the instants just following breaking, before any measurements were taken. The vertical mixing that may still be occurring, will be slow and non-uniform throughout the flow and is unlikely to be noticeable over the 4.45s that the flow is measured. Also, wave components travelling through the region during this period of study, may disguise the true position of the turbulence, contributing some oscillation to the flow.

5.3.2 The mixed layer

In figures 5.9 to 5.16 the depth profiles are shown on log-log graphs, with depth increasing down the page. The profiles are presented for the four different positions at which the waves were studied and for both waves.
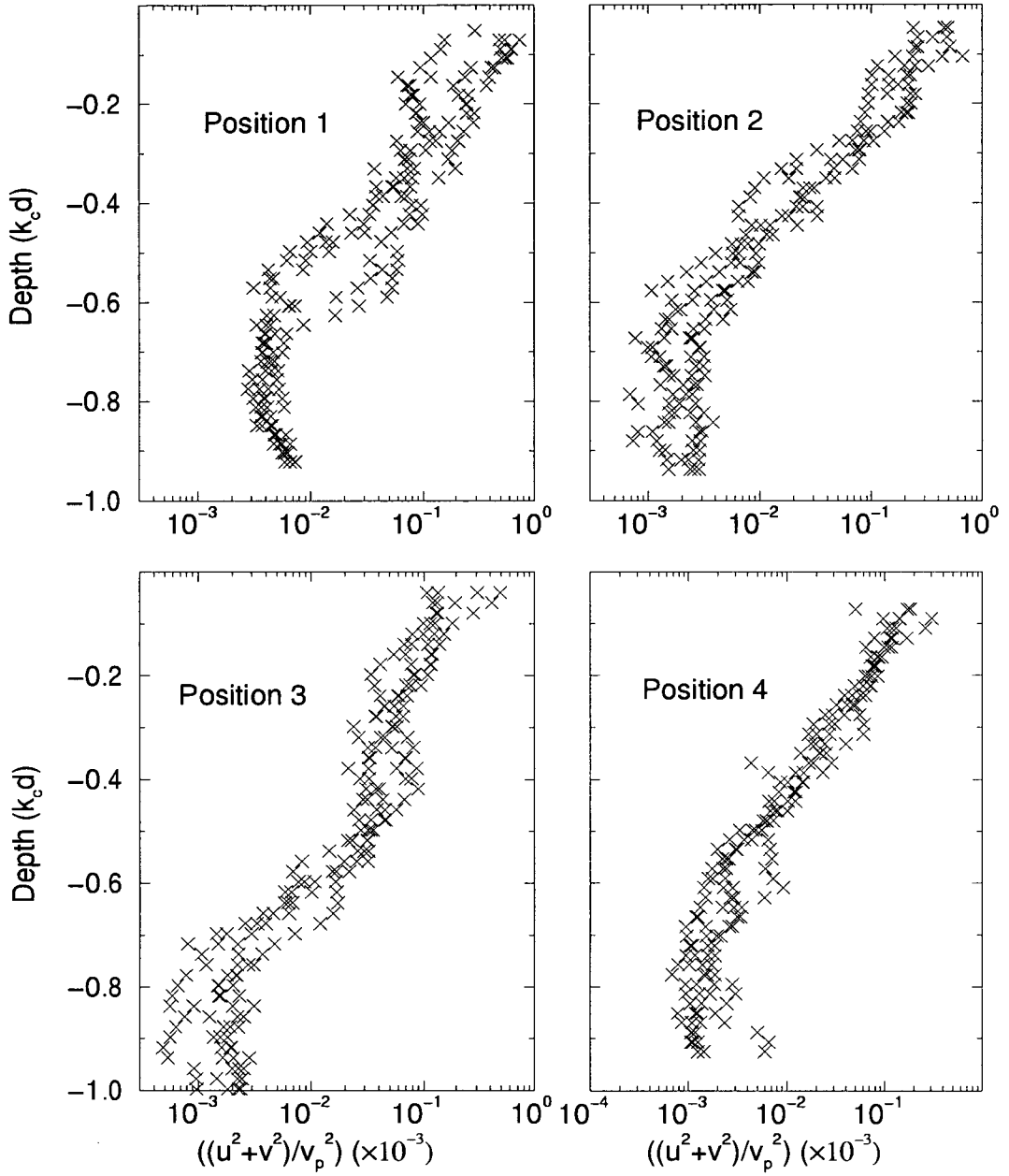
Figure 5.7: Turbulent energy profiles showing the variation in vertical mixing at position 1-4 for the plunging breaker.
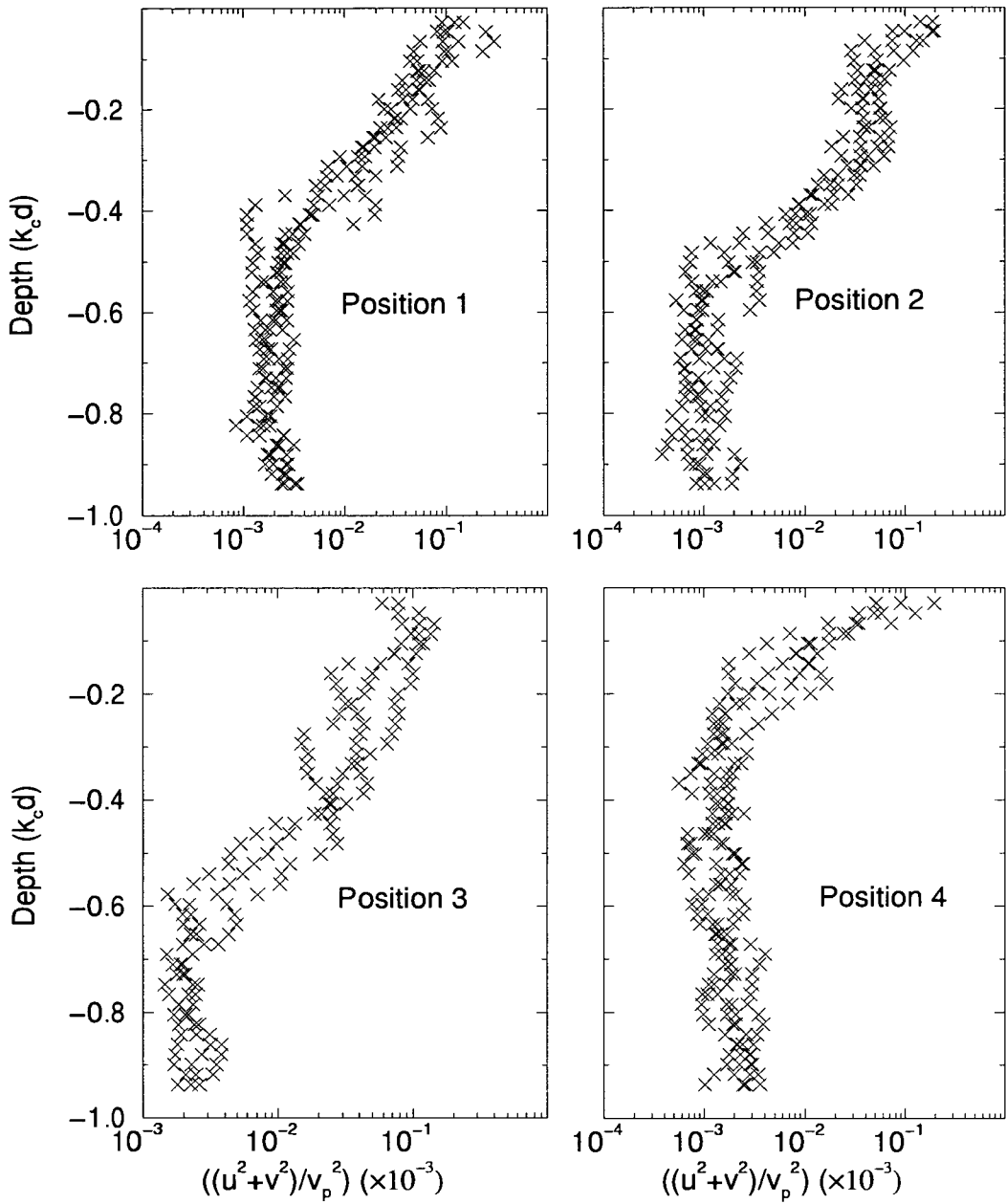
Figure 5.8: Turbulent energy profiles showing the variation in vertical mixing at position 1-4 for the spilling breaker.

In the majority of the graphs, two separate regimes can be identified. The near-surface region shows the turbulence level decaying slowly with depth, compared to the deeper region, where the levels fall off rapidly to a constant level. For both waves this feature is most prominent in regions 2 and 3.

There is no clear trend to the precise depth of the transition point between the two different parts of the profiles. Sometimes there does appear to be a deepening of the upper region between successive instants but this does not continue over longer periods.

For the plunger, the enhanced layer extends to a depth of between 0.3 and 0.4 at position 1 and position 2, 0.5 at position 3 and 0.3 at position 4. This compares to between 0.2 and 0.3 at position 1, 0.3 at position 2 and approximately 0.4 at position 3 for the spiller. These depths are comparable to the non-dimensionalised wave amplitudes which are 0.366 and 0.309. For the spiller, there is no clear upper-layer at position 4, it either does not exist or, is so close to the surface that it cannot be identified.

The enhanced layer for the plunger is largest in region 3, where deeper mixing occurs. The maximum turbulent intensities exist in region 2, which corresponds with the observations (made from the vorticity maps) that the strongest, most intense vortices exist here. However, at any arbitrary depth below the surface layer, the turbulence levels are greater at position 3, a direct result of the deeper mixing. Two individual profiles for region 2 and 3 are shown in figure 5.17, illustrating this point. A feature that is worth noting is that the gradient of the lower region is different for the two cases. The significance of this is subsequently discussed in section 5.3.4. This is not so clearly displayed in the case of the spiller, mainly because the turbulence is more evenly spread throughout the breaking region rather than being distributed in patches.
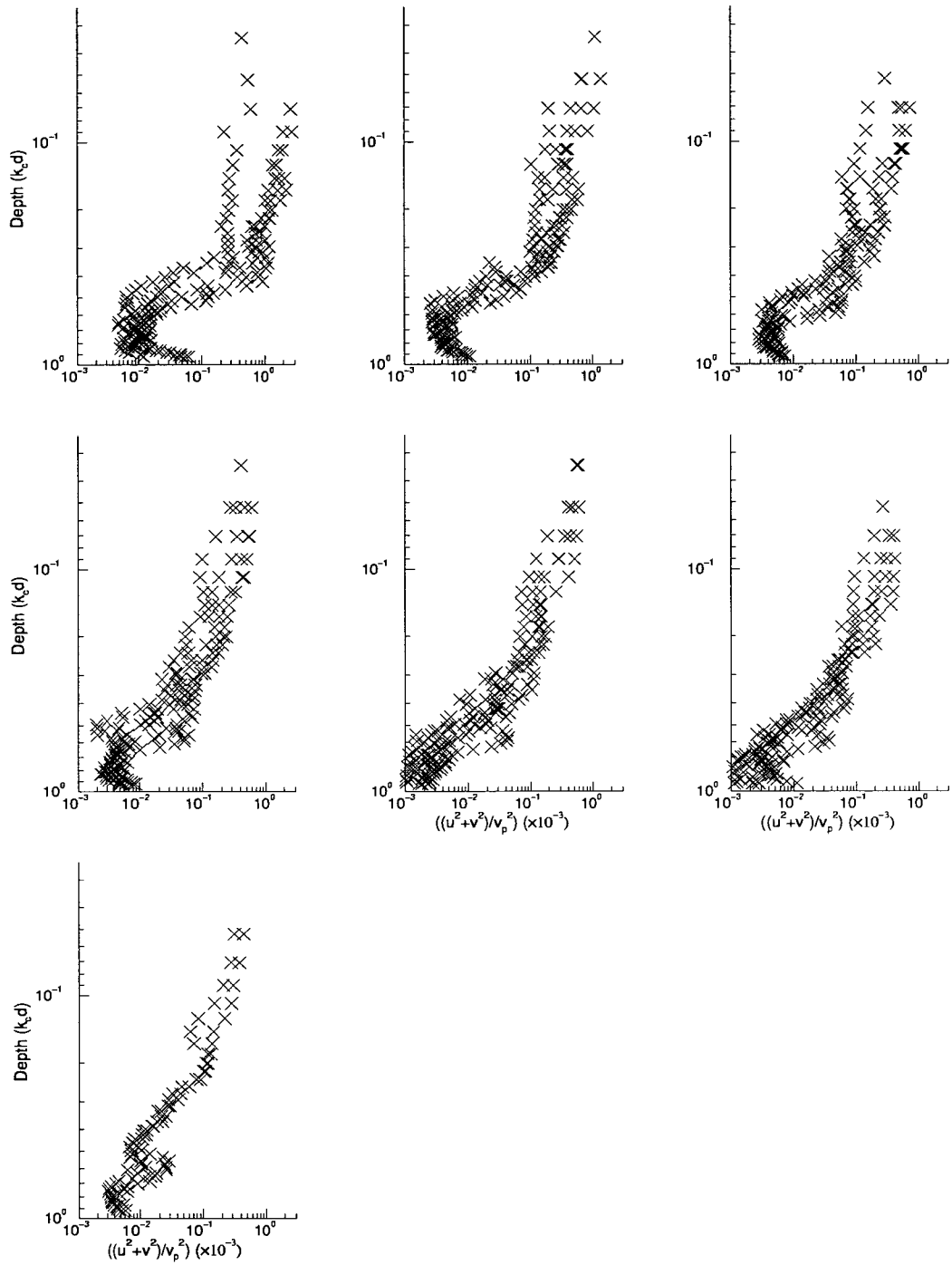
Figure 5.9: Evolution of turbulent energy profiles for the plunging breaker at position 1 from t=0.95s (top left) to t=5.45 (bottom).
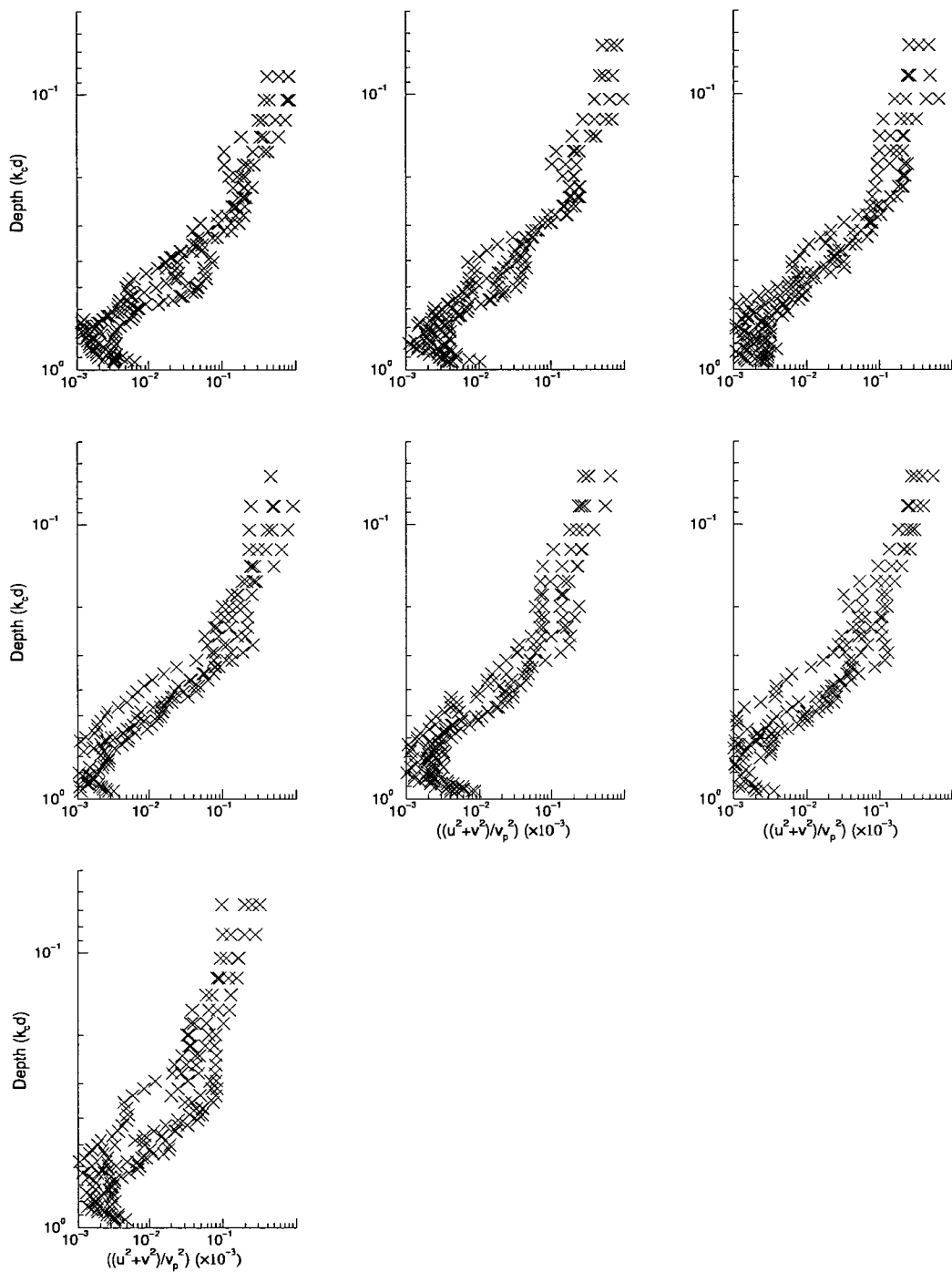
Figure 5.10: Evolution of turbulent energy profiles for the plunging breaker at position 2 from t=1.7s (top left) to t=6.2 (bottom).
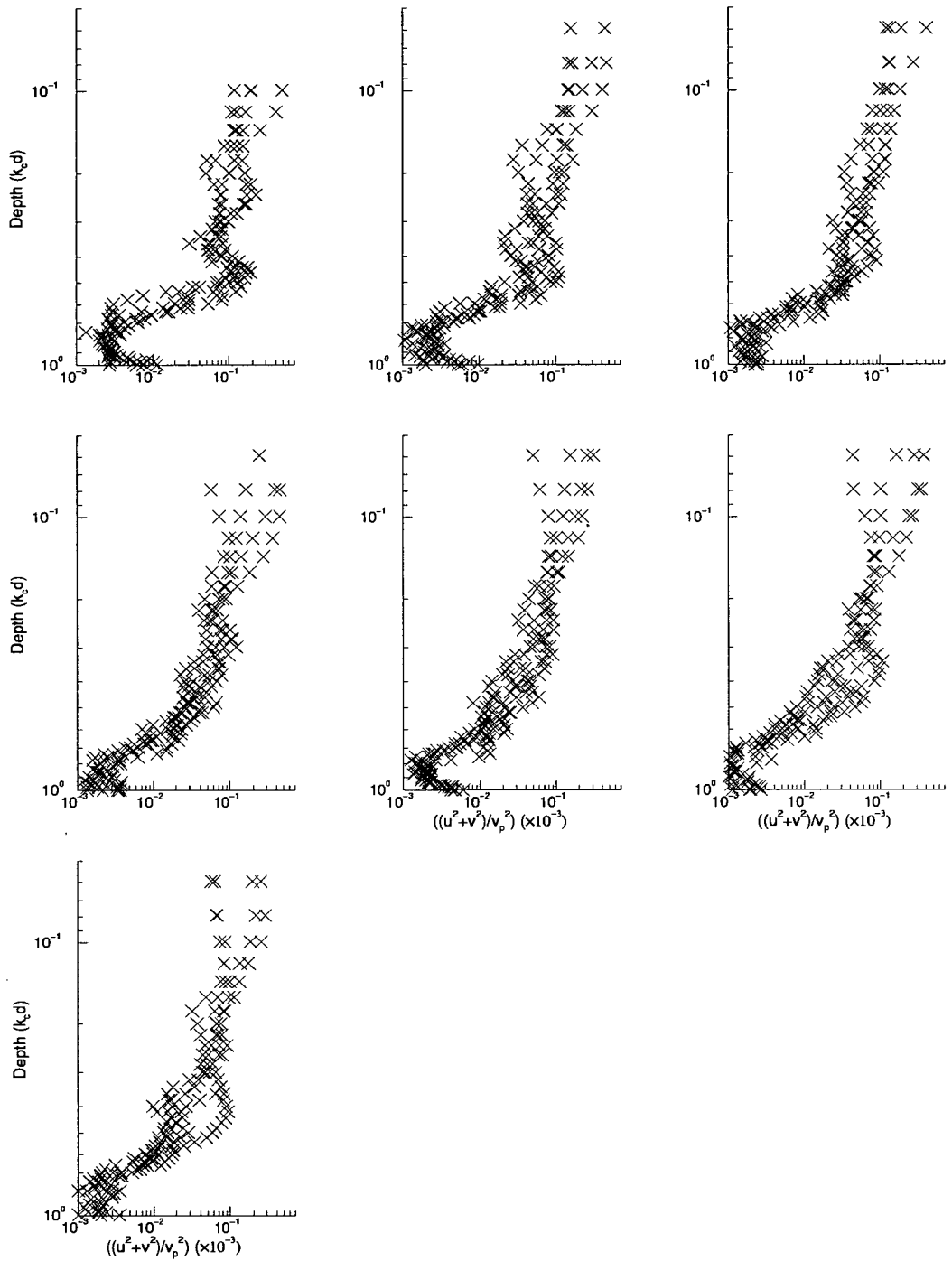
Figure 5.11: Evolution of turbulent energy profiles for the plunging breaker at position 3 from t=1.7s (top left) to t=6.2 (bottom).
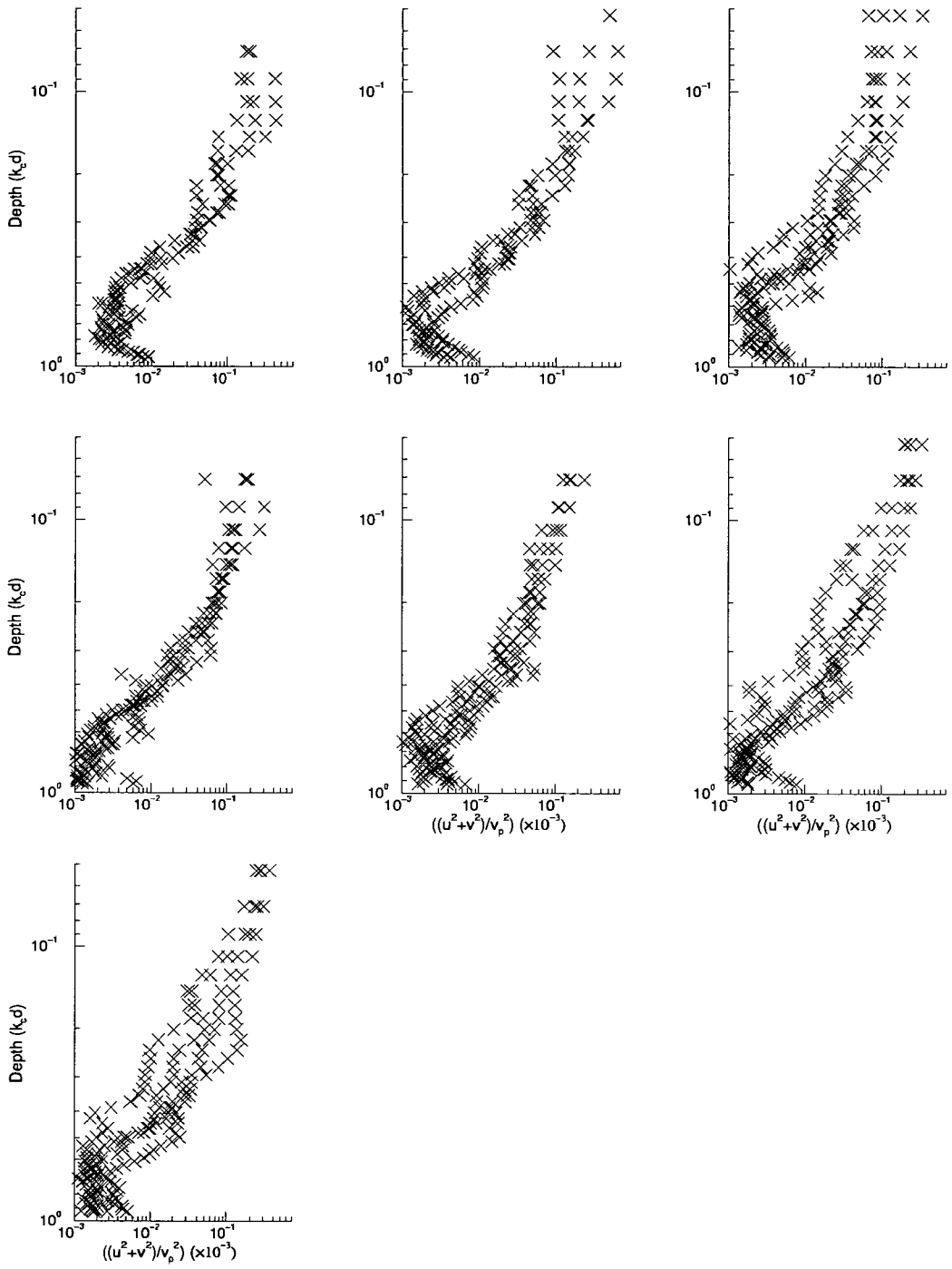
Figure 5.12: Evolution of turbulent energy profiles for the plunging breaker at position 4 from t=1.7s (top left) to t=6.2 (bottom).
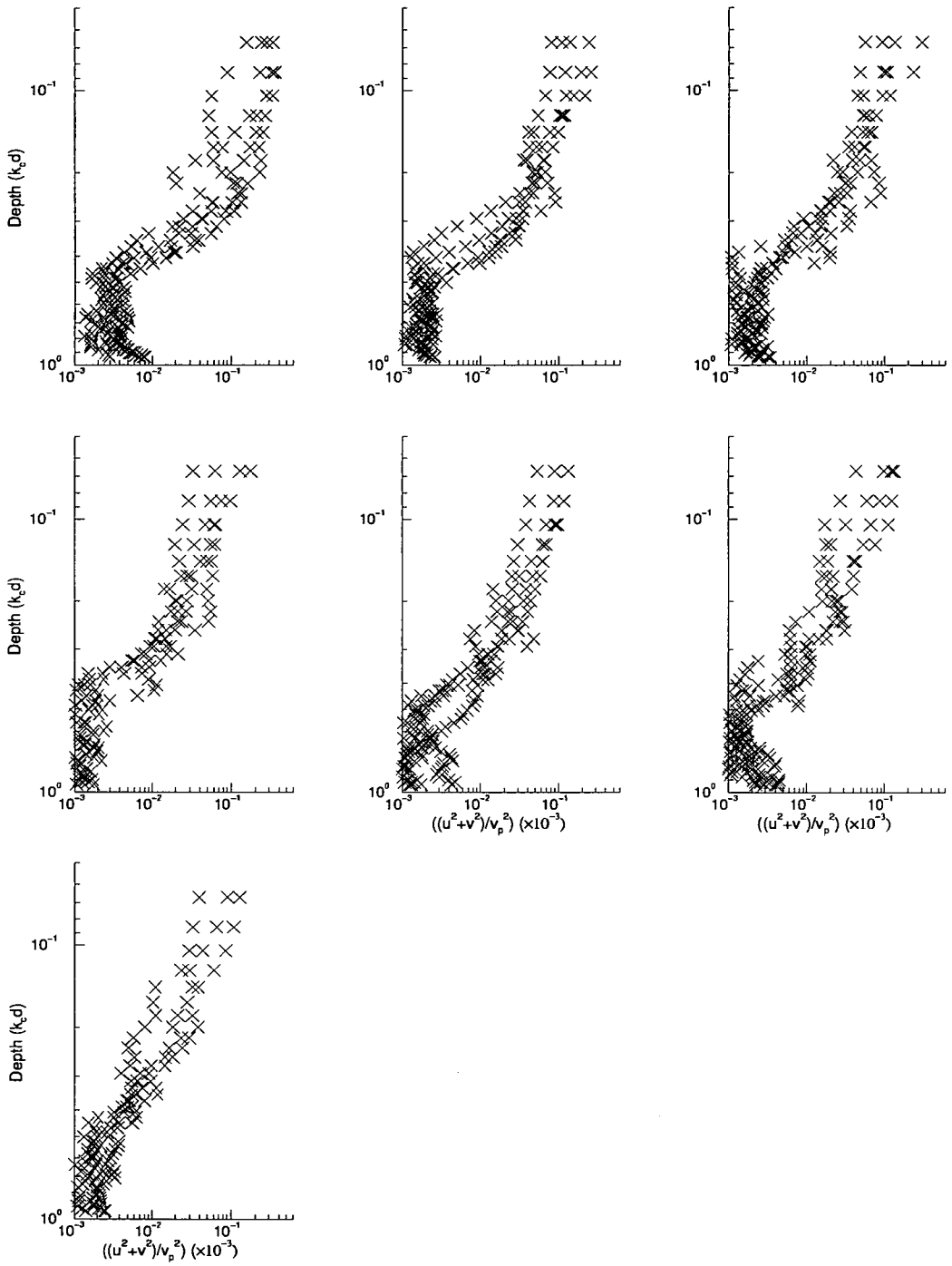
Figure 5.13: Evolution of turbulent energy profiles for the spilling breaker at position 1 from t=0.95s (top left) to t=5.45 (bottom).
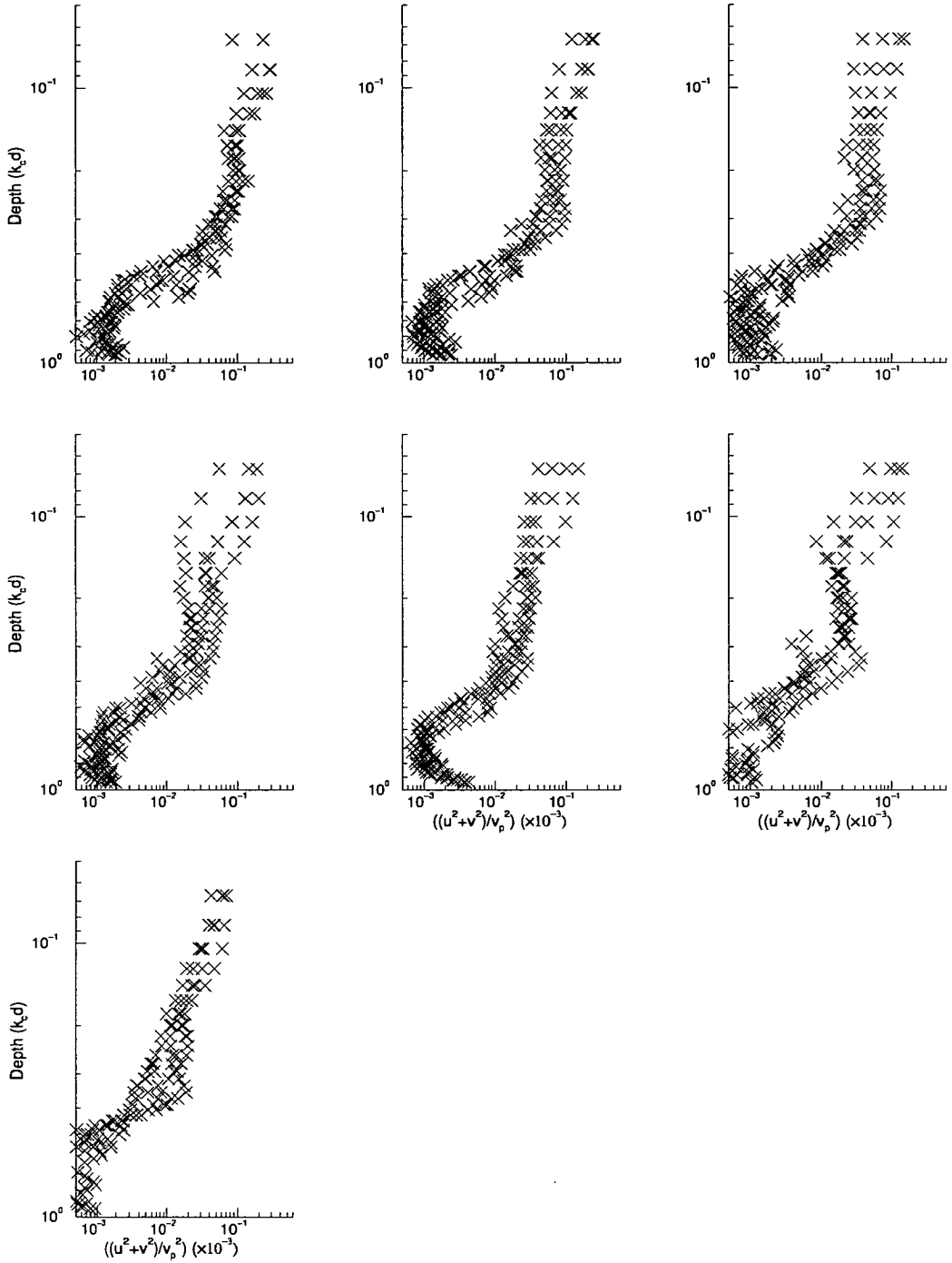
Figure 5.14: Evolution of turbulent energy profiles for the spilling breaker at position 2 from t=1.7s (top left) to t=6.2 (bottom).
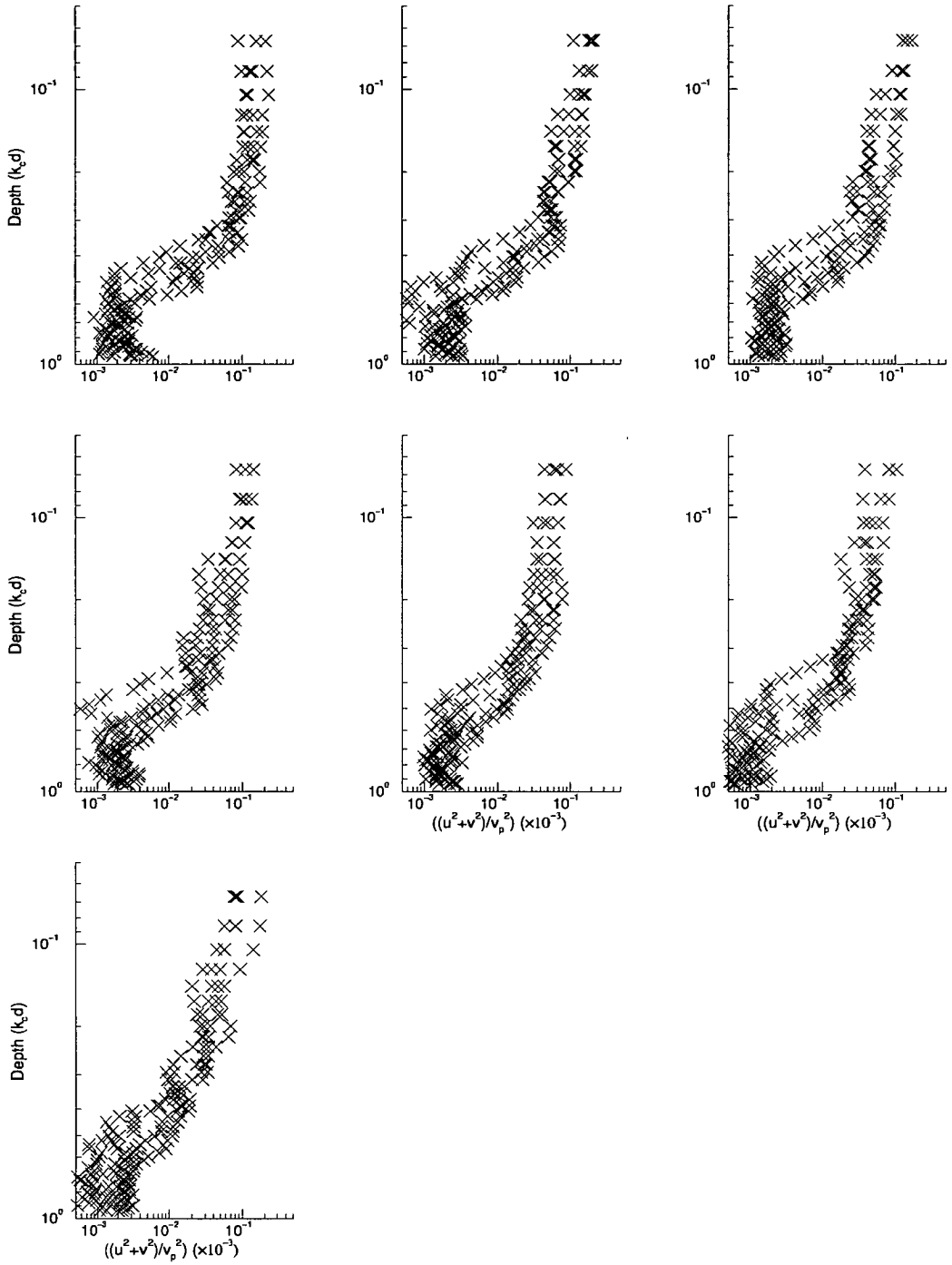
Figure 5.15: Evolution of turbulent energy profiles for the spilling breaker at position 3 from t=1.7s (top left) to t=6.2 (bottom).
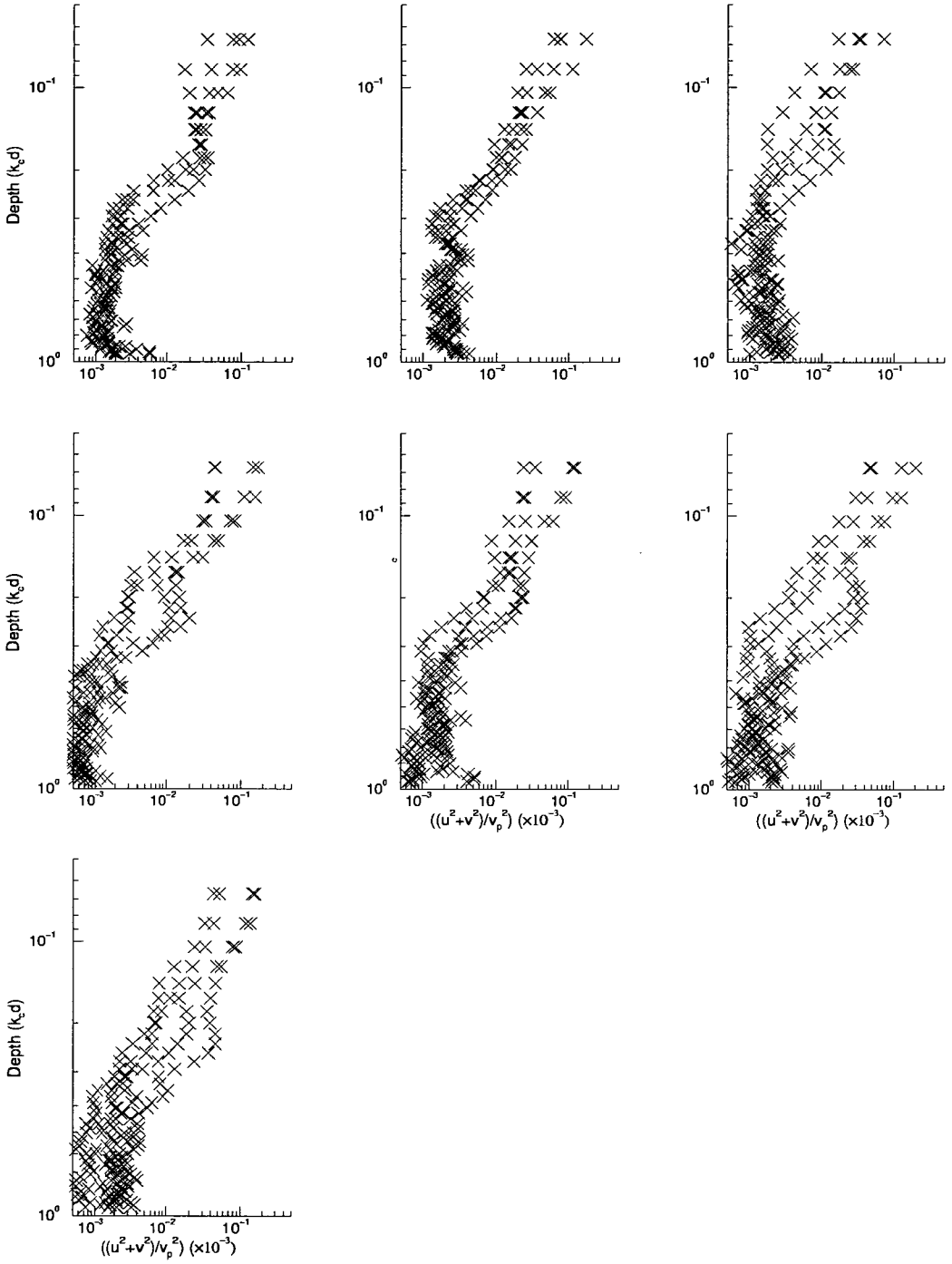
Figure 5.16: Evolution of turbulent energy profiles for the spilling breaker at position 4 from t=1.7s (top left) to t=6.2 (bottom).
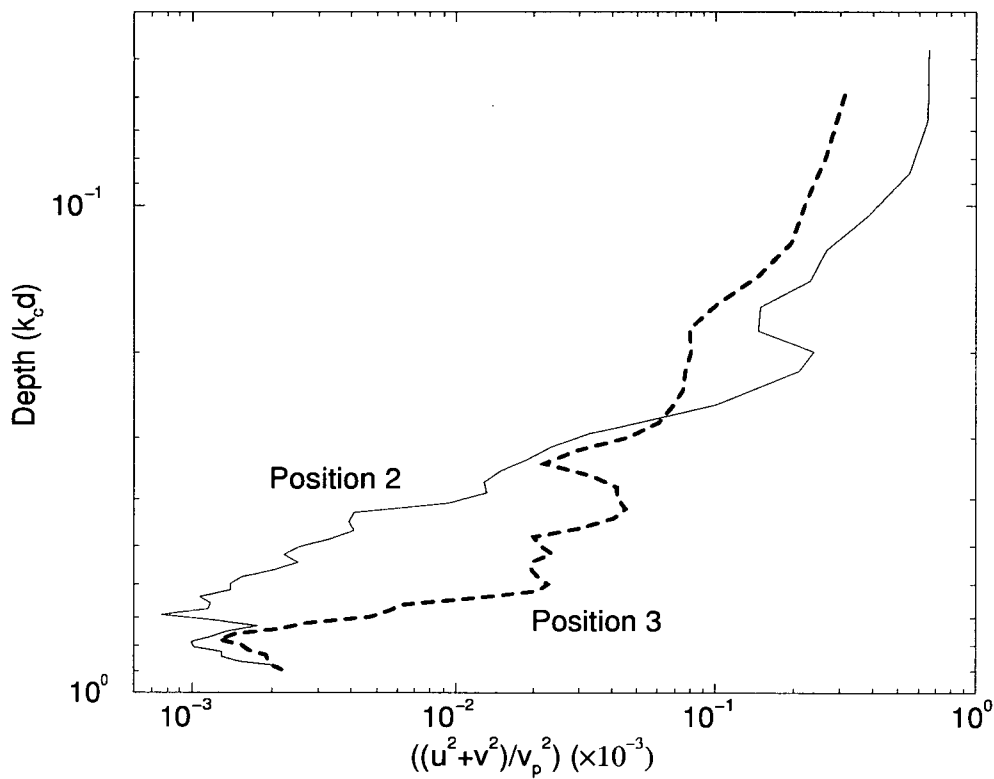
Figure 5.17: A comparison between depth profiles at positions 2 and 3.

In order to characterise the profiles, best-fit lines are fitted to the two regions using a least-squares regression fit of a line of the form $y = Ax^B + C$, which assumes that the form of the decay is a power-law. The value of B can be inferred by measuring the gradient of the best-fit line on the log-log plot. The gradients of the deeper region vary from approximately -0.2 to -0.3, while the near surface region shows slightly less consistent behaviour and varies between -0.4 and -0.6.

5.3.3   Evolution of depth profiles over long time periods

For comparison, results from a complementary study of breaking waves in a similar wave flume at Edinburgh University, will be presented here. The data was collected by David Hann and was a study of breaking waves using a cross-correlation PIV system (see Arnott *et al* [4]) with a lower camera resolution but a capacity to take a longer time-sequence of data. The local averaging method for extracting turbulent information, developed by the author, was again used on this data-set, removing approximately the same spatial scales as before. The longer time sequence enabled a more comprehensive analysis of the evolution of vertical mixing to be made, along with providing additional confirmation of conclusions already stated in this study.

In the comparative study a plunger was created that had a small amplitude ($a = 0.0525m$) but large wavenumber ($k_c = 6.542m^{-1}$), giving a non-dimensional amplitude of $ak_c = 0.3435$. This compares with $ak_c = 0.3656$ in this study. Data was acquired for times ranging from approximately 6 to 20 wave periods after breaking, compared to about 1.5 to 5 in the data taken by the author. A comparison between two typical profiles from each dataset are shown in figure 5.18. Even though the times are very different there are definite similarities that demonstrate the legitimacy of the method of scaling parameters used in this
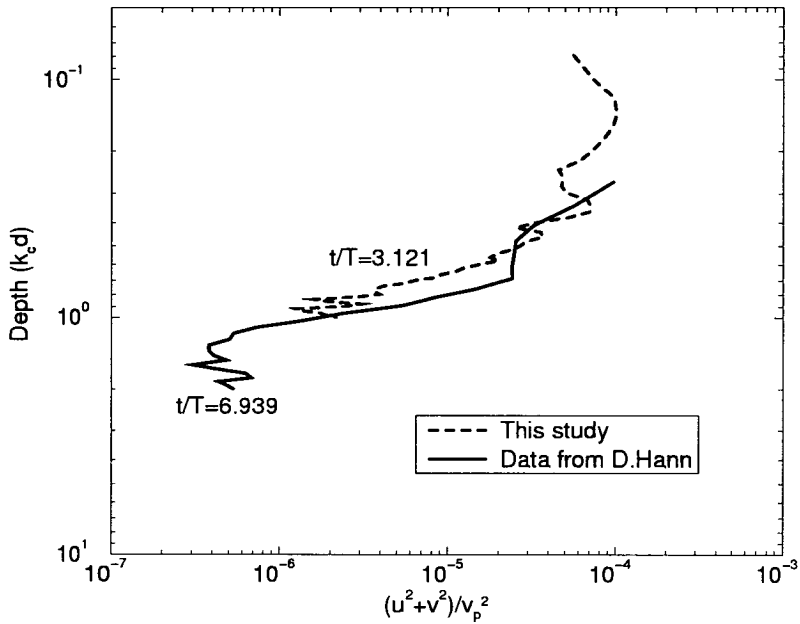
Figure 5.18: Comparison between this study and a similar study in a different flume with a different plunging breaker. The times after breaking have been non-dimensionalised using the wave period T.

study. The gradients of the upper and lower sections of the profiles appear to be the same, although the range of resolved energies differ. The transition point between the two regimes of the graph is deeper for the comparative study, which is to be expected as this is a later time after breaking. An interesting feature of the graphs are that even though the data from this study is taken at an earlier time the turbulence levels in deeper water are smaller. This is likely to be due to differences in the breakers used. The breaker in the comparative study has a significantly larger wavenumber which causes increased recirculation within the wave flume. This recirculation will have the effect of increasing the shear and hence increasing the turbulent velocities in the lower part of the flume.

The final aspect of the comparison is the greater resolving power of the second
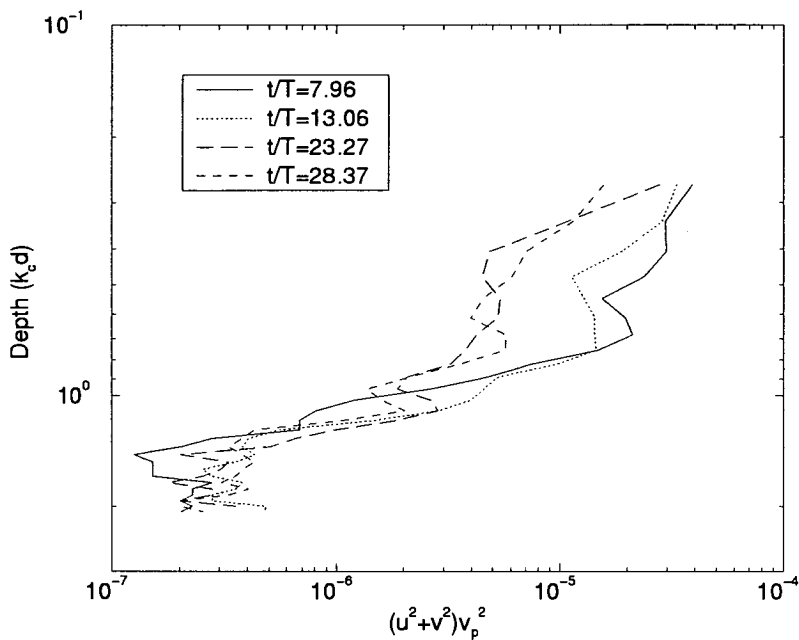
Figure 5.19: Four example profiles from secondary study of breakers.

study, where smaller turbulence levels can be detected. This illustrates the loss of resolution that image shifting causes and the advantages of using cross-correlation to study turbulence.

Figure 5.19 shows a sequence of turbulent depth profiles for data from the second study, covering a much longer time period than the first study. These show similar individual characteristics to the data already presented, while collectively they show the upper region extending further with time. The four profiles shown are for two instances closer to the breaking time and two at some time later. The deepening of the upper mixing layer can be clearly seen between the first two profiles and then quite appreciably between the second and third profiles while there is hardly any noticeable difference between the third and the fourth profiles.

Rapp and Melville [56] measured the deepening of the mixed layer by looking

at the depth to which dye had mixed and fitted a $t^{1/4}$ relation to the data, that was followed closely after all the remnant wave components had dispersed. This proposed relation is not investigated here, although something of that form is implicated by the decrease in deepening of the upper layer in the later pair of profiles. The dye measurements of Rapp and Melville [56] are useful, but direct comparisons must be made carefully. In this case a dyed patch was used to indicate the region of the flow that was turbulent. This may not compare directly to the enhanced upper layer discussed here.

5.3.4 Analysis of spatial turbulence decay

The results outlined above have several important implications that need to be emphasised. Firstly the decay of the mean-square turbulence has been identified as occurring in two distinct regions which can be approximated by different power-law relationships. The upper region is a heavily mixed-up region, analogous to homogeneous turbulence and contains the most intense levels of turbulence. The deeper region is a shear-type flow which is a consequence of the mean current and turbulent vortices shearing the remainder of the flow. These analogies are a very convenient way of describing the flow and are supported by the observations made in chapter 4, where a mixed-up region and a strong surface shear were in evidence.

Using the general expression introduced previously, $E \propto d^{-n}$, where E is the mean square turbulent energy and d is the depth, the range of values of n are 3.8 to 5.3 for the deeper layer and about 1.7 to 2.6 for the near-surface region. This highlights the fact that there are two separate mechanisms creating and sustaining the turbulence. The values of n for the lower layer were generally higher for position 3 than position 2, something that is evident from figure 5.17. This is possibly due to the intensity and two-dimensionality of the vortical structures in

the upper layers being greater in position 2 than position 3, resulting in a less rapid decay of the turbulence.

Thomson and Turner [65] performed experiments using an oscillating grid in water producing decaying homogeneous, near isotropic, turbulence. They suggested this was a good analogy to turbulence produced by breaking waves. The spatial decay power-law that was suggested by their experiments was $u \propto d^{-n}$ where n was close to 1.5. Hopfinger and Toly [34] did similar experiments and proposed that the decay was better represented by a value of n close to 1. They also measured the spatial decay of the turbulent kinetic energy which showed a $E \propto d^{-2}$ relation. Also they repeated the experiment with a perforated grid and obtained a $E \propto d^{-2}$

The results suggested by Hopfinger and Toly [34] fall within the range of values for the power-law calculated here while the results of Thomson and Turner just exceed the upper-bound. There is a fundamental difference between the turbulence studied here and the case of grid turbulence that must be recognised. The grid turbulence is continuously forced by the oscillations while a single breaking wave is an impulsive input of energy. Comparisons must therefore be made carefully and similarities between the two cases not necessarily expected. The fact that the turbulence in this mixed region has evolving isotropy could have a significant effect on the comparison.

The turbulence in the deeper water will be examined further in the next section and related to a shear-type flow.

5.3.5 Decay of horizontal turbulent components

The dominant processes in this flow is the horizontal shear exerted by the near-surface region on the remaining part of the flow. Therefore the vorticity and turbulence is strongly dominated by the horizontal component, the behaviour of

which provides a basis for characterising the turbulence. Furthermore a comparison of the order of magnitude of the rms turbulence levels with other research will be possible.

The depth profiles for the rms horizontal turbulence levels at position 2 for the plunger and spiller respectively are shown in figures 5.20 and 5.21. The value of the turbulence levels can be clearly seen. For the plunging breaker the maximum levels of turbulence are approximately $0.03v_p$, decaying within the upper enhanced layer to levels of about $0.005v_p$. In the case of the spilling breaker the levels are as expected slightly lower, ranging from $0.01v_p$ to $0.003v_p$. These values are in accordance with the levels reported by Rapp and Melville [56].

The form of the decay of the lower shear-layer is characterised by the value of the gradients, as indicated on the graphs. These were calculated by fitting a power-law relationship to the lower part of the graph, which was identified by inspection. There is a certain amount of uncertainty in this technique and it is only intended that general conclusions to be drawn.

The shear region can be easily identified in all the graphs, beginning at a depth greater than 0.3 and extending to depth of about 0.7, where the noise level is reached. The best-fit lines show gradients of similar magnitudes in both cases in the range -0.35 to -0.49.

The intense patch of vorticity in region 2 was chosen so that a theoretical comparison could be made. If this patch of vorticity is regarded as part of a vortex dipole with an image vortex above the surface, the work of Meleshko and Heijst [44] can be applied. They describe exact solutions of two-dimensional vortex structures, first published by Chaplygin which concludes that the horizontal velocity decays as $1/d^2$ in the region outside the vortex. It could be expected that the decay of velocity in the region below the very intense vortical patch pro-

duced in region 2 of this study, may show a similar relation. This would therefore indicate that this strong vortex motion was an important factor in driving the turbulence below.

The gradients measured imply that u_{rms} decays as $1/d^n$ where n is in the range 2.04 to 2.85. There is relatively good agreement with the $1/d^2$ result, reflecting the strong two-dimensionality of the vorticity in this region. The more inconsistent results could imply some evolving three-dimensionality. This links up with the observation in the previous section, that there were differences in the decay within the lower region at position 2 and 3. Further differences might be expected at the other positions where the turbulence mechanism is again different. For instance many researchers have reported a reversion to law-of-the-wall behaviour at larger depths under breaking waves. The decay of the lower region in the case of the spiller is less well defined, which is not surprising as the turbulence does not occur in distinct, isolated patches as is the case for the plunger. Instead, the turbulence is spread more evenly across the region, so a depth profile calculated from the whole of the velocity field may contain a mixture of different types of motion (i.e some of the structures may be more two-dimensional than others).

5.3.6 Discussion of noise levels and turbulence

So far the noise levels have not been discussed in depth. It has been assumed that when the noise levels are reached that this corresponds to a nominal zero value of the turbulence. The origin and implications of the noise level have not been explained.

Foremost, the noise represents the random PIV error in the experiment. It has contributions due to the error in peak detection in the correlation plane and velocity gradients within the interrogation region. It is also has contributions from systematic errors that may arise from the technique used to extract the
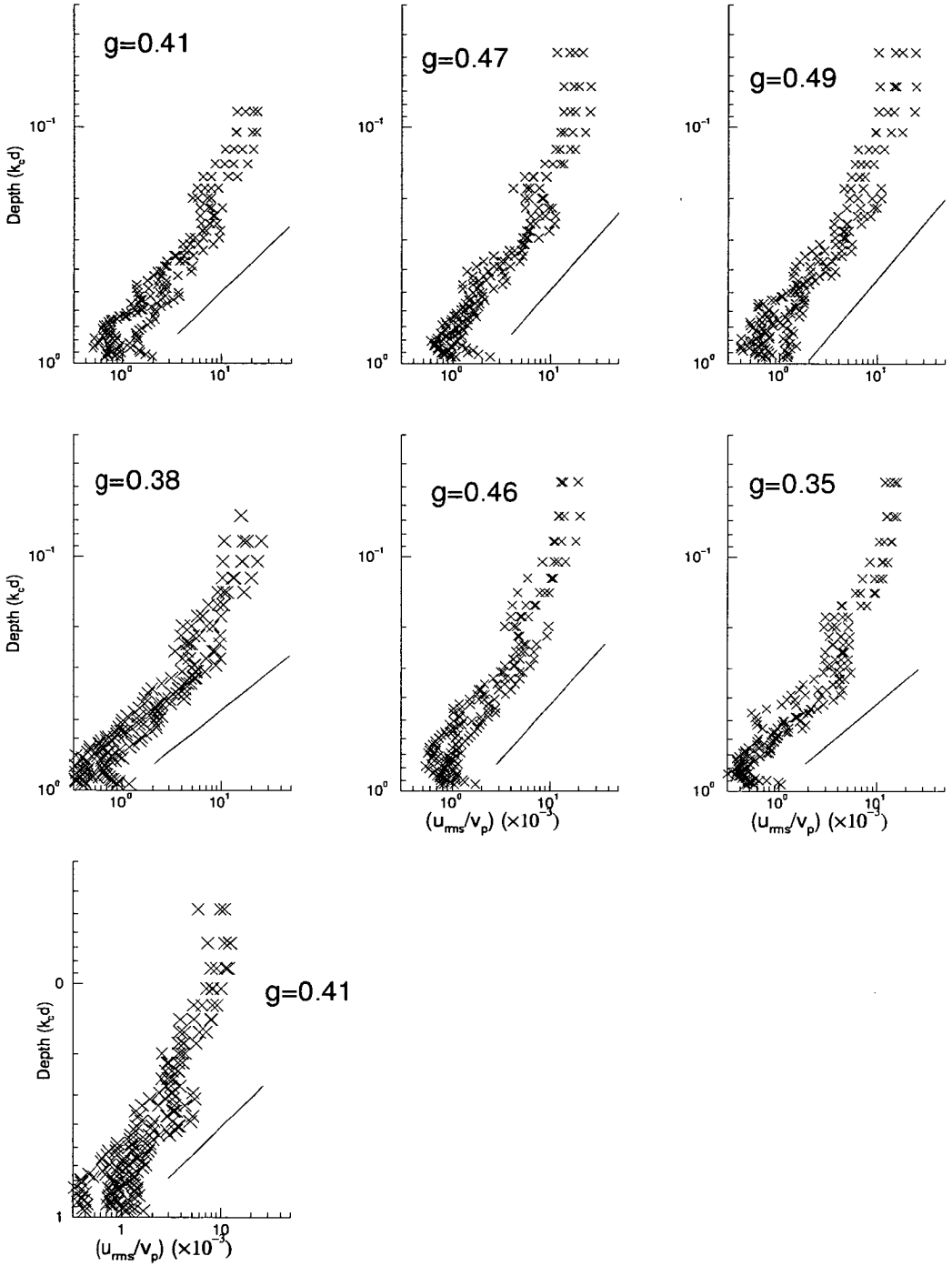
Figure 5.20: Turbulent horizontal velocity profiles for four repeats of sequences captured 1.7-6.2s after breaking of plunger at 0.75s intervals.
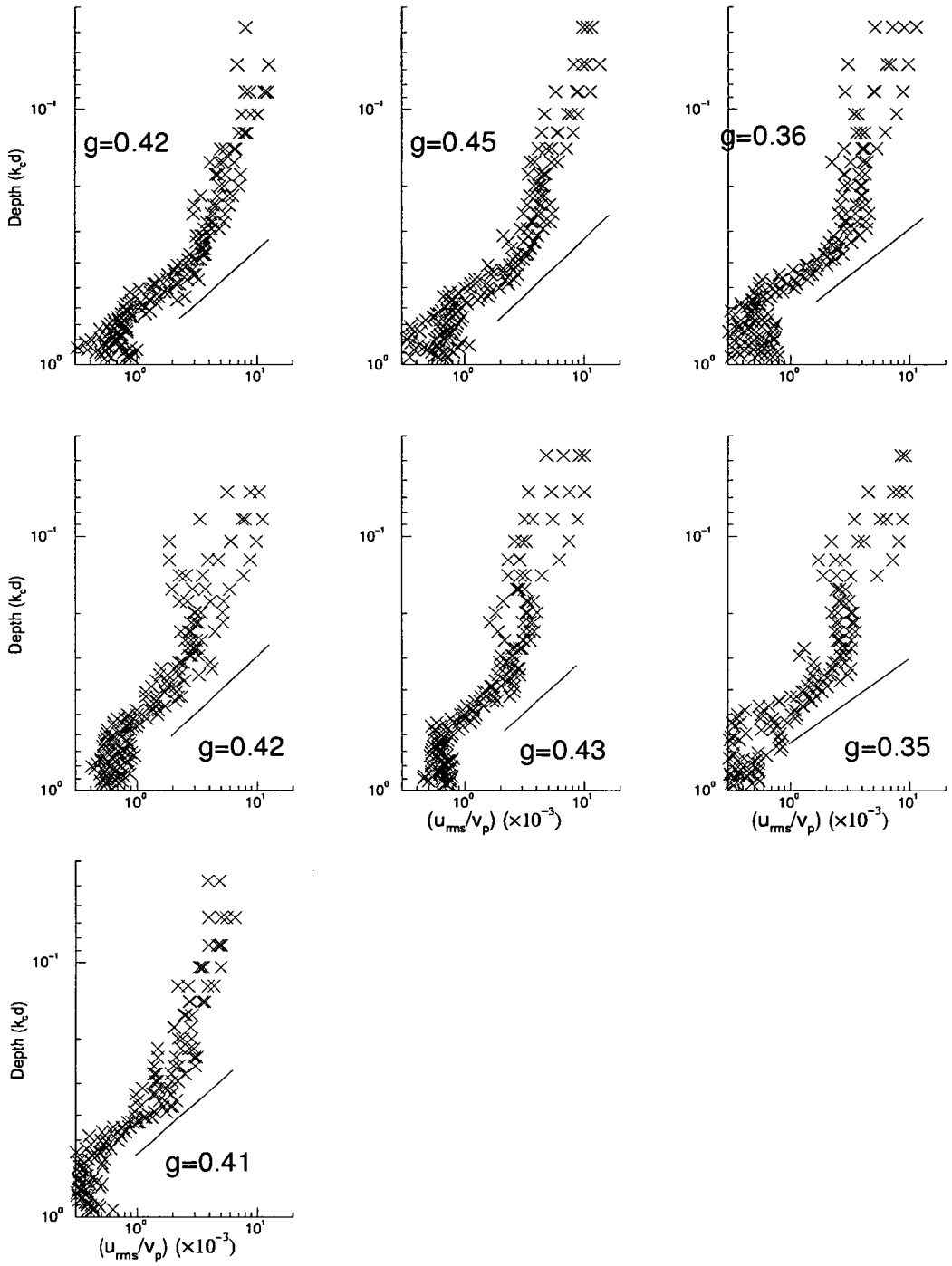
Figure 5.21: Turbulent horizontal velocity profiles for four repeats of sequences captured 1.7-6.2s after breaking of spiller at 0.75s intervals.

turbulent velocities. For instance if the averaging technique does not remove all the mean flow, then this will be included in the background noise level. Also there may be an incorrect estimation of what the value of the mean-flow component might be at the bottom of the velocity field because the local average used near the bottom does not correctly represent the mean-flow at a particular point.

The error is not constant between repeats of the experiment at the same or different positions. There are variant parameters such as seeding density that cause the error to fluctuate, also at different experimental positions the absolute value of the error will change if the distance to the flow field is different.

On inspection of the turbulent velocity depth profiles the rms noise can be estimated as being of the order of 10% of the rms turbulence level in the near-surface layer of the flow, this is approximately 1% in the mean-square values. As an indicator of the relative accuracy of this technique, the error can be compared to errors of approximately 10% in the mean-square turbulence levels that are quoted from LDA experiments [56].

The existence of the rms error also has a profound affect on the form of the depth profiles themselves. If the fluctuating velocity component is expressed as

$$u' = u'_t + u'_n \tag{5.1}$$

where u'_t and u'_n are the turbulent and noise contributions to the fluctuation then the rms fluctuation, calculated by summing along a horizontal line of vectors, is given by

$$u'^2 = u'^2_t + u'^{\,2}_n \tag{5.2}$$

The cross term of $u'_t u'_n$ is assumed to be negligible because any correlation between these two terms is week. Therefore every rms turbulence value should have a constant contribution of $u'^{\,2}_n$. In this analysis the noise could have been subtracted

117

but was not for specific reasons.

Firstly, the exact value of the noise is not known, because the value that comes out of the depth profiles (as quoted above) seems sensible but may have non-noise contributions that are not constant throughout the fluid. Secondly, problems would be encountered if the noise value was subtracted, leaving zero or near-zero values which are difficult to display on log-log graphs.

The essential effect will be that the gradient values measured in the previous section might be larger than the true values. Figure 5.22 shows the comparison between the rms turbulent velocity depth profiles if a noise value of $0.001v_p^2$ is subtracted.

The gradient of the two lines within the box marked on the graph are -0.3 for the graph with the estimated noise removed, and -0.36 for the original graph. This is a significant but not crucial difference. It has the effect of changing the $1/r^n$ power-law from $n = 2.8$ to $n = 3.3$ in this particular case.

5.4 Temporal decay of turbulence

The large dataset can be used to investigate the decay of the total turbulence throughout the whole breaking region for each wave. There are some assumptions that are made in order to enable this relation to be calculated.

Since the total turbulence is calculated by summing the individual turbulence levels over the each experimental position for a particular time, it must be assumed that there is no net flow in or out of each region. While this is unlikely to be strictly true, it should be a of little significance because the most intense turbulence occurs in regions 2 and 3 which were chosen specifically so that the turbulent patch remained within the field of view.

The second assumption is due to the fact that the regions of study overlap
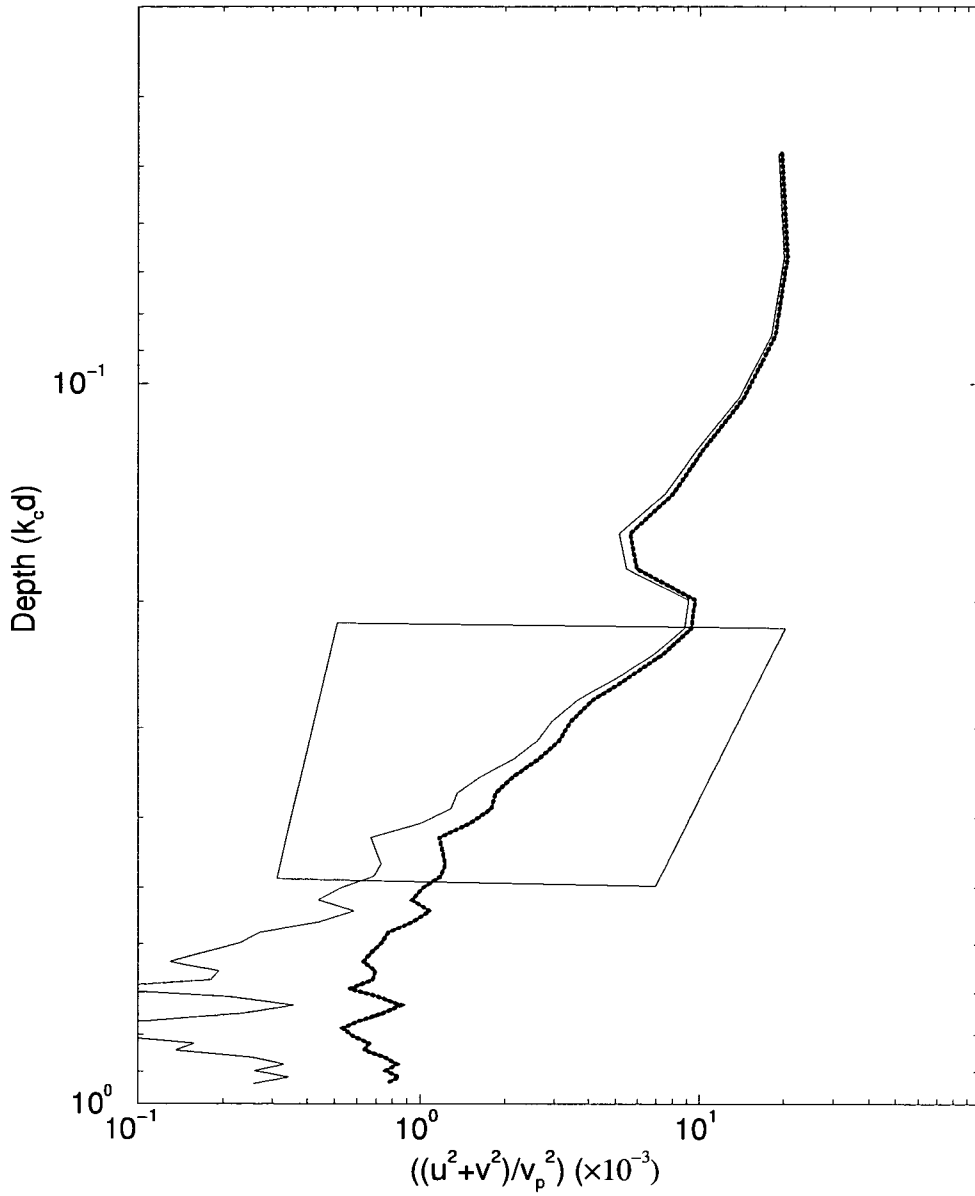
Figure 5.22: A comparison of a depth profiles from position 2 with (solid line) and without (dotted line) estimated noise removed.

slightly. Therefore the contribution to the total turbulence is multiply counted in some cases, which will manifest itself as a systematic shift of the graph, and should not affect the conclusions.

Figure 5.23 shows the decay of the mean-square turbulence levels per unit mass, normalised with v_p^2, plotted against the reciprocal of time. Both graphs show good straight-line fits to the data points, although neither appear to go through the origin. This again relates to the noise levels discussed in the previous section, with the offset being due to the rms noise level and the other error contributions. The intercept on the vertical axis is $0.015v_p^2$ for the spiller and $0.15v_p^2$ for the plunger (this is ignoring the erroneous point on the far left). These values are approximately 5% and 30% of typical turbulence levels in this graph, suggesting that there is a significant systematic error due to overlapping of experimental regions in the case of the plunger but not in the case of the spiller.

A turbulent kinetic energy decay proportional to t^{-1} is consistent with the results of Rapp and Melville [56]. The gradients of the graphs are 0.9348 and 0.6988 for the plunger and spiller respectively.

Over the period of time for which this data was recorded the turbulent energy levels fall by about a factor of 2 in the case of the plunger and in excess of a factor of 3 for the spiller.

5.5 Wavenumber spectra

The wavenumber spectra in turbulence represents the cascade of eddies from the largest to smallest sizes, which is a fundamental aspect of turbulence. It is also very important in the measurement of dissipation rates, a quantity that is important in the study of the upper region of the ocean.

Many researchers have used various different methods to characterise the spec-
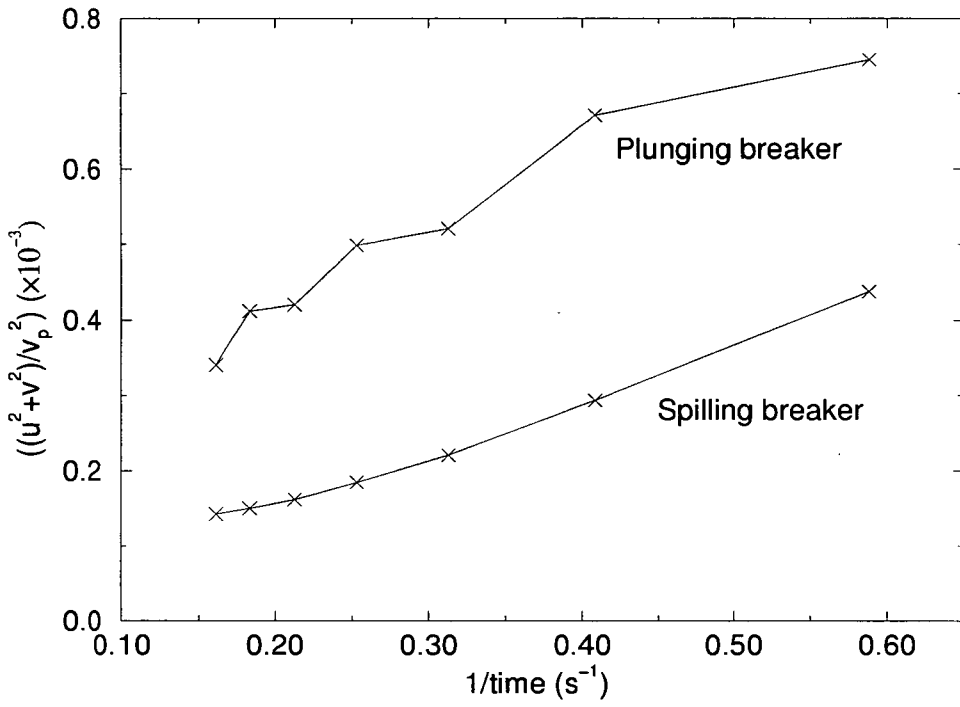
Figure 5.23: Total turbulent energy against time for the spilling and plunging breakers.

tra and hence measure dissipation rates. Mainly temporal (point) measurements have been made using techniques such as LDA, which have been converted to the spatial domain using Taylors frozen turbulence hypothesis [26].

In this study the wavenumber spectra was calculated directly from the PIV data. The minimum physical size of a spatial fluctuation that can be unambiguously measured using PIV is approximately two vector spacings in width. Therefore the spectra calculated was generally noisy above spatial frequencies corresponding to two vectors in separation. It was therefore decided that all spectral information could be cut off at this two-vector wide spatial frequency.

There are a number of reasons for studying the spectra with respect to the application of post-breaking turbulence. Primarily we are looking for evidence of a Kolmorgorv spectrum in which the cascade decays as $k^{-5/3}$. This follows from the expression for the energy spectrum

$$E(k) = \alpha \epsilon^{2/3} k^{-5/3} \qquad (5.3)$$

Where α is a constant whose value has been found experimentally to be approximately 1.5 and ϵ is the dissipation rate. This is derived in most standard test books [63].

The -5/3 law has been found experimentally for breaking wave turbulence by many researchers e.g [20]. This represents the cascade spectrum in the inertial subrange for isotropic turbulence in highly convected flow. There is also evidence for cascade spectra with slopes greater than -5/3. Thornton [66] found slopes of up to -2 or -3 at high frequencies suggesting that a -2 gradient corresponds to weekly convected flow. A gradient of -3 was also found by Battjes [8] and Lemmin [37]. Battjes [8] found the -3 gradient for high frequencies when investigating the near breaking region of a steady breaker while Lemmin [37] investigated turbulence in Lake Ontario directly following meteorological disturbances, finding that a

transition from a -3 gradient to -5/3 occurred. A spectrum with gradient of -3 within the inertial subrange is indicative of two-dimensional turbulence (see Frisch [24]), while a gradient of -3 in the low frequency regime of the spectrum may be expected anyway due to the irrotational wave components of the flow.

The turbulence studied here is in the early stages of decay and was produced by an essentially two-dimensional process. Therefore, it may be expected that some evidence of two-dimensional turbulence may be found in the spectra displayed in this section. The main objectives were to show the evolution of the wavenumber spectra and relate it to the physical event of the breaking process and the associated motions. This can also be related to theoretical and experimental results suggested by other researchers.

5.5.1 Discussion of wavenumber spectra

Not all spectra for these experiments displayed high quality information, in some cases noise levels appeared to be high and no useful information could be extracted. In the case of the plunging breaker the majority of the spectra showed good agreement with the -5/3 gradient when plotted on a log-log graph, particularly for the higher wavenumber part of the spectrum. The low wavenumber section of the spectra often shows a steeper gradient in the region of -2.5 to -3.

Example spectra for all positions and both waves are shown in figures 5.24 - 5.31, for selected times. The best-fit line to the data is shown on each graph. For the plunger the best-fit gradient was maximum in positions 1, 2 and 3 and was considerably less at position 4. Position 2 showed gradients quite consistently in the range -1.7 to -2, while in positions 1 and 3 the gradients were slightly less than this, in the range -1.6 to -1.7. The gradients at the final position were substantially lower, generally being in the range -1.4 to -1.6.

In the case of the spilling breaker, position 2 showed the maximum slopes

of the spectra, in the range -1.7 to -2, while the spectra at the remaining three positions showed gradients below this, in the range -1.4 to -1.7. All gradients have errors of approximately 0.07 a percentage error of 4 - 5%.

The initial conclusion from these gradients is that the trends shown are as expected but the actual values of the gradients are lower than would have been expected. If the magnitude of the gradient is regarded as an indication of the isotropy then it is consistent that the greatest values occur at position 2 where the most strongly two-dimensional vortical structures exist. The less two-dimensional structures occur due to the more chaotic splash-ups in the subsequent regions.

There are a number of spectra that show a characteristic shape as displayed by the first graph in figure 5.24 or the first graph in figure 5.28. These show a broad peak in the spectrum at wavenumbers between approximately 40 and $150m^{-1}$. The most likely cause of these peaks are the presence of non-breaking wave components, consisting of a mixture of harmonics of the input frequencies, that travel through the region after breaking. This explains why the peaks are very short-lived, disappearing from one instant to the next.

The decrease in gradient can be seen as an increase in isotropy and an increase in the rate of transfer of energy towards the higher frequencies, something suggested by Thornton [66]. The smaller scales produced by the spiller and the splash-up's of the plunger would dissipate much more rapidly than the more coherent two-dimensional vortices that are present in the flow. Here, the gradient of the spectra are less steep in the spilling case and for the furthest downstream position of the plunger.

The spectral slopes have been found to be lower than expected in other experimental work. For instance George *et al* [26] found the average slope of the spectra to be -1.25, citing entrained air bubbles as a possible reason. It may
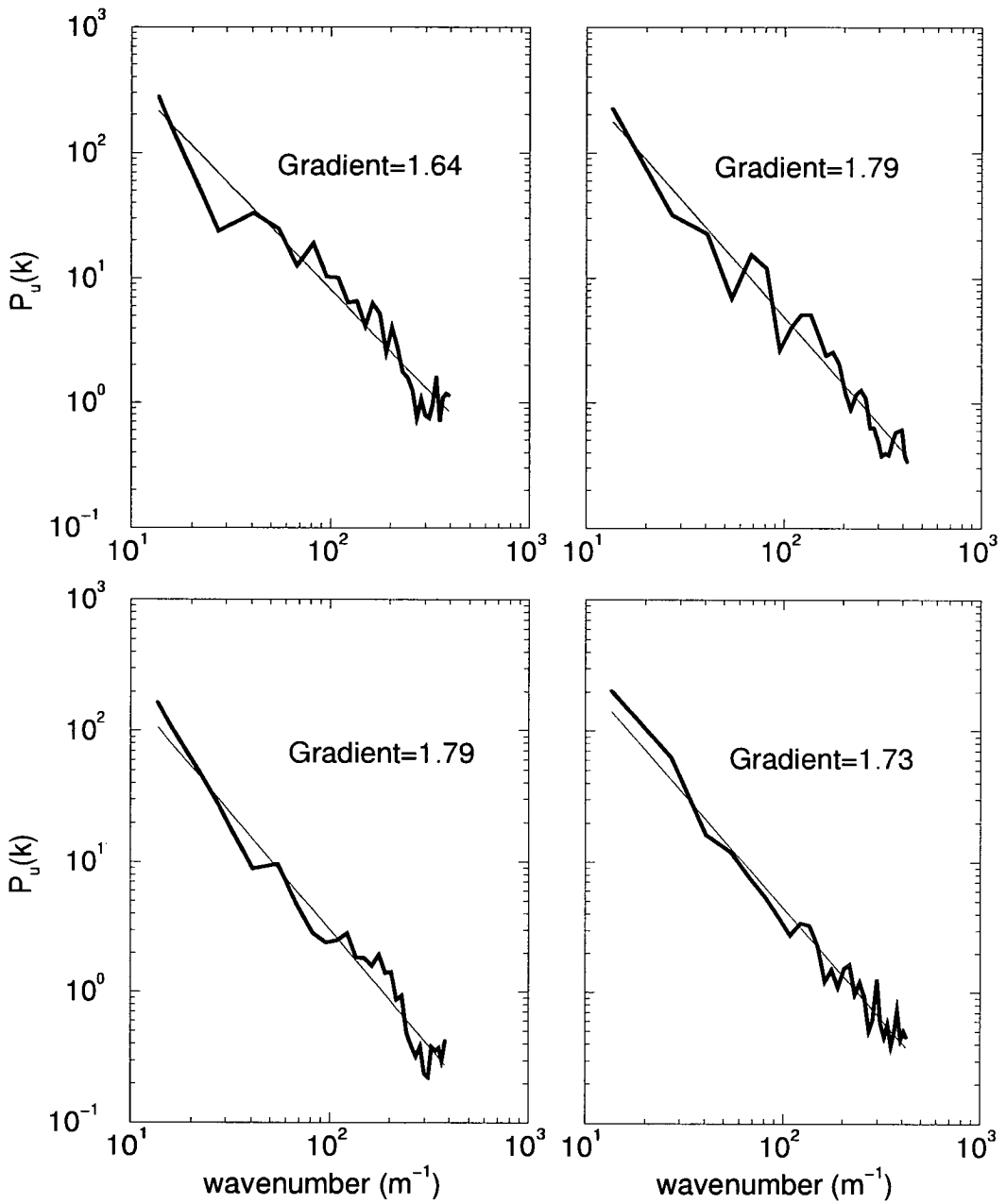
Figure 5.24: Selected power spectra for plunging breaker at position 1. Top left is earliest, bottom right latest.
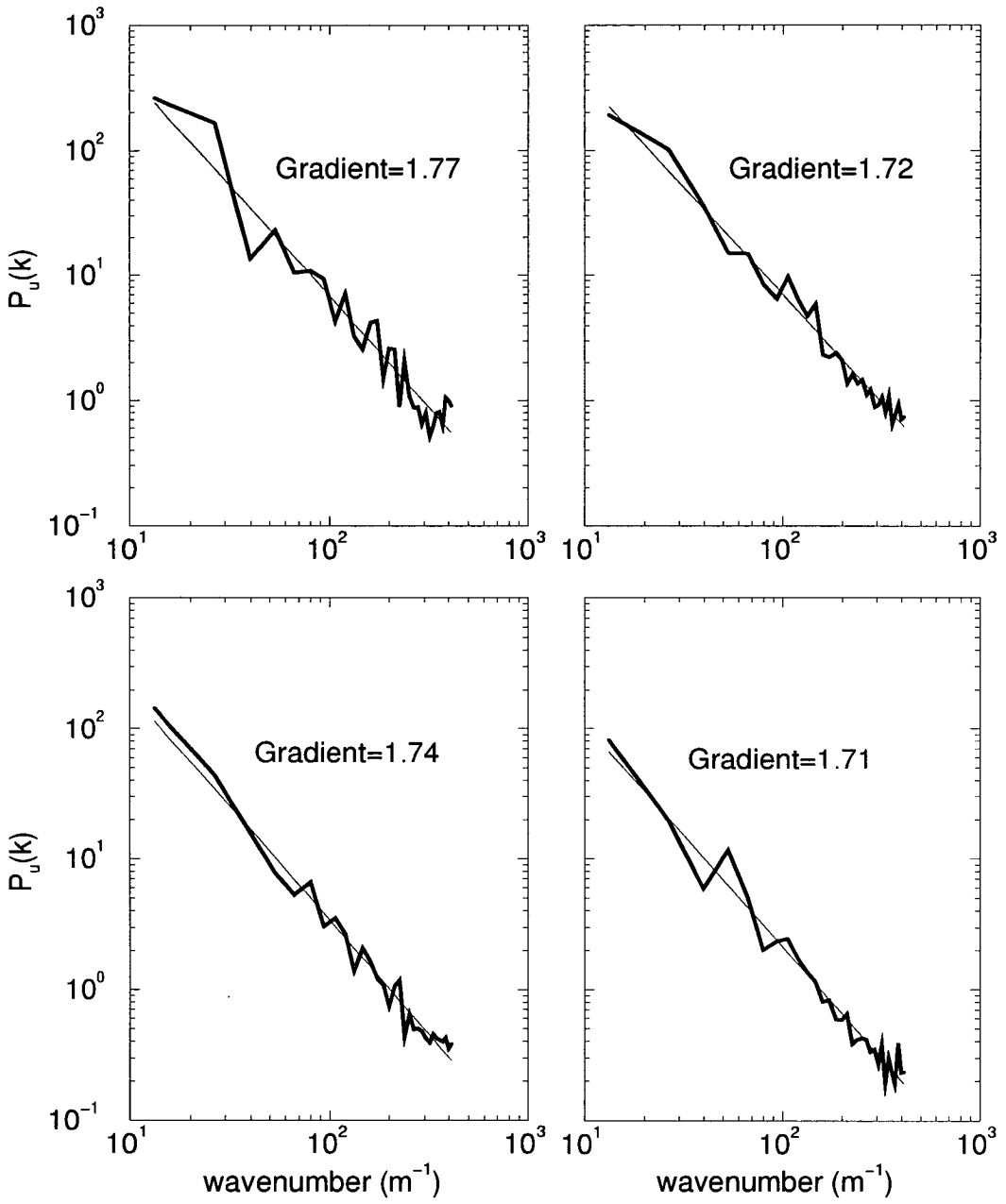
Figure 5.25: Selected power spectra for plunging breaker at position 2. Top left is earliest, bottom right latest.
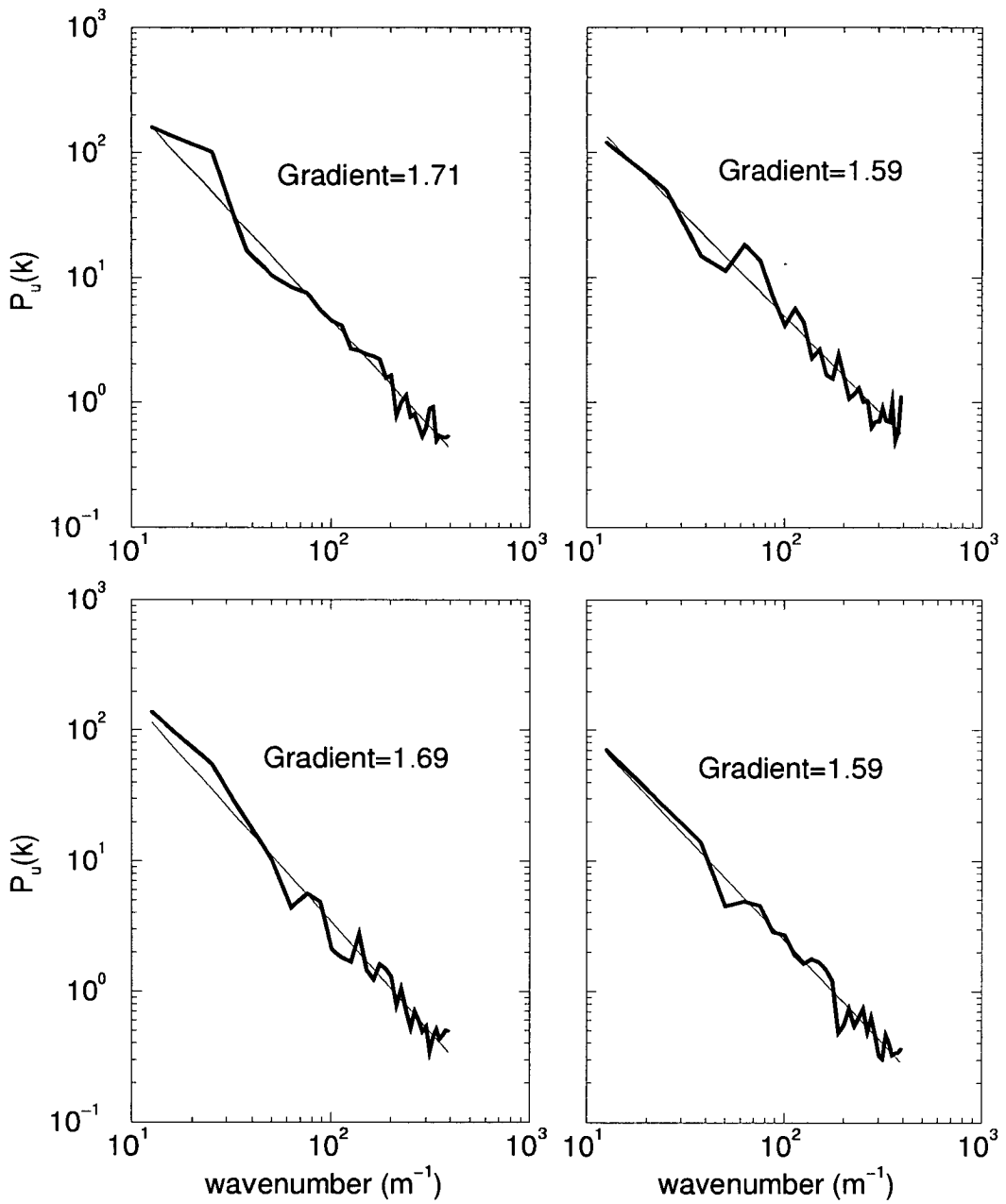
Figure 5.26: Selected power spectra for plunging breaker at position 3. Top left is earliest, bottom right latest.
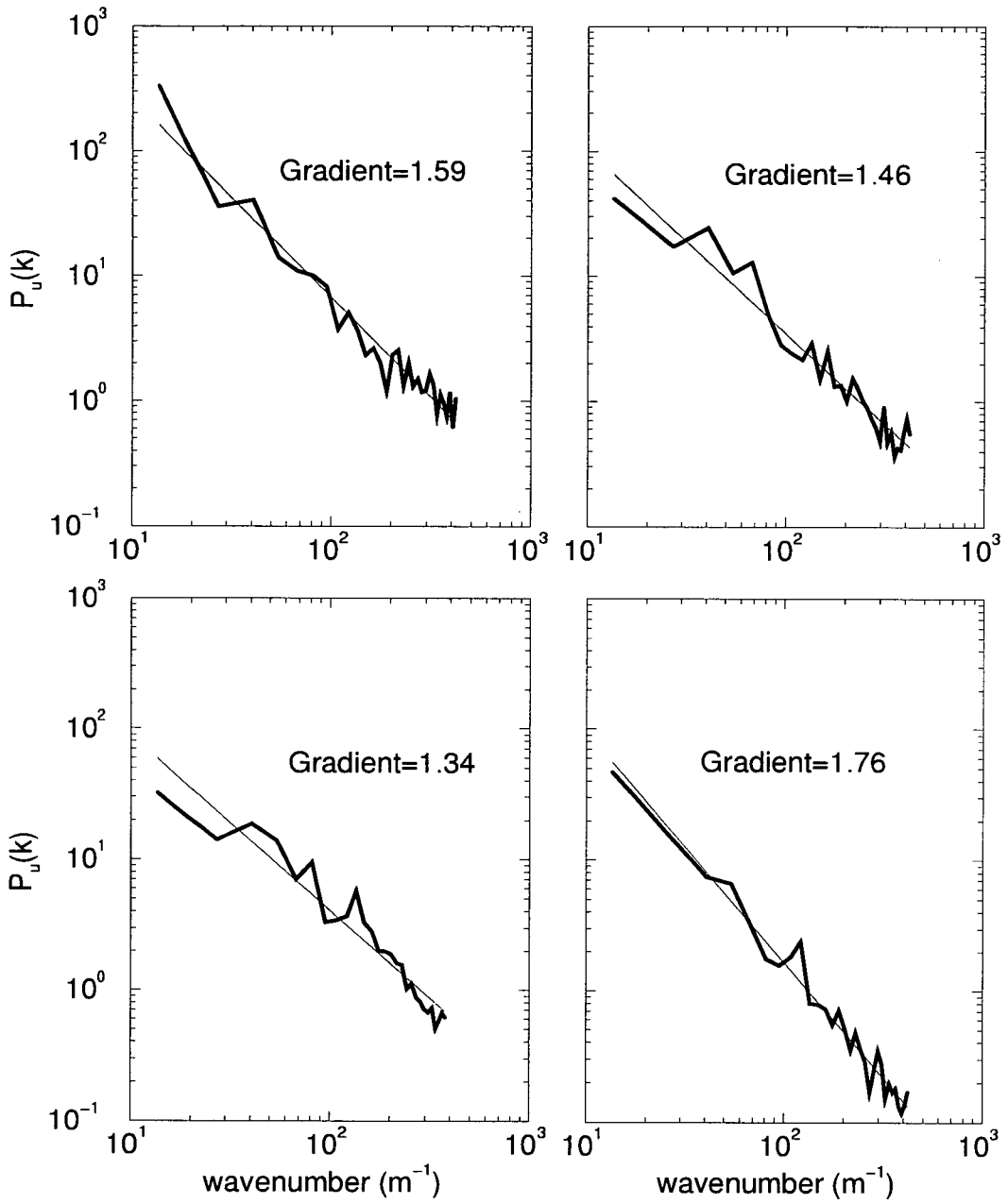
Figure 5.27: Selected power spectra for plunging breaker at position 4. Top left is earliest, bottom right latest.
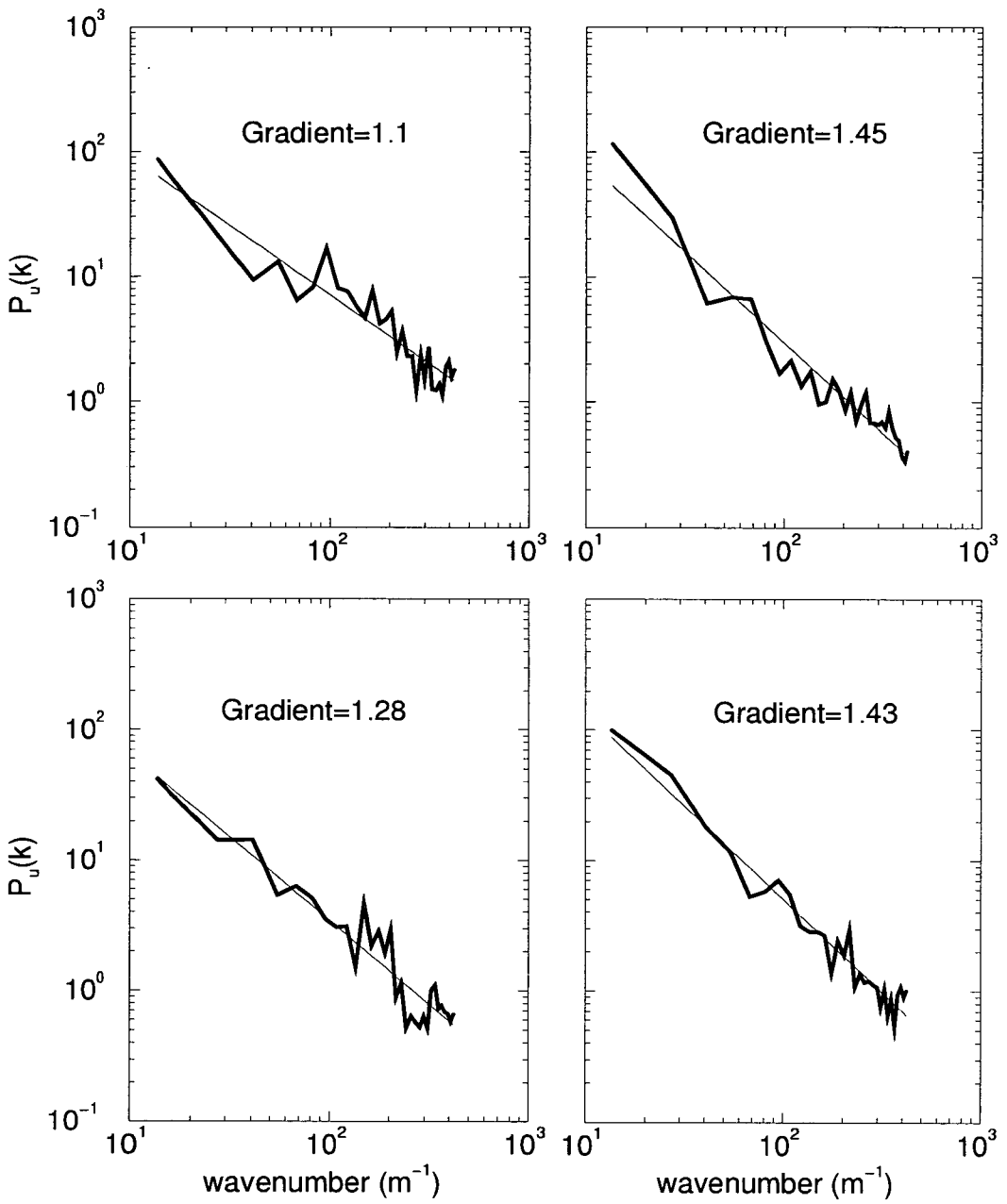
Figure 5.28: Selected power spectra for spilling breaker at position 1. Top left is earliest, bottom right latest.
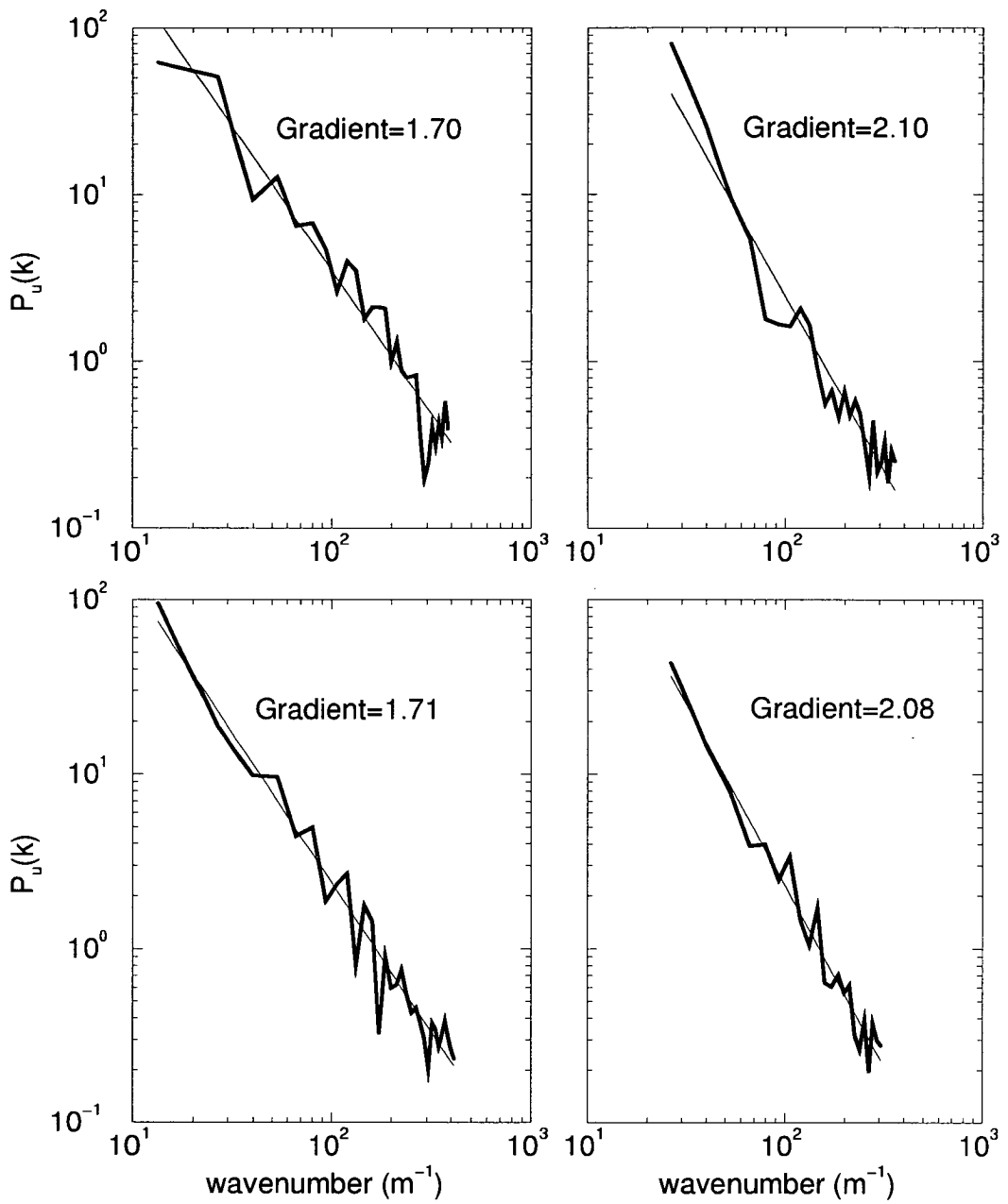
Figure 5.29: Selected power spectra for spilling breaker at position 2. Top left is earliest, bottom right latest.
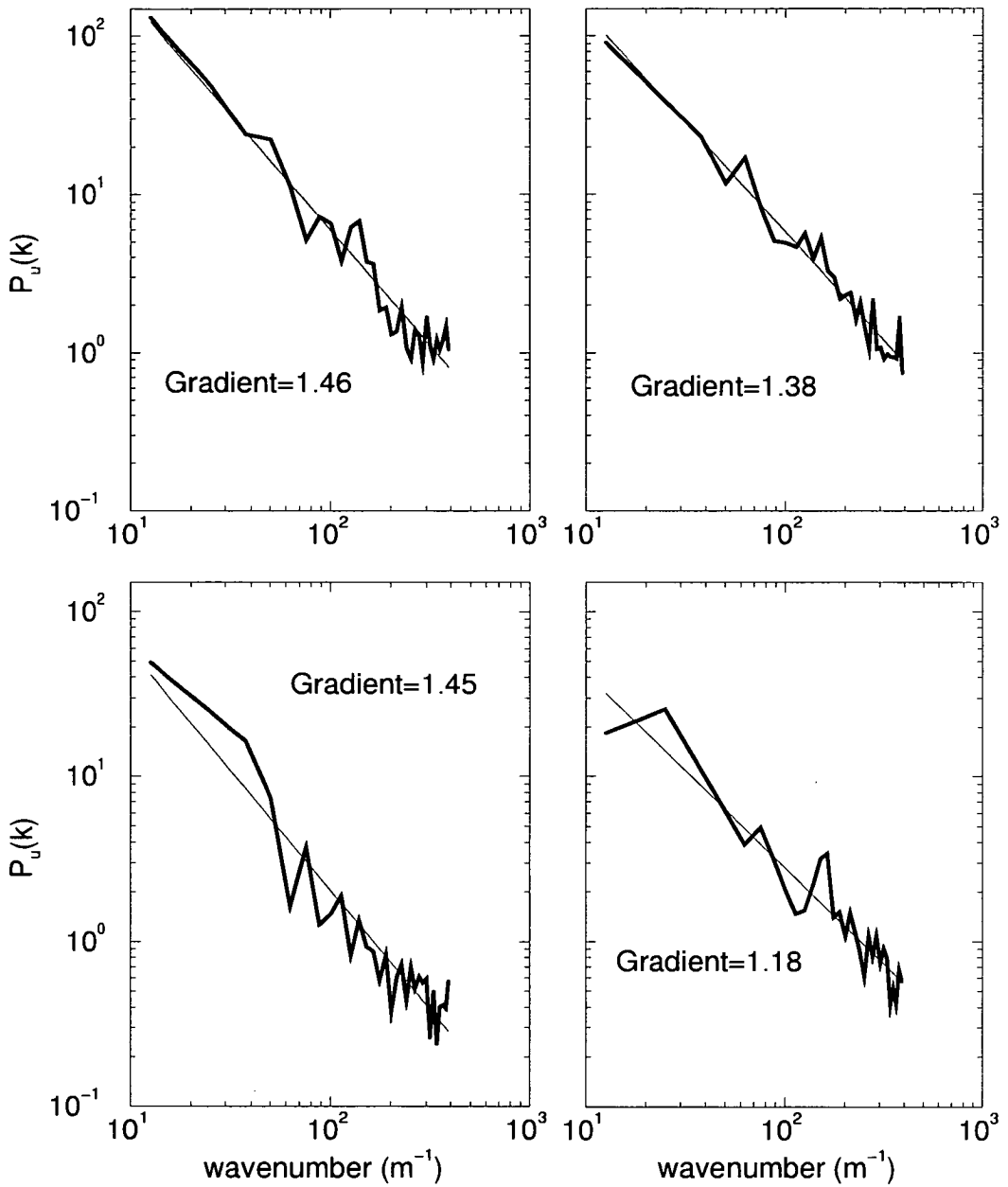
Figure 5.30: Selected power spectra for spilling breaker at position 3. Top left is earliest, bottom right latest.
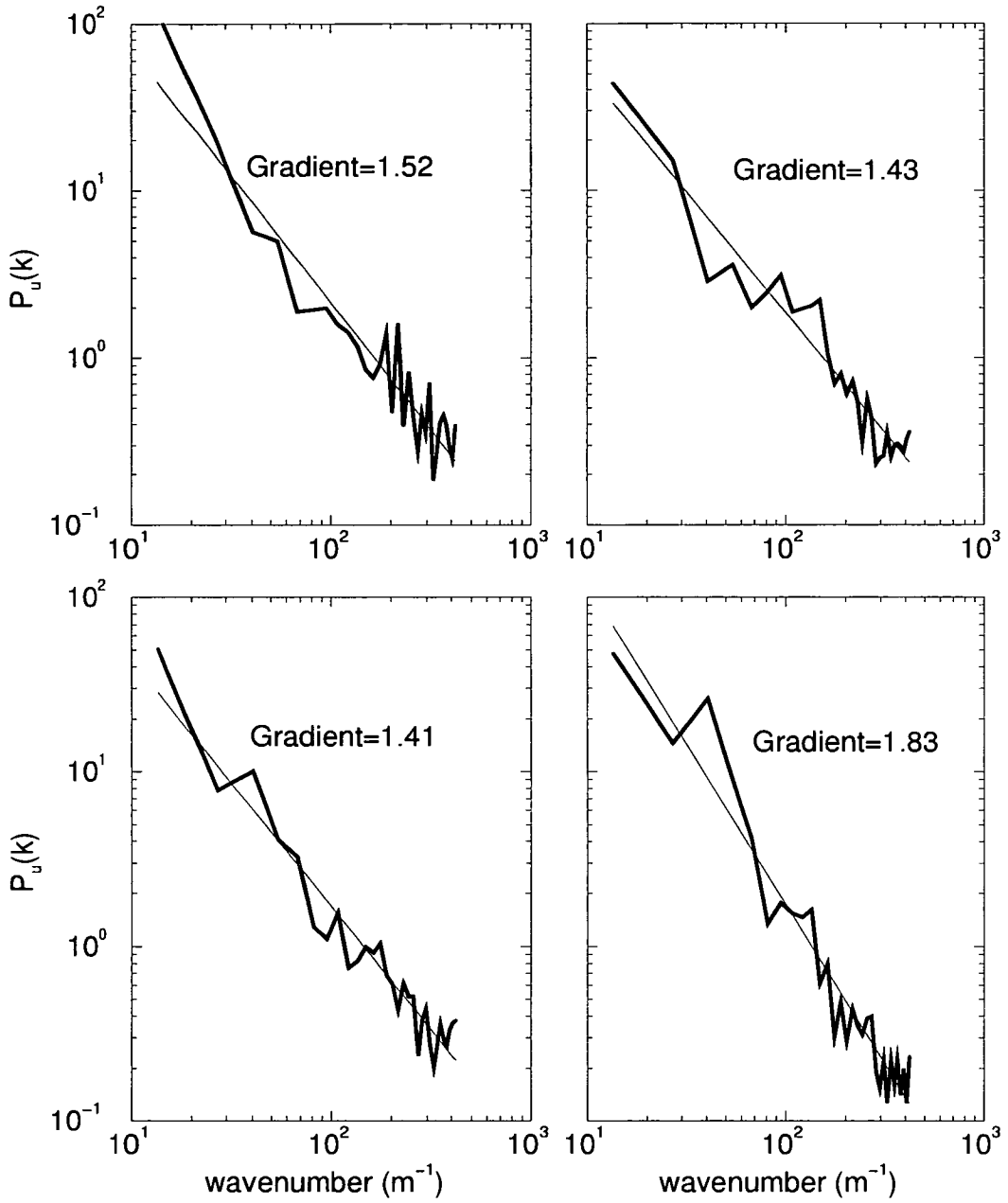
Figure 5.31: Selected power spectra for spilling breaker at position 4. Top left is earliest, bottom right latest.

therefore be that lower values of the gradients are to be expected.

5.6   Conclusions

In this chapter the turbulence has been characterised as a mixed-layer and a shear layer beneath. The decay over time of the turbulent kinetic energy was shown and fitted to a t^{-1} relationship. The wavenumber spectra has shown a good comparison with theory and the results from other research.

Chapter 6

Conclusions

6.1 Primary conclusions

The conclusions to the work contained in this thesis can be made with reference to the original aims that were set out in chapter 1.

- With the use of image shifting and a high resolution CCD camera the flow was successfully measured in the post-breaking region. The frame-grabbing hardware that was used in conjunction with the camera was upgraded and software written in order to allow a sequence of images to be obtained. This was a non-trivial achievement because of the large size of the images and the cost and limitations of memory.

  The time-scale for this sequence was 4.45s, during which time the flow velocities decayed significantly. The degree of shift that was applied to the flow could not be changed during an acquisition sequence, making the choice of it's value and the value of the other PIV parameters important. This fine-tuning of the system was a fundamental aspect of the successful measurement of the flow.

- The next question that was addressed was whether it is possible to measure turbulent quantities accurately using this PIV system. The flow generated

was a complicated example of turbulence, being not only inhomogeneous but a mixture of true random turbulence and non-turbulent wave components.

The wave-number spectra that was displayed showed good agreement with similar work on this subject and with the Kolmogorov $-5/3$ law. This agreement and the fact that the spectra were generally relatively smooth, provides evidence to support the accurate measurement of the turbulence.

A technique was developed to decompose the flow-field into non-turbulent motion, turbulent motion and high frequency noise. Whilst acknowledging the limitations and inaccuracies of the separation technique it was demonstrated to be a useful approach to solving this problem. Certainly in comparison with techniques used by researchers in similar work it was thought to be adequate. This was supported by the characteristics shown by depth profiles and the temporal decay of turbulence in comparison with related theory.

- The final objective could be regarded as the most important to the study. This was the aim to obtain an insight into the dynamics of the breaking process using the full field information obtained in the post-breaking region. Four different positions were studied covering the whole of the turbulent region. Two fundamentally different waves were studied, one being an extreme plunging breaker and the other a spilling breaker.

  1. Beginning from an extensive visualisation of the velocity and vorticity field the differences between the two flows and the individual characteristics were noted and highlighted. The large, extensive set of vorticity maps show the flow structures clearly and display the early

stages of evolution. Along with video information of the flow, a qualitative description of the two breakers were developed and related to the existing knowledge of the dynamics of the breaking process.

2. An estimation of the circulation in the region where the main vorticity exists is made for the plunging breaker. The variation over time is measured and extrapolated back to the instant of breaking. This provided an estimation of the total circulation in this region just after breaking. An estimate for the circulation around a point outside the flow just before the wave breaks was also made and the two values related. The value of 32% of the original circulation was calculated. This value is of the expected order of magnitude and gives a reasonable comparison value for more accurate calculations that may follow.

3. The turbulent energy and horizontal velocity profiles reveal important characteristics of the turbulent region. Two distinct regions were found that seemed to exist consistently in all but the furthest region from breaking. These were related to observations from the vorticity maps and proposed to be a near surface mixing region with a shear-layer beneath.

4. The temporal decay of turbulence showed that the decay followed a $1/t$ relationship.

5. The spectra, as stated, show the Kolmogorov law but also can be used to highlight an important property of this type of turbulence. The spectra from the spilling breaker showed a generally smaller gradient than for the plunger. For the plunger, further away from the position at which the crest initially hits the water, smaller gradients were found. The flatness of the gradient was suggested to correspond to increased

136

isotropy in the flow, which implies that spilling breakers have a more three-dimensional nature than plungers. This was stated to agree with observations from video and from vorticity maps.

6.2 Recommendation for future work

6.2.1 PIV

PIV is a measurement technique that has developed rapidly over the period of this research, yet there is still much scope for further improvement. Higher resolution cameras, faster computers and larger memory are all areas in which the systems will inevitably improve.

Larger CCD arrays will further improve the versatility of the technique, allowing larger regions to be studied in increased detail. This would be useless without the additional development of faster computer systems and hardware such as frame-grabbers that can deal with the large images. At present the size of images produced by the CCD camera used in this study are cumbersome.

Developments in this area will enable new CCD technology such as faster frame rates and developments in DPIV itself such as the use of cross-correlation, to be accommodated. The implementation of cross-correlation systems will be a big step forward, image shifting and the associated errors will no longer be a problem.

Increased computer capacity allowing more images to be acquired sequentially will result in more information on evolving flows to be extracted.

Recent advances in PIV systems at Edinburgh have involved the use of a four camera cross-correlation system enabling the measurement of accelerations and out-of-plane velocities [17]. Further developments in the location of the displacement-correlation peak have also improved the resolution of small scale

structures. Westerweel [70] reports accurate measurement of wavenumbers nearly an order of magnitude higher than with the previous peak-locating technique. Improvements of this nature would result in a significant increase in the inertial subrange of scales displayed in the spectra in chapter 5. This would accordingly increase the accuracy and quality of the spectra.

The developments outlined here will therefore allow a significant increase in the dynamic range of velocities that can be measured, with an associated increase in spatial resolution, while still enabling a large area to be studied.

6.2.2   Water wave studies

The future study of water waves using PIV follows from the developments that should be made with the PIV system. An extended sequence of PIV images covering a longer time period and at higher sampling frequencies would yield more complete information on the flow. At the moment only the flow near the breaking time has been studied. The measurement of accelerations and hence forces exerted by breaking waves would prove useful to offshore engineers. The existence of an evolving out-of-plane velocity component has been discussed in this work and would benefit from further investigation with the newly developed system.

The present study concentrated on a single breaking wave. A logical development would be to extend this to a continuous random train of breakers, thus simulating the intermittency of the ocean.

The study could be extended to cover breaking waves on beaches, indeed preliminary studies have already been made by the author in this area. The flume used for this study has a facility for a steep beach to be used.

In addition to extending the scope of the experimentation, there is plenty of room for further analysis on the existing data that was captured. Only limited

analysis was performed covering only a few of the possible turbulent characteristics of the flow. Other quantities such as Reynolds stresses, turbulent length scales and dissipation rates could be calculated.

Bibliography

[1] R. J. Adrian. Scattering particle characteristics and their effect on pulsed laser measurement of fluid flow. *Applied Optics*, 23:1690–1691, 1984.

[2] R. J. Adrian. Image shifting technique to resolve directional ambiguity in double pulsed velocimetry. *Applied Optics*, 25:3855–3858, 1986.

[3] R. J. Adrian. Particle-imaging techniques for experimental fluid mechanics. *Ann. Rev. Fluid Mech*, 25:3855–3858, 1986.

[4] A. D. Arnott, T. P. Dewhirst, J. Pullen, and C. A. Greated. Underwater ccd cameras for piv flow mapping. *Optics and Laser Technology*, 29:45–50, 1997.

[5] M. P. Arroya and C. A. Greated. A three-dimensional particle image velocimetry system and its application to the measurement of accoustic streaming. In *Proc. Euromech Colloquium 279*, The Netherlands, December 1992.

[6] M. L. Banner and D. H. Peregrine. Wave breaking in deep water. *Ann. Rev. Fluid Mech*, 2:373–, 1992.

[7] T. C. D. Barnes, M. Brocchini, D. H. Peregrine, and P. K. Stansby. Modelling post-wave breaking turbulence and vorticity. In *Proc. 25th Intl. Conf. Coastal Eng.*, Orlando, Florida, USA, September 1996.

[8] J. A. Battjes and T. Sakai. Velocity field in a steady breaker. *J. Fluid Mech.*, 111:421–437, 1981.

[9] A. Yu. Benilov and B. N. Filyushkin. Application of methods of linear filtration to an analysis of fluctuations in the surface layer of the sea. *Atmos. Oceanic Phys. USSR (Eng. Transl.)*, 6:477–482, 1970.

[10] P. Bonmarin. Geometrical properties of breaking waves. *J. Fluid Mech.*, 209:405–433, 1989.

[11] R. N. Bracewell. *The fourier transform and it's applications.* McGraw-Hill International Editions, 1986.

[12] T. Bruce. Private communication.

[13] A. Chopra. *The volume of fluid technique for the numerical simulation of water waves.* PhD thesis, The University of Edinburgh, 1997.

[14] A. Chopra and C. A. Greated. Development and validation of the volume of fluid technique for water wave dynamics. In *Proc. 6th Intl. Symp. Comput. Fluid Dyn.*, volume 1, pages 212–217, Lake Tahoe, Nevada, USA, September 1995.

[15] D. Dabiri and M. Gharib. Experimental investigation of the vorticity generation within a spilling water wave. *J. Fluid Mech.*, 330:113–139, 1997.

[16] C. E. Damm. *Study of turbulence using PIV.* PhD thesis, The University of Edinburgh, 1996.

[17] T. P. Dewhirst. Private communication.

[18] D. G. Dommermuth, D. K. P. Yue, W. M. Lin, R. J. Rapp, E. S. Chan, and W. K. Melville. Deep-water plunging breakers: a comparison between potential theory and experiments. *J. Fluid Mech.*, 189:423–442, 1988.

[19] M. A. Donelan. Whitecaps and momentum transfer. In A. Favre and K. Hasselmann, editors, *Fluxes through the sea surface, wave dynamics and prediction*, pages 273–286. Plenum Press, 1978.

[20] W. M. Drennan, K. K. Kahma, E. A. Terray, M. A. Donelan, and S. A. Kitaigorodskii. Observations of the enhancement of kinetic energy dissipation beneath breaking wind waves. In *UTAM Symp. Breaking Waves*, pages 95–101, Sydney, 1991.

[21] H. C. Earnshaw. *A study of Flow over a Rippled Bed using Particle Image Velocimetry*. PhD thesis, The University of Edinburgh, 1996.

[22] W. A. Easson, C. A. Greated, D. H. Peregrine, and P. K. Stansby. Modelling of breaking waves. Technical report, Report on EPSRC grant., 1997.

[23] D. I. M. Forehand, J. G. B. Byatt-Smith, and C. A. Greated. Numerical prediction of extreme free-surface flows caused by body/fluid interaction. In *Proc. 6th Intl. Symp. Comput. Fluid Dyn.*, volume 1, pages 312–317, Lake Tahoe, Nevada, USA, September 1995.

[24] U. Frisch. *Turbulence*. Cambridge University Press, 1995.

[25] A. E. Gargett. Ocean turbulence. *Ann. Rev. Fluid Mech.*, 21:419–451, 1989.

[26] R. George, R. E. Flick, and R. T. Guza. Observations of turbulence in the surf zone. *J.Geophys. Reseach*, 99:801–810, 1994.

[27] C. H. Gibson. Effects of intermittency on growth inhibition of a red tide dinoflagelate, gonyaulax polyedra stein. *J.Geophys. Reseach*, 100:24841–24846, 1995.

[28] C. Gray. *The Development of Particle Image Velocimetry for Water Wave Studies.* PhD thesis, The University of Edinburgh, 1989.

[29] C. Gray. An analysis of the scanning beam piv illumination system. *J.Phys. Measurement Science and Technology*, 2:717–724, 1991.

[30] D. B. Hann. Private communication.

[31] M. Hattori and T. Aono. Experimental study on turbulence structures under breaking waves. *Coastal Engineering in Japan*, 28:97–116, 1985.

[32] T. R. Haydon and C. A. Greated. The measurement of turbulence using piv. In *Advances in Turbulence*, Lausanne, Switzerland, July 1996.

[33] T. R. Haydon, D. B. Hann, P. Davies, C. A. Greated, and T. C. D. Barnes. Turbulence structures in the surf zone. In *Proc. 25th Intl. Conf. Coastal. Eng.*, Orlando, Florida, USA, September 1996.

[34] E. J. Hopfinger and J. A. Toly. Turbulent mixing across density interfaces. *J. Fluid Mech.*, 70:155–175, 1976.

[35] S. A. Kitaigorodskii, M. A. Donelan, J. L. Lumley, and E. A. Terray. Wave-turbulence interaction in the upper ocean, part 2: Statistical characteristics of wave and turbulent components of the random velocity field in the marine surface layer. *J. Phys. Oceanogr.*, 13:1988–1999, 1983.

[36] M. V. Klein and T. E. Furtak. *Optics.* John Wiley and Sons, Inc., New York, 1986.

[37] U. Lemmin, J. T. Scott, and U. H. Czapski. The development from two-dimensional to three-dimensional turbulence generated by breaking waves. *J.Geophys. Reseach*, 19:3442–3448, 1974.

[38] J. C. Lin and D. Rockwell. Instantaneous structure of breaking waves. *Phys. Fluids*, 6:2877–2879, 1994.

[39] J. C. Lin and D. Rockwell. Evolution of a quasi-steady breaking wave. *J. Fluid Mech.*, 302:29–44, 1995.

[40] M. S. Longuet-Higgins. Parametric solutions for breaking waves. *J. Fluid Mech.*, 121:403–424, 1982.

[41] J. L. Lumley and E. A. Terray. Kinematics of turbulence convected by a random wave field. *J.Phys. Oceanogr*, 13:2000–2007, 1983.

[42] J. Magnaudet and L. Thais. Orbital rotational motion turbulence below laboratory wind water waves. *J. Geophys. Research*, 100:757–771, 1995.

[43] W. D. McComb. *The Physics of Fluid Turbulence*. Oxford University Press, 1990.

[44] V. V. Meleshko and G. J. F. Van Heijst. On chaplygin's investigations of two-dimensional vortex structures in an inviscid flow. *J. Fluid Mech.*, 272:157–182, 1994.

[45] I. G. Morrison. *The Hydrodynamic Performance of an Oscillating Water Column Wave Energy Converter*. PhD thesis, The University of Edinburgh, 1995.

[46] K. Nadaoka, M. Hino, and Y. Koyano. Structure of the turbulent flow field under breaking waves in the surf zone. *J. Fluid Mech.*, 204:359–387, 1989.

[47] K. Nadaoka and T. Kondoh. Laboratory measurements of velocity field structure in the surf zone by ldv. *Coastal Eng. Jpn.*, 25:125–145, 1982.

[48] A. L. New. A class of elliptical free-surface flows. *J. Fluid Mech.*, 130:219–239, 1983.

[49] A. Okayasu, T. Shibayama, and N. Mimura. Velocity field under plunging waves. In *Proc. Coastal Engineering Conf.*, volume 1, pages 662–663, 1986.

[50] M. Perlin, J. He, and L. P. Bernal. An experimental study of deep water plunging breakers. *Phys. Fluids*, 8:2365–2374, 1996.

[51] K. Prasad, R. J. Adrian, C. C. Landreth, and P. W. Offutt. Effect of resolution on the speed and accuracy of particle image velocimetry interrogation. *Exp. Fluids*, 13:105–116, 1992.

[52] P. A. Quinn. *Breaking Waves on Beaches*. PhD thesis, The University of Edinburgh, 1995.

[53] P. A. Quinn, T. C. D. Barnes, S. T. Lloyd, C. A. Greated, and D. H. Peregrine. Velocity measurements of post-breaking turbulence. In *Proc. of Coastal Dynamics Conf.*, volume 1, Gdansk, 1995.

[54] P. A. Quinn, D. J. Skyner, C. Gray, C. A. Greated, and W. J. Easson. A critical analysis of the particle image velocimetry technique as applied to water waves. In *Proc. of Euromech 279 Colloquiom*, volume 1, pages 2383–2396, Delft, 1991.

[55] M. Rahman. *Water waves*. Oxford University Press, 1995.

[56] R. J. Rapp and W. K. Melville. Laboratory measurements of deep water breaking waves. *Phil. Trans. R. Soc. Lond*, 331:735–800, 1989.

[57] J. W. Rottman, J. E. Simpson, and P. K. Stansby. The motion of a cylinder of fluid released from rest in a cross flow. *J. Fluid Mech.*, 177:307–337, 1987.

[58] P. G. Saffman. *Vortex Dynamics.* Cambridge University Press, 1992.

[59] T. Sawaragi. *Coastal engineering, waves, beaches, wave structure interactions.* Elsevier, 1995.

[60] D. J. Skyner. *The Mechanics of Extreme Water Waves.* PhD thesis, The University of Edinburgh, 1992.

[61] M. J. F. Stive. Velocity and pressure fields of spilling breakers. In *Proc. Int. Conf. Coastal Eng,* pages 547–566, 1980.

[62] C. Swan. An experimental study of waves on a strongly sheared profile. In *Proc. Int. Conf. Coastal Eng,* pages 489–502, 1990.

[63] H. Tennekes and J. L. Lumley. *A first course in turbulence.* The MIT Press, 1973.

[64] L. Thais and J. Magnaudet. A triple decomposition of the fluctuating motion below laboratory wind water waves. *J. Geophys. Research,* 100:741–755, 1995.

[65] S. M. Thompson and J. S. Turner. Mixing across an interface due to turbulence generated by an oscillating grid. *J. Fluid Mech.,* 67:349–368, 1975.

[66] E. B. Thornton. Energetics of breaking waves within the surf zone. *J.Geophys. Reseach,* 84:4931–4938, 1979.

[67] D. J. Tritton. *Physical Fluid Dynamics.* Oxford University Press, 1988.

[68] T. Vinje and P. Brevig. Breaking waves on finite water depths. Report R-111.81, The University of Trondheim and The Ship Research Institute of Norway, Trondheim, Norway, 1981.

[69] J. Westerweel. *The use of digital particle image velocimetry*, volume 4 of *Pure and Applied Mathematics*. Academic Press, New York, 1992.

[70] J. Westerweel, D. Dabiri, and M. Gharib. The effect of a discrete window offset on the accuracy of cross-correlation analysis of digital piv recordings. *Exp. Fluids*, 23:20–28, 1997.

[71] C. E. Willert and M. Gharib. Digital particle image velocimetry. *Exp. Fluids*, 10:181–193, 1991.